General Disclaimer

One or more of the Following Statements may affect this Document

- This document has been reproduced from the best copy furnished by the organizational source. It is being released in the interest of making available as much information as possible.

- This document may contain data, which exceeds the sheet parameters. It was furnished in this condition by the organizational source and is the best copy available.

- This document may contain tone-on-tone or color graphs, charts and/or pictures, which have been reproduced in black and white.

- This document is paginated as submitted by the original source.

- Portions of this document are not fully legible due to the historical nature of some of the material. However, it is the best reproduction available from the original submission.

SOLAR LIMB DARKENING IN THE FAR INFRARED AND ITS RELATION TO THE TEMPERATURE OF THE CHROMOSPHERE

by

William G. Mankin

FINAL REPORT

Period Covered: 1 Sept. 1967 - 31 Aug. 1968

Principal Investigator: John Strong

Research sponsored by
Solar Physics Division
National Aeronautics and Space
Administration

DEPARTMENT OF PHYSICS and ASTRONOMY
ASTRONOMY RESEARCH FACILITY
UNIVERSITY OF MASSACHUSETTS, AMHERST
and
THE FOUR COLLEGE OBSERVATORIES

Grant NGR-22-010-025

Contribution #46/242

SOLAR LIMB DARKENING IN THE FAR INFRARED AND ITS RELATION TO THE TEMPERATURE OF THE CHROMOSPHERE

William G. Mankin

Research sponsored by

Solar Physics Division
National Aeronautics and Space Administration
Washington, D.C. 20546

FINAL REPORT

NGR 22-010-025

Period Covered: 1 September 1967 - 31 August 1968

Principal Investigator: John Strong

Department of Physics and Astronomy
University of Massachusetts
Amherst, Mass. 01002

FOREWORD

This final report on NASA Grant NGR 22-010-025 to the University of Massachusetts covers preparations for the balloon flight of March 23, 1968, the flight itself, and the subsequent work including reduction of the data that was recorded at altitude.

The project served Dr. William Mankin as his Ph.D. Dissertation, at Johns Hopkins University. The project was planned there before the present contract began at University of Massachusetts. Dr. Mankin was a graduate student at Johns Hopkins University then, as well as during the entire period, at Amherst, when he was working on this project, until he got his Ph.D. degree in the spring of 1969.

Much of the flight equipment, and substantially all of the auxiliary test equipment, were originally provided by the ONR support that started us in balloon astronomy; and by subsequent AFOSR support.

The radiometer used in this flight was purchased from Philips Co. of Briarcliff Manor, with special adaptations to our work provided by Mr. Marc Dreyfus. Funds for its purchase were provided by ARPA Grant DA-ARO-D-31-124-G756 to Johns Hopkins University.

ABSTRACT

A balloon borne telescope and filter radiometer has been used to observe the limb darkening of the sun at six infrared wavelengths ranging from 11 to 115 μ in order to determine the variation of electron temperature with height in the lower chromosphere.

It is shown that the only important source of far infrared opacity in the lower chromosphere is the free-free transitions of negative hydrogen, for which the absorption coefficient is proportional to the square of the wavelength, and further that the source function in the far infrared is just the Planck function of the local electron temperature. Under the circumstances the infrared brightness temperature, except for a small correction for departures from the Rayleigh-Jeans law, is a function only of λ^2/μ, where λ is the wavelength and μ, the cosine of the zenith angle on the sun. Therefore, the solar infrared spectrum may be deduced from limb darkening measurements.

Furthermore, it is shown that the brightness temperature spectrum is the Laplace transform of the chromospheric electron temperature as a function of reference optical depth. It is therefore possible to determine the temperature structure of the lower chromosphere from the spectrum.

PREFACE

This work does not represent the efforts of one person alone; any project of the complexity of a balloon flight requires the efforts and cooperation of many people of diverse talents. While lack of space precludes mentioning each one individually, it is a pleasure to acknowledge with appreciation their collective contribution.

This work was performed under the direction of Professor John Strong, partially at the Laboratory of Astrophysics and Physical Meteorology of the Johns Hopkins University and partially at the University of Massachusetts. Professor Strong's always willing but never intrusive help and advice have contributed greatly to the success of this project; we readily acknowledge our debt to him.

The bulk of the day to day work fell upon the staff of the Laboratory of Astrophysics and Physical Meteorology at Johns Hopkins and of the Astronomy Research Facility at the University of Massachusetts. From the former we must mention especially the dedicated and conscientious efforts of Mr. W. T. Green in constructing and testing all the electronic equipment and of Mr. John McClellan in the mechanical design. Of the latter we mention the field crew -- Mr. William Dalton, Mr. Joe Ouilette,

Mr. Florian Duguay, and Mr. Bartley Smith -- who functioned under the trying conditions of the field trip for nearly two months. Mr. Dalton bore the double responsibility of both technical and administrative tasks at both Johns Hopkins and at the University of Massachusetts.

The cooperation of the individuals and firms who supplied various components was unstinting. The radiometer was built by Philips Laboratories under the direction of Mr. Marc Dreyfus and Mr. Jerry Pitcher. Mr. Frank Cooke did the optical work on the telescope and Mr. Wilbur Perry coated the mirrors. Dr. Hamilton Marshall of Perkin-Elmer Corp. directed the construction of the far infrared thermopile and Mr. Charles Reeder also supplied numerous detectors for tests.

We must especially express our appreciation to Mr. Leonard Kercheval of General Sensor, Inc. in Athens, Texas. When problems with the tracking sensors developed in the field, he undertook to produce on short notice some special sensors which performed admirably during flight. His personal interest and helpfulness are appreciated.

The entire staff of the NCAR balloon base in Palestine, Texas, were outstanding for their courtesy, helpfulness, and competence.

Mr. Joe Kinard of the University of Massachusetts conscientiously and accurately did most of the tedious job of digitizing the

flight data. Mr. Robert Gonter and Mr. James Hill of the Research Computing Center at the University of Massachusetts were responsible for programs for conversion of the data. Mr. Morris Birnbaum of Impro, Inc., provided valuable consultation on problems of the tracking system. Dr. Earle Mayfield of Aerospace Corporation and Dr. R.M. MacQueen of High Altitude Observatory provided data on solar activity on the date of the flight. Mrs. Faith Trueax and Mrs. Linda Barron patiently typed the manuscript.

This experiment was supported by the Solar Physics Division of the National Aeronautics and Space Administration under grant NGR 22-010-025; certain optical equipment, including the far infrared radiometer, was purchased under grant DA-ARO-D-31-124-G756 from the Advanced Research Projects Agency. During a portion of this work, the writer was supported by a National Science Foundation Graduate Fellowship. We are grateful for all this support.

The balloon borne instrument, consisting of a stabilized platform, a 38 cm Newtonian telescope, and a filter radiometer is described in detail. The two channel radiometer employs reststrahlen filters and focal isolation techniques for selecting the far infrared radiation observed. Details of the tests and calibrations as well as circumstances of the flight are given.

The corrected limb darkening curves are converted into a spectrum and the results compared with those of other investigators and with the predictions of the Bilderberg Continuum Atmosphere. In general the results are in accord with the other experimental results which may be directly compared. The results are also in accord with the predictions of the Bilderberg model for wavelengths less than 70 μ but in serious disagreement at longer wavelengths. The present results show a sharp decline in the solar brightness temperature from 80-120 μ in contrast with the Bilderberg model which predicts a slight increase in this region.

On the basis of the limb darkening measurements, an approximate model of the lower chromosphere is constructed. It is characterized by close agreement with the Bilderberg model for $\tau_5 > 1.4 \times 10^{-3}$, with a temperature plateau near 4650° in the vicinity of $\tau_5 = 2\text{-}10 \times 10^{-3}$. Above this point there is a sharp gradient to a temperature of 4000° near $\tau_5 = 6 \times 10^{-4}$, followed by a nearly isothermal region.

TABLE OF CONTENTS

		Page
Foreword		
Abstract		
Preface		
I.	Introduction	1
II.	Theory	19
III.	The Experiment	50
IV.	Results and Discussion	95
Tables		121
Figures		135
Bibliography		151

TABLE OF ILLUSTRATIONS

		Page
Figure 1.	Temperature dependence of opacity.	135
Figure 2.	Balloon borne instrument package.	136
Figure 3.	Telescope optical diagram.	137
Figure 4.	Radiometer optical diagram.	138
Figure 5.	Four crystal reststrahlen filter.	139
Figure 6.	Transmission of MgO filter.	140
Figure 7.	Channel A filter transmission.	141
Figure 8.	Channel B filter transmission.	142
Figure 9.	Amplifier schematic diagram.	143
Figure 10.	Linearity test.	144
Figure 11.	Correction for scanning function.	145
Figure 12.	Instrument temperature during flight.	146
Figure 13.	Far infrared limb darkening.	147
Figure 14.	Solar far infrared spectrum.	148
Figure 15.	Electron temperature in lower chromosphere.	149
Figure 16.	Solar far infrared brightness temperature.	150

I. INTRODUCTION

The sun has a unique role in the study of astronomy: it is the only star whose surface we may examine in detail; all other stars may be seen only as points. The immense practical importance of the sun to the earth needs no emphasis. The sun has been the most extensively studied astronomical body since the time of Galileo, when the telescope first revealed the existence of solar structure.

A vast body of information has been accumulated about the sun. This information, while it has answered many questions and dispelled many false notions about the sun, has raised new questions for which we are still striving to find answers. Some of the most intriguing of these questions are: What is the origin of the eleven year sunspot cycle? What causes the variation of solar rotation rate with latitude? What is the role of the magnetic field in solar structure? How fast does the core rotate? How has the sun lost angular momentum during its evolution? What causes solar flares? Are atomic abundances the same in various parts of the solar atmosphere? How is the corona heated to millions of degrees? How

does the sun expel matter? How can the Fraunhofer lines be explained? What is the ultimate fate of the sun?

The final answers to all these questions still lie in future solar research. Here we describe an assault on one particular question: the temperature of the lower chromosphere. Our method of attack is the measurement of the solar limb darkening (or brightening) in the far infrared and the inversion of these data to obtain the electron temperatures. This problem may have less cosmological significance than the questions mentioned above; it is, nevertheless, an important piece to be fitted into the jigsaw puzzle of solar physics, one which plays an essential role in any complete understanding of solar structure, and especially in understanding the solar spectrum.

First let us say what we mean by the chromosphere. The chromosphere is a relatively thin layer of gas, practically transparent to radiation in the visual continuum, lying above the photosphere, the visible surface of the sun. It is physically distinct from both the photosphere and the corona, the hot, tenuous outer atmosphere of the sun, in the sense that physical conditions are markedly different in the chromosphere, with a transition zone which is small compared to the depth of the chromosphere.

The limb, or edge, of the solar disk appears sharp and well defined when viewed in white light even with a powerful telescope. The intensity of the visual continuum drops by a factor of e in a distance of 100 km, corresponding to 0.15 arcsec viewed from the earth, far smaller than the resolution of the best solar telescopes. This sharp drop in continuum intensity defines the top of the photosphere. Above this point, the spectrum changes radically in two respects: first, the spectrum changes from a strong continuum crossed by many absorption lines to a line emission spectrum of neutral and singly ionized atoms superimposed upon a weak continuum; second, the emission scale height, the height over which the emission decreases by e, increases from 100 km to values several times greater for both line and continuum, and varies greatly from line to line (Thomas and Athay, 1961).

These two spectral characteristics differentiate the chromosphere from the photosphere. In the corona, on the other hand, the line emission comes from forbidden lines of very highly ionized atoms such as FeXIV or AX. The line radiation is called the E corona; superimposed on the E corona is a continuum, called the K corona, formed by scattering of photospheric light by free electrons in the corona. The chromosphere is therefore easily distinguished spectrally from the corona.

The chromosphere may be subdivied into two parts, the lower chromosphere and the upper chromosphere. The lower chromosphere presents a more or less homogeneous appearance whereas the emission in the upper chromosphere is concentrated in small regions called spicules which stick up into the corona like spikes.

The total thickness of the chromosphere is difficult to define because of the jagged nature of the spicules. An average value is about 10,000 km with the lower chromosphere comprising the first 5,000 km (Thomas and Athay 1961).

The first recorded observation of the chromosphere was by one Captain Stannyan at the eclipse of Berne in 1706; he noted a "blood red streak of light, visible for six or seven seconds upon the western limb" (Young 1897). Substantially the same report was made by Halley and Louville at the eclipse of 1715.

The chromosphere was then apparently forgotten, to be rediscovered at the eclipse of 1842. This eclipse, which was visible across southern Europe, was observed by many of the leading astronomers of the day. Observation of the chromosphere and the solar prominences excited great interest and controversy.

Secchi first photographed the chromosphere at the eclipse of 1860. The first chromospheric spectra were observed in 1868 at an eclipse in India. Several astronomers, including Janssen, Herschel, and Rayet, reported the spectrum consisted of bright lines, including prominently those of hydrogen. Almost simultaneously Janssen and Lockyer discovered that the chromosphere could be observed at the limb outside of eclipse by using a spectroscope with a high dispersion. Lockyer named the region the chromosphere ("color sphere") because of the color due to the Hα line.

One further discovery of the eclipse of 1868 deserves special note. A bright yellow line, which did not appear in the Fraunhofer spectrum, was observed. Most observers assumed that it was the sodium D line, but Janssen asserted that it did not occur at the correct wavelength. Since the line could not be found in the spectrum of any known element, he concluded that it was a line of a new element, which was christened "helium"; twenty-seven years passed before Ramsay isolated this element on earth.

Chromospheric spectroscopy continued both at eclipse and outside eclipse. Young (1897) made detailed studies at the eclipse of 1870 as well as outside eclipse. In 1892 Hale and Deslandres independently invented the spectroheliograph for photographing the entire

chromosphere outside of eclipse in the light of a single spectral line.

Photographic spectra of the chromosphere were obtained at the eclipse of 1893 and at subsequent eclipses. Because of the large gradients at the limb and the overwhelming brightness of the photosphere, it is difficult to measure height variation of emission in the chromosphere, especially the lower region, outside eclipse. The usual procedure is to let the moon "scan" the chromosphere during the eclipse as it occults the limb. This allows only a few seconds observation at each eclipse. Early flash spectra were made with slitless spectrographs, the narrow crescent of the chromosphere acting as the slit. This permits total line intensity estimates, but not the measurement of line profiles or intensity gradients. Early slitless spectra were plagued with uncertainties in the height scale and lack of photometric standardization, difficulties which made comparison of the results of different observers practically impossible.

At the 1932 eclipse Menzel introduced the "jumping film" technique in which a series of very brief exposures of slitless spectra were made at 2.4 sec intervals with rapid film transport between exposures; he obtained spectra with 800 km height resolution in the

chromosphere (Cillié and Menzel 1935). Emission scale heights were determined from these data. Other observers used slit spectrographs to obtain line profiles.

A landmark in chromospheric spectroscopy was reached at the 1952 eclipse at Khartoum in the Sudan. A program was undertaken to obtain as complete a set of data for one eclipse as possible, including accurate calibrations and a consistent height scale. The analysis of these data has made a major contribution to both an understanding of the physical conditions of the chromosphere and the theoretical methodology to describe it (Thomas and Athay 1961). Eclipse data are especially valuable for determining the vertical structure of the chromosphere.

Two techniques for observing the chromosphere outside eclipse deserve special mention: the observation of line profiles with high resolution spectrographs and, secondly, spectroheliograms, including the modifications due to Leighton to allow visualization of the magnetic field (Leighton 1959a) and the velocity fields (Leighton, Noyes, and Simon 1962). These techniques are especially valuable for determining the spatial variation of the conditions in the chromosphere.

Despite a mass of experimental data and a century of scientific

effort, the chromosphere is still incompletely understood. The uncertainty stems from both the difficulty of the observations and the complexity of the subject. A theoretical understanding of the region is complicated by the fact that the concept of local thermodynamic equilibrium (LTE) is not strictly applicable. Most of the elegant and powerful mathematical tools developed for the study of stellar interiors cannot be used in the chromosphere. The more difficult methodology for the non-LTE case is still being developed.

On the observational side, the classic observations of the chromosphere are the eclipse observations of the flash spectrum, a circumstance which allows only a few seconds observing time per year. In the visible region, the continuous opacity is so low that one sees right through the chromosphere; the total vertical optical depth of the chromosphere at 5000 Å is only 0.003.

As described above, observations of the lower chromosphere may be made in monochromatic light of absorption lines such as Hα or the K line of CaII; the interpretation of spectral line observations in terms of physical conditions in the chromosphere is, however, very difficult. The theory of line formation in a non-LTE atmosphere is complex and not completely understood.

An a priori understanding of the chromosphere is further complicated by the failure of the condition of radiative equilibrium. Radiative equilibrium may be defined as the vanishing of the divergence of the radiative flux; physically this means that there are no energy sources in the region and no non-radiative energy transport mechanisms operating. The extent and temperature of the chromosphere cannot be accounted for by radiation alone; there must be some non-radiative energy input in the chromosphere. It is important to chromospheric study to know not only how much energy is deposited by this mechanism but how this energy deposition varies with height -- without knowing the magnitude of the effect, the nature of the non-radiative input cannot be conclusively identified. Without this knowledge, we cannot claim to understand the structure and dynamics of the chromosphere.

The accurate measurement of the distribution of temperature in the chromosphere is essential for determining the energetics of the region. Considerable effort has been expended in this direction; the results are sufficiently ambiguous that the subject may not be considered closed. First of all, the chromosphere is not in local thermodynamic equilibrium, so the value of the temperature depends upon the definition employed. "Temperatures" may be defined from the total radiant energy density, the radiant energy

density at some wave length, the relative populations of different ionization stages, or the kinetic energy of the particles, to mention but a few possibilities. The density of the lower chromosphere is high enough that collisons between electrons, atoms, and ions are sufficiently frequent to maintain equipartition of translational energy. There is thus a well defined kinetic temperature, or electron temperature, at any point. This electron temperature is the temperature to which we refer throughout unless some other possibility is specifically stated.

We should note that electron temperature may differ radically from temperatures defined in other ways. Furthermore, other definitions of temperature do not give mutually consistent or even self-consistent results; the excitation temperature, for example, depends upon which atomic levels are chosen for the measurement.

The electron temperature of the chromosphere is generally considered to decline from its photospheric value near 6000° reaching a minimum of 4200-4600° in the lower chromosphere. Above this temperature minimum, the temperature rises to the neighborhood of 10,000° in the upper chromosphere and ultimately merges with the coronal temperature in excess of one million degrees. The determination of the minimum temperature, the height in the

chromosphere where this minimum occurs, and the shape of the temperature vs. height curve in this region is a subject of lively investigation by solar physicists.

The most detailed information on the variation of electron temperature through the lower chromosphere comes from the analysis of the continuum radiation. Non-LTE effects are less important for the continuum than in the interpretation of line spectra (Thomas and Athay 1961). The source of difficulty in the visible is the low continuous opacity; most of the visible continuum comes from the photosphere and is little affected by the chromosphere. Minnaert (1953) has summarized the limb darkening data in the visible. More recent work is reported by Heintze (1965). The measurement is carried higher into the chromosphere by observing the continuum above the limb at eclipses. The emission there measures the optical depth along the line of sight as much as the temperature. The temperature must be deduced from its effect on the variation of optical depth with height.

The continuous absorption coefficient increases from its value in the visible as we go into either the ultraviolet or the infrared. The ultraviolet increase is caused by the fact that the photons of shorter wavelength can ionize more and more atoms; the increase

in the infrared is caused by the λ^2 dependence of the opacity due to free-free transitions of negative hydrogen. We may therefore examine the continuous radiation arising from regions around the temperature minimum by observing in either the far ultraviolet or the far infrared. Observations in both regions are made difficult by the opacity of the earth's atmosphere.

The ultraviolet continuum has been measured from rockets (Tousey 1963). An equivalent blackbody temperature may be assigned from the observed flux. If scattering contributes significantly to the observed flux, the continuum source function is not the Planck function at the local electron temperature; this may be expected to introduce errors in determining the temperature minimum, particularly if the minimum is narrow. Furthermore, any inhomogeneities in the chromosphere will result in a measured temperature higher than the actual average temperature because the source function in the ultraviolet is so strongly dependent upon temperature. There is, therefore, a problem of interpretation in addition to the usual observational problems of rocket astronomy; the ultraviolet flux should be regarded as setting an upper limit on the minimum temperature. There is also uncertainty in the ultraviolet opacity which introduces uncertainty in the height from which the radiation arises.

Not all temperature determinations employ the continuum. The bands of carbon monoxide have been studied in both the disk spectrum and in the flash spectrum (Goldberg and Müller 1953; Newkirk 1957; Rich 1966). Relative strengths of different lines in the band yield excitation temperature; identification of this excitation temperature with the electron temperature requires careful justification where LTE may not be assumed. The amount of CO also depends upon temperature, especially on the high pressure side of the temperature minimum, so the total band strength also provides an indicator of chromospheric temperatures.

There is a vast amount of data available on line widths and shapes, especially in the Fraunhofer spectrum. Line shapes provide information on temperature because they depend upon excitation and molecular velocities, both of which are temperature sensitive, but it is difficult to deduce the electron temperature from the line shapes because of the non-LTE effects. The theory of formation of hydrogen lines is better understood than for metal lines, but the hydrogen lines do not provide a very sensitive indicator of temperature. Other, more sensitive lines lead to ambiguous results. Linsky (1968; see also Athay and Skumanich 1968) has carefully analyzed the H and K lines of CaII without the assump-

tion of LTE. He was able to fit the experimental data with either of two classes of models characterized by minimum temperatures of 4200° and 4600°. We must conclude that at the present time line observations are unable to specify unambiguously the electron temperature of the chromosphere.

Thus we turn to the infrared continuum observations. It will be shown in the next chapter that these observations, if accurate enough, yield the chromospheric electron temperature; it will also be shown that infrared limb darkening measurements and spectral measurements are equivalent. The interpretation of the infrared data in terms of the chromospheric temperature is simpler than the interpretation of any other sort of data. It avoids the difficulty caused by the failure of LTE since the infrared continuum emission depends only on the electron temperature and not at all on the radiation field, distribution of atoms among the various levels, degree of ionization, etc., as long as most of the hydrogen is in its ground state.

A number of investigators have employed the infrared spectral region. Saiedy and Goody (1959; Saiedy 1960) measured the absolute solar radiance and the limb darkening from the ground at wavelengths of 8 to 12 μ. These wavelengths are too short to

provide information on the temperature minimum because the opacity is too low. Their results do provide a valuable reference point in the photosphere-chromosphere transition region. We use their results as a boundary condition in interpreting our limb darkening data.

Intensity measurements at longer wavelengths are difficult because of the absorption in the earth's atmosphere due to water vapor and carbon dioxide. Limb darkening measurements are hindered by the absorption and by the reduced angular resolution of telescopes at longer wavelengths. Observations must be made through small "windows," spectral regions of relatively high transmission, in the atmosphere or with instruments carried aloft with balloons, aircraft, or rockets. Beer (1966) measured the spectrum to 70 μ with a Fourier spectrometer flown on a balloon; his results show a decrease in brightness temperature with wavelength, but, because his system was not absolutely calibrated, it is not possible to deduce accurate chromospheric temperatures from his data.

Noyes, Beckers, and Low (1968) measured the limb darkening at a wavelength of 22.5μ at the eclipse of 12 November 1966. They used the occultation by the moon to obtain a spatial resolu-

tion of 2 arcsec; to obtain such a resolution at that wavelength with a conventional telescope would require a telescope larger than the 100 inch telescope.

Léna (1968) used the McMath solar telescope at Kitt Peak to measure limb darkening at wavelengths of 18-24 μ. His spatial resolution was limited to 3.4 arcsec..

A group from Meudon Observatory at Paris (Gay et al. 1968) measured the spectrum from 50 to 200 μ with a balloon borne telescope of 40 cm aperture and a Michelson interferometer used as a Fourier spectrometer.

Eddy, Léna, and MacQueen (1968) also used a Fourier spectrometer with which they measured the spectrum from 80 to 400 μ. Their instruments, including a specially constructed far infrared blackbody radiance standard, were carried to 12 km altitude on the NASA Convair 990 jet aircraft.

The last two mentioned experiments obtained high resolution spectra to assess the absorption by the remaining atmosphere above their instruments.

Koutchmy and Peyturaux (1968) recently measured the absolute radiance at 20.15 μ from the ground.

As more data became available, it became apparent that earlier models of the lower chromosphere were inadequate. In April 1967, a meeting was held at the Hotel "De Bilderberg" near Arnheim, Netherlands, to construct a model consistent with the new data. As it turned out, the model was largely based on continuous measurements, especially but not exclusively the ultraviolet measurements near 1600Å; the model is therefore known as the Bilderberg Continuum Atmosphere or BCA (Gingerich and de Jager 1968). Most of the infrared results have become available since the construction of the BCA; incorporation of those data may require serious revision of the model.

It is clear that the problem of the temperature of the lower chromosphere is not closed. We shall discuss the various infrared measurements in the final chapter and compare them with the results of the present work.

We may now state the problem to which the present experiment addresses itself: measure the solar limb darkening (or brightening) in the far infrared and from this infer the variation of

electron temperature with height through as large a region of the lower chromosphere as possible.

II. THEORY

We must examine the transfer of radiation through an emitting and absorbing gas in order to understand quantitatively the relation between conditions in the solar atmosphere and the far infrared radiation emerging from the top of the atmosphere. To this end, we define the intensity of radiation at a given point in a particular direction: let dE be the element of radiant energy of any polarization within a narrow wavelength interval between λ and $\lambda+d\lambda$ which passes through an element of area da at some point P into the solid angle $d\omega$ along the normal of da during the time interval dt. We define the spectral intensity at the point P in the direction of the normal of da by

$$I_\lambda(P,\theta,\phi) = \frac{dE}{d\lambda\ da\ d\omega\ dt}, \qquad \text{(II.1)}$$

where θ,ϕ are the polar coordinates specifying the direction of the normal of da.

The spectral intensity is more properly known as spectral radiance in radiometry and spectroscopy, but the term intensity is almost universally used in astrophysics; we shall adopt this prac-

tice. The terms radiant sterance, steradiancy, and radiant flux density are also occasionally encountered.

The total or integrated intensity is the integral of the spectral intensity with respect to wavelength. The term intensity used alone may denote either spectral or total intensity.

The differential equation relating the intensity to the physical conditions in the solar atmosphere may be derived by considering the processes which change the intensity as it traverses a distance ds in the atmosphere (Chandrasekhar 1960). The processes may be characterized as:

absorption: $dI_\lambda = -\kappa'_\lambda \rho I_\lambda \, ds$, where κ'_λ is the mass absorption coefficient and ρ the density;

stimulated emission: $dI_\lambda = \kappa''_\lambda \rho I_\lambda \, ds$, where κ''_λ is the mass stimulated emission coefficient;

spontaneous emission: $dI_\lambda = j_\lambda \rho \, ds$, where j_λ is the spontaneous emission coefficient;

scattering: $dI_\lambda = \left[\frac{1}{4\pi}\int_{4\pi} \alpha(\theta,\phi,\theta',\phi')(I(\theta',\phi') - I(\theta,\phi))\, d\Omega'\right] \rho \, ds$,

where α is the product of the mass scattering coefficient and the normalized phase function.

Hereafter we neglect scattering; it will be shown later that scattering is negligible compared to the absorption and emission processes

for the wavelengths and physical conditions involved in the present experiment.

We include the stimulated emission as negative absorption, replacing the absorption coefficient κ'_λ by the "absorption coefficient including stimulated emission" $\kappa_\lambda = \kappa'_\lambda - \kappa''_\lambda$. In thermodynamic equilibrium $\kappa''_\lambda = \kappa'_\lambda \exp(-hc/\lambda kT)$, so κ_λ is positive. In certain non-equilibrium situations it is possible for κ_λ to be negative. In the lower chromosphere, κ_λ is very nearly its equilibrium value for far infrared wavelengths, as we shall show.

The net change in intensity is

$$dI_\lambda(P,\theta,\phi) = (-\kappa_\lambda I_\lambda + j_\lambda)\rho\, ds. \qquad \text{(II.2)}$$

We now assume that the solar atmosphere is spherically symmetric, that is that physical conditions depend only upon height above some reference level, not upon heliographic latitude and longitude; hence $I_\lambda(P,\theta,\phi)$ depends only upon height and zenith angle θ, as well as wavelength. This assumption is certainly true of the quiet sun on a large scale, except for the corona. It is, of course, not even approximately true of active features such as sunspots and flares. On a small scale, the assumption is not exact. The entire visible disk of the sun is mottled with small irregularly shaped bright areas bounded by darker lanes,

the so-called "rice-grain" pattern; this presumably is a manifestation of thermal convection in or below the photosphere. The bright granules range in size from 300 km to 1800 km (Schwarzschild 1959). They have lifetimes of about 9 minutes (Bahng and Schwarzschild 1961a); the r.m.s. fluctuations in brightness between bright granules and dark lanes correspond to a temperature difference of 92° (Bahng and Schwarzschild 1961b).

The ragged appearance of the solar limb in the light of the hydrogen emission lines shows that the upper chromosphere is even less spherically symmetric than the photosphere. The elements of structure, called spicules, appear as bright jets spurting into the upper chromosphere; they have characteristic diameters of 800 km and heights of 2800 km with lifetimes on the order of 15 minutes (Beckers 1964). The temperature of the spicules and of the surrounding material is uncertain inasmuch as the concept of local thermodynamic equilibrium does not apply.

The lower chromosphere, the region of interest in the present experiment, lies between these two extremes. It is more nearly related in physical conditions to the photosphere than the upper chromosphere; indeed, it is sometimes considered a part of the photosphere.

The assumption of spherical symmetry holds more accurately here than in any other region of the solar atmosphere accessible to observation (de Jager 1964). The photospheric granualtion has decreased at this height due to the fact that the decrease in density results in an increase in mean free path of radiation and hence in more effective radiative coupling of adjacent hot and cool regions. The apparently eruptive motion of the spicules, which is perhaps related to the heating of the upper chromosphere, is not present at least in the lower portions of this region. The layer is therefore comparatively homogeneous.

In the present experiment, the area of the sun observed at any instant (defined by the entrance slit of the radiometer) is greater than one square arcmin. Since granules have a size on the order of a square arcsec, the observation represents an average over thousands of granules, if indeed the effects of granules extend to the observed height. The far infrared emission is very nearly proportional to temperature -- $d\ln B/d\ln T$ varies from 1.01 to 1.15 in this experiment -- so that the average infrared emission represents the average brightness temperature of the observed area. This contrasts with the situation in the ultraviolet where the temperature dependence of the emission is very strong; near 1600Å, $d\ln B/d\ln T \approx 20$. Thus intensity measurements of a non-

uniform source in the ultraviolet, when interpreted by Planck's law, yield a temperature that is highly weighted in favor of the hotter elements.

We assume, in view of these arguments, a stratified solar atmosphere with properties dependent only upon z, the height above some arbitrary reference level. Then the spectral intensity is a function only of z and the zenith angle θ. It is convenient to use $\mu = \cos\theta$ as the angular variable rather than θ itself; μ varies from -1 to +1, but only the range 0 to +1 is accessible to observation. Because of the curvature of the layers of the atmosphere, μ varies along a ray. Unless observations are made extremely close to the limb, within a few arcsec, this variation is negligible.

We substitute $dz = \mu ds$ into equation II. 2 and obtain

$$\frac{d}{dz}\left(I_\lambda(z,\mu)\right) = -\frac{\kappa_\lambda \rho}{\mu}\left(I_\lambda(z,\mu) - j_\lambda/\kappa_\lambda\right). \qquad \text{(II. 3)}$$

The ratio j_λ/κ_λ of emission to absorption is known as the source function, S_λ. Neglecting scattering, ϵ_λ is a function only of the physical properties of the gas at height z; in principle $S_\lambda(z)$ can be calculated if the physical conditions are known. We can then formally solve the transfer equation to obtain $I_\lambda(z,\mu)$.

In actual practice, however, the conditions determining the source

function are in turn determined at least partially by the radiation; to determine a priori the radiation, one must solve the enormously more complicated problem of the simultaneous coupled equations relating radiation, mass motion, and other forms of energy transport to the physical conditions in the atmosphere. At the present state of knowledge of solar physics, a complete solution of this difficult problem is simply not possible.

Our goal is to work the other way: we deduce the source function, and thereby something of the physical conditions in the atmosphere, from the observed radiation. To this end, the far infrared observations are uniquely suited to the determination of the electron temperature of the lower chromosphere, as we shall show. This electron temperature is one of the most important parameters for understanding the physics of the lower chromosphere.

We may formally solve the radiative transfer equation by using

$$\exp\left[-\frac{1}{\mu}\int_z^\infty \kappa_\lambda(z')\,\rho(z')\,dz'\right]$$

as an integrating factor. Multiplying equation II. 3 by this factor we obtain

$$\frac{d}{dz}\left[I_\lambda(z,\mu)\,e^{-\frac{1}{\mu}\int_z^\infty \kappa_\lambda \rho\, dz'}\right] = \frac{\kappa_\lambda \epsilon}{\mu} S_\lambda(z). \qquad \text{(II.4)}$$

Integrating this equation from reference level z_0 to z we obtain

$$\left[I_\lambda(z,\mu) - I_\lambda(z_0,\mu)\,e^{-\frac{1}{\mu}\int_{z_0}^{z} \kappa_\lambda \rho\, dz'}\right] e^{-\frac{1}{\mu}\int_z^\infty \kappa_\lambda \rho\, dz'} = \frac{1}{\mu}\int_{z_0}^{z} \kappa_\lambda(z')\,\rho(z')\,S_\lambda(z')\,e^{-\frac{1}{\mu}\int_{z'}^{\infty} \kappa_\lambda \rho\, dz''}\,dz'. \qquad \text{(II.5)}$$

By choosing the arbitrary level z_0 deep enough in the sun, we may make $\int_{z_0}^{z} \kappa_\lambda \rho dz'$ very large. In that case the second term may be neglected for $\mu>0$. Physically this corresponds to choosing z_0 so deep that no radiation from that level reaches height z directly.

The observable radiation is that emerging from the top of the solar atmosphere: $I_\lambda(z\to\infty, \mu>0)$. We may obtain this from equation II. 5 writing $I_\lambda(\mu)$ for $I_\lambda(z\to\infty, \mu)$:

$$I_\lambda(\mu) = \frac{1}{\mu}\int_{z_0}^{\infty} S_\lambda(z)\,\kappa_\lambda(z)\,\rho(z)\, e^{-\frac{1}{\mu}\int_z^\infty \kappa_\lambda(z')\rho(z')\,dz'}\, dz \qquad \text{(II.6)}$$

We must investigate the sources of infrared opacity in the sun because the emergent intensity depends upon the opacity, since the radiation emitted at any point is attenuated by all the atmosphere above it before emerging. The continuous opacity of the sun mystified astrophysicists for years. It was thought that the major contribution was due to the photoionization continua of hydrogen and of metals. The Balmer discontinuity at 3646 Å is, however, much smaller than would be expected if most of the opacity came from the bound-free transitions of hydrogen; sufficient continuous opacity from metals is inconsistent with the observed strengths of Fraunhofer lines and with the absence of any absorption edges attributable to metals.

R. Wildt (1939) suggested that the opacity was due to the bound-free transitions of negative hydrogen atoms, hydrogen atoms binding an extra electron. Such ions had not at that time been observed in the laboratory, although their existence was predicted by quantum mechanics. Wildt's expectation was based on the abundant supply of neutral hydrogen atoms in the sun and a source of free electrons from the easily ionized atoms such as sodium and calcium.

The H^- ion has one bound state with binding energy .754 ev. The continuous opacity of the solar atmosphere in the visible arises from the photodetachment of the extra electron by a photon with wavelength less than 1.645 μ . Calculations of the opacity (Chandrasekhar 1945) due to this process accounted well for the solar limb darkening in the visible. In the infrared, the opacity due to bound-free transitions of H^- decreases, becoming zero for wavelengths greater than 1.645 μ . But observations show the solar opacity goes through a minimum and then increases at longer wavelengths. To account for this increase Wildt revived the suggestion of Pannekoek (1931) that the infrared opacity might be due to free-free transitions of negative hydrogen, that is, transfers of an electron from one unbounded orbit to another in the field of a neutral hydrogen atom, a process familiar to physicists as inverse

bremsstrahlung. Early calculations (Wheeler and Wildt 1942; Menzel and Pekeris 1935) of the cross section for this process indicated that it was too small by an order of magnitude to account for the infrared opacity. As late as 1946, there were suggestions (Chalonge and Kourganoff 1946) of an additional unknown source of opacity. Chandrasekhar and Breen (1946) pointed out that the Born approximation for the incident free electron wave function, which had been used in the previous calculations, was likely to be seriously in error for the very low electron energies involved. They recomputed the cross section using the Hartree approximation and found cross sections more than ten times larger than had been previously computed, fully ample to account for the solar infrared opacity. They recognized the shortcomings of their own calculation in using an *s* wave representation for the electron and in neglecting effects of exchange and polarization; yet it was a monumental computational task with nothing but a Marchant calculator.

With the advent of large digital computers, several investigators (Geltman 1956; Ohmura and Ohmura 1960; John 1964, 1965) have recomputed the free-free absorption coefficient to higher approximations. It now appears that Chandrasekhar and Breen overestimated the coefficients by abo 40%. The various recent computations are consistent to within a few percent and agree well

with experimental work in the near infrared.

For our work, we adopt the values of John (1966) which incorporate exchange and polarization corrections as likely to be the most accurate at very long wavelengths. The use of any of the other recent values would not seriously affect the results.

The absorption coefficient including stimulated emission is proportional to the number of neutral hydrogen atoms, to the electron pressure, and in the limit of long wavelength to the square of the wavelength. The wavelength squared dependence of the opacity is accurate throughout the far infrared: for temperatures encountered in the lower chromosphere, κ_λ/λ^2 varies by less than 1/2% for wavelengths greater than 10 μ. We therefore write the absorption coefficient as

$$\kappa_\lambda(n_H, p_e, T) = \kappa_1(T)\, n_H\, p_e\, \lambda^2 . \qquad \text{(II.7)}$$

The coefficient κ_1 is a function of temperature, varying approximately as $T^{-0.85}$ at solar temperatures. In Figure 1 we show the dependence of κ_1 upon temperature according to John (1966). In Table I we compare the value of κ_1 from the results of several investigators.

Although the free-free transitions of negative hydrogen are the

dominant source of chromospheric opacity in the far infrared, it is worthwhile to examine possible competing sources of opacity, such as molecular absorption or bound-free continua of neutral atoms. For comparison we shall estimate the opacity at 10μ and 100μ at the chromospheric levels where this radiation originates (in the Eddington-Barbier approximation), using the Bilderberg model of the lower chromosophere (Gingerich and de Jager 1968). This model may err in the details, but is surely accurate enough for reasonable estimates. From this model we take the following conditions:

τ_0	10^{-2}	10^{-4}	
λ for $\tau_\lambda=1$	10	100	μ
T_e	5225	4600	°K
p_e	3.94	.285	dynes/cm^2
n_H	7.85×10^{16}	7.90×10^{15}	cm^{-3}
κ_λ/n_H	2.27×10^{-24}	1.89×10^{-23}	cm^2

Atomic line absorption need not be considered in the far infrared. A line in the far infrared represents a transition between two very close levels; such levels generally occur within multiplets or, as in hydrogen, very near an ionization limit. In the first case radiative transitions are forbidden; in the latter, both the populations and the oscillator strengths are small. Hydrogen especially has small population in the upper levels because of its large ionization potential.

Molecular lines are not as easily dismissed: in planetary atmosphere, for example, pure rotation lines of polar molecules are the principal source of far infrared opacity. At solar temperatures, however, most molecules are dissociated. The principal molecules in stellar atmosphere, excepting H_2 which is not infrared active, are CO, OH, CH, and CN, which are 6 to 8 orders of magnitude less abundant than atomic hydrogen at the effective solar temperature (de Jager and Neven 1957). Metal oxides, such as TiO and ZrO which are prominent in the spectra of cool stars, are many orders of magnitude less abundant at the solar temperature. We take CO as typical in order to calculate the importance of molecular absorption.

The pure rotation spectrum consists of a number of equally spaced lines at wave numbers $\nu_J = 2B(J+1)$ where $J(=0,1,2,3\ldots)$ is the angular momentum of the lower state and B is the rotational constant, 1.93 cm^{-1} for CO (Leighton 1959b). The integrated absorption over a line is

$$\int k_\nu \, d\nu = N_J \, B_{J,J+1} \, h\nu_J \, ,$$

where N_J is the number density of molecules in the J^{th} state and $B_{J,\,J+1}$ is the Einstein coefficient:

$$B_{J,J+1} = \frac{8\pi^3}{3h^2c} \, |R_{J,J+1}|^2 \, ,$$

where $R_{J,\,J+1}$ is the matrix element of the dipole moment

between the rotational states; R will be of the same order of magnitude as the permanent dipole moment of the CO molecule, that is 10^{-19} esu-cm (Goody 1964). The mean opacity will be the integrated opacity of a line divided by the line spacing 2B. Including the stimulated emission factor $1-\exp(-hc\nu_J/kT)$, we have

$$\langle K_\nu \rangle = N_J\left(\frac{8\pi^3}{3hc}\right)|R|^2\left(1-e^{-\frac{hc\nu_J}{kT}}\right)(J+1). \qquad \text{(II.8)}$$

Since $hc\nu_J/kT << 1$, we expand the exponential retaining only the first two terms. The number of molecules in the J^{th} state is $(2J+1)\ N_{CO}/Q_R$ where N_{CO} is the total number density of CO and Q_R is the rotational partition function. In calculating the partition function, we approximate the sum by an integral since many states are populated.

$$Q_R = \sum_{J=0}^{\infty}(2J+1)e^{-\frac{c_2BJ(J+1)}{T}} \longrightarrow \int_0^\infty 2J\, e^{-\frac{c_2BJ^2}{T}}dJ = \frac{T}{c_2B}, \qquad \text{(II.9)}$$

where $c_2 = hc/k$ is the second radiation constant.

Approximately,

$$\langle K_\nu \rangle = N_{CO}\frac{c_2B}{T}(2J+1)e^{-\frac{c_2BJ(J+1)}{T}}\left(\frac{8\pi^3}{3hc}\right)|R_{J,J+1}|^2\left[\frac{2c_2B(J+1)}{T}\right](J+1).$$

For $T = 4600^\circ$, $\langle \kappa_\nu \rangle$ has a maximum at $J \approx 52$, corresponding to $\lambda = 49\mu$. At this maximum $\langle \kappa_{max} \rangle = 1.7 \times 10^{-24} N_{CO}$. Taking $N_{CO} = 10^{-6}N_H$, we have $\kappa_\lambda(CO) < 2 \times 10^{-30} N_H$. Compared to $\kappa_{50\mu}(H^-) = 4 \times 10^{-24} N_H$ for negative hydrogen, molecular absorption is entirely negligible.

Another possible source of far infrared opacity is the bound-free

continuum of atomic hydrogen. If an atom is in an excited state close enough to the continuum, a far infrared photon can photoionize it. The cross section for an atom in the n^{th} quantum state is (Aller 1963)

$$\sigma_n = \left[\frac{32\pi^2 e^6 R}{3\sqrt{3}\, h^3 c^3}\right] \frac{\lambda^3}{n^5} g = D \frac{\lambda^3}{n^5} g,$$

provided $\lambda < n^2/R$. R here is the Rydberg and g is the Gaunt factor, which is near unity. To find the absorption coefficient for radiation of wavelength λ, we sum the cross section times number density in state n over all values of $n > \sqrt{R\lambda}$ that is, over all states from which absorption may occur. Neglecting the Gaunt factor,

$$K_\lambda = D\lambda^3 \sum_{n=\sqrt{R\lambda}}^{\infty} \frac{N_n}{n^5}.$$

But

$$N_n = n^2 N_1 e^{-\frac{(E_n - E_1)}{kT}} = n^2 N_1 e^{-\frac{c_2 R}{T}} e^{\frac{c_2 R}{n^2 T}}.$$

Since the neutral hydrogen atoms are preponderantly in the ground state in the lower chromosphere, we replace N_1 by N_H, the number density of neutral hydrogens. In the far infrared, we shall be concerned with absorption from a large number of levels with approximately equal contributions; we therefore replace the sum by an integral. Setting $\beta = c_2 R/T$,

$$K_\lambda = D\lambda^3 N_H e^{-\beta} \int_{\sqrt{R\lambda}}^{\infty} n^{-3} e^{-\frac{\beta}{n^2}}\, dn ;$$

$$K_\lambda = D\lambda^3 N_H e^{-\beta} \frac{1}{2\beta} \left[e^{-\frac{\beta}{\lambda R}} - 1\right]. \qquad \text{(II.10)}$$

At solar temperatures $\beta \approx 35$. For $\lambda = 100\mu$, $\lambda R = 1097$.

Therefore we have

$$K_\lambda = D\lambda^2 N_H \frac{e^{-\beta}}{2R} = 5.3 \times 10^{-27} N_H .$$

This contribution to the opacity, which mimics the free-free opacity in its λ^2 wavelength dependence, is also negligible compared to the opacity of negative hydrogen.

One final source of opacity should be mentioned: during the collision of two unlike atoms, a time varying dipole moment is formed which can absorb radiation. In the solar atmosphere, the most prevalent collisions of this type are between hydrogen and helium. Ulrich (1968) has calculated the importance of this process for the solar infrared opacity. He finds that the induced opacity has a broad peak at 32 μ, but is largest relative to negative hydrogen absorption at 19 μ, where it contributes about 1% to the opacity. We are therefore justified in neglecting also this source of opacity.

Scattering may also be neglected. The scattering quantity which is analogous to the linear absorption coefficient for absorption is the cross section for scattering times the number density of scatterers. For Thomson scattering by free electrons, $\sigma_T = 6.7 \times 10^{-25} cm^2$.

Therefore $K_{Thomson} = \frac{P_e \sigma_T n_H}{kT n_H} = 4.6 \times 10^{-29} n_H$.

Rayleigh scattering is even less important. The scatterers are hydrogen atoms with cross section $\sigma_R = 6.7 \times 10^{-25} (.1216/\lambda)^4$.

For $\lambda = 10\mu$, $K_{Rayleigh} = 1.5 \times 10^{-31} n_H$.

Both scattering coefficients are negligible compared to absorption.

We should note that the absorption coefficients computed above are all linear absorption coefficients; they must be divided by the total density to obtain the mass absorption coefficient.

In summary, we conclude that the only significant source of continuous far infrared opacity in the lower chromosphere is due to the free-free transitions of electrons in the field of neutral hydrogen atoms, for which the opacity is proportional to hydrogen density, electron pressure, and the square of the wave length.

All that remains now is to relate the source function $S_\lambda(z)$ to the electron temperature $T_e(z)$. In the case of thermodynamic equilibrium, Kirchhoff's law states that $j_\lambda(T) = \kappa_\lambda B_\lambda(T)$ where $B_\lambda(T)$ is the Planck function, which depends only upon the temperature and not at all upon the specific nature of the emitting material. In this case, the source function is simply the Planck function of the thermodynamic temperature. Thermodynamic equilibrium does not, of course, obtain in the solar atmosphere, for in equilibrium the radiation field is isotropic and there is no net transfer of radiant energy. The equality of the source function

and the Planck function still holds if there is local thermodynamic equilibrium (LTE). This means that a local temperature may be defined at any point such that the gas conditions -- velocities, atomic excitation, etc. -- but not the radiation field, are the same as they would be in thermodynamic equilibrium. This condition is widely applied in astrophysics because of its simplicity, but is not strictly applicable in the lower chromosphere. It is still possible for a particular emission or absorption process to obey Kirchhoff's law provided the departures from LTE do not directly affect the process in question.

We wish to show that, for the free-free transitions of negative hydrogen, Kirchhoff's law holds to a high degree of accuracy with $S_\lambda(z) = B_\lambda(T_e(z))$ where T_e is the kinetic temperature of the free electrons. To establish this, we show that the free electrons have a Maxwellian velocity distribution from which we define the electron temperature, and that the conditions which are not characterized by this temperature, chiefly the thermal radiation field and the distribution of atoms among the various atomic levels and ionization states, do not significantly affect the free-free absorption and emission in the far infrared.

The question of the velocity distribution of the electron has been considered by Woolley and Stibbs (1953). A free electron is created by photoionization, usually of a H^- ion, typically with super thermal velocity, travels about, freely colliding with other electrons and with atoms and ions, gradually losing its excess energy and becoming part of a Maxwellian distribution. In contrast it also collides with photons, that is undergoes free-free transitions, which would tend to make the distribution non-Maxwellian since the radiation field is not characteristic of the electron temperature. Inelastic collisions between electrons and atoms may also introduce non-Maxwellian velocities. Eventually the free electron is captured by an atom or ion and disappears from the distribution. We shall show that the mean time from creation to destruction of a free electron is long compared to the time required for elastic collisions to thermalize it and that the inelastic collisions are negligible; it is clear that under these conditions the velocity distribution is very nearly Maxwellian.

Suppose that an electron with excess energy $\frac{3}{2}\beta kT$ is injected a thermal distribution of electrons with mean energy $\frac{3}{2}kT$. The cross section for the fast electron to collide with a slow electron and lose an amount of energy at least equal to Q_o is given by Mott and Massey (1950) as: $\sigma_o = \frac{2\pi e^4}{mv^2 Q_o}$.

If we consider only collisions in which the electron loses at least half of its excess energy, that is $Q_o = \frac{3}{4}\beta kT$, we obtain

$$\sigma_e = \frac{4\pi}{9\beta^2}\left(\frac{e^2}{kT}\right)^2 . \qquad \text{(II.11)}$$

The rate of such collisions is $n_e\sigma_e v$. The rate of collisions resulting in photoattachment is $n_H\sigma_H v$ where σ_H is the relevant cross section. The ratio of these rates, that is the mean number of "hard" electron-electron collisions suffered by an electron between production and destruction is

$$\frac{4\pi}{9\beta^2}\left(\frac{e^2}{kT}\right)^2 \frac{n_e}{\sigma_H n_H} .$$

For conditions appropriate to the levels of the chromosphere where the 100 μ radiation originates, $T = 4600^o$, $n_e/n_H = 5.7 \times 10^{-5}$. The excess energy parameter β may be estimated from the fact that the largest number of photoionizations occur near $\lambda = .5\mu$. For this wavelength, the photon energy is 2.479 ev (= kT for $T=28,800^o$). Only .754 ev is required to detach the electron; therefore the typical energy of a "new" free electron will be 1.7 ev, that is $\beta = 2.9$. The maximum value of σ_H is given by Wooley and Stibbs (1953) as 2.5×10^{-22} cm^2, so the mean number of "hard" collisions is at least 5000. Since only 3 or 4 such collisions suffice to thermalize a fast electron, we may state that, provided inelastic collisions are negligible, the electron velocity

distribution is Maxwellian.

We may neglect elastic collisions with atoms and ions. While the number density of atoms is 2×10^4 times greater than the number density of electrons, the cross section is about 10^3 times smaller. Furthermore, an electron can never lose more than .2% of its energy in an electron-atom collision due to the much larger mass of the atom.

Inelastic collisions between electrons and hydrogen or helium atoms in the ground state may be neglected because the electrons have insufficient energy to raise the atoms to their first excited state. Inelastic collisions between electrons and other atoms may be neglected unless the number of such collisions is significant, say 1%, relative to the number of electron-electron collisions. In that case

$$\sigma_a n_a \geq 1.25 \times 10^{-20} n_H .$$

The maximum excitation cross section for a permitted transition is $125\ \pi a_0^2 \lambda^2 f$ where λ is in microns (Allen 1962). Since the typical electron energy is less than 1 ev, we look for a permitted transition from the ground state with excitation energy less than 1 ev and oscillator strength $f > 10^{-5} n_H/n_a$. Since most resonance lines lie in the ultraviolet, we may expect that

$f < 0.1$; therefore we need only examine species with abundances greater than 10^{-5} relative to hydrogen: helium, carbon, nitrogen, oxygen, neon, magnesium, silicon, sulphur, and iron. A search of Miss Moore's tables (1949, 1952) shows that none of these atoms has a transition with the requisite oscillator strength. Therefore inelastic electron-atom collisions are negligible.

Another inelastic process to be considered is the collisional detachment of the extra electron from a negative hydrogen ion. The maximum cross section is $\sigma_{H^-} = 2\pi a_0^2 (R\lambda_0)^2 = 2 \times 10^{-15} cm^2$ (Allen 1963) where R is the Rydberg and $\lambda_0 = 1.645\mu$, the ionization threshold. In the lower chromosphere $n_{H^-}/n_H \approx 10^{-9}$ (Thomas and Athay 1961), so $\sigma_{H^-} n_{H^-} \approx 2 \times 10^{-24} n_H$, which is also negligible.

The only other inelastic process to be considered is the free-free transitions themselves. The probability per cm along a ray that a photon will be absorbed is $\kappa_1(T) n_H n_e kT\lambda^2$. Then the number of photons absorbed per cm^3 per second is

$$\int c N_\lambda \kappa_1(T) N_H N_e kT \lambda^2 d\lambda,$$

where $N_\lambda d\lambda$ is the number density of photons with wavelength between λ and $\lambda + d\lambda$. This will be approximately equal to the number density of photons in an isothermal

enclosure at the effective temperature of the sun times a dilution factor of 0.5. In an isothermal enclosure $N_\lambda = (\lambda/hc)(4\pi B_\lambda/c)$, so the rate of free-free transitions <u>per electron</u> is

$$2\pi \frac{kT}{hc} N_H K_1(T_e) \int \lambda^3 B_\lambda(T_{eff})\, d\lambda, \qquad \text{(II.12)}$$

where T_e is the electron temperature in the chromosphere and T_{eff} is the effective solar temperature, 5800°. The function $\lambda^3 B_\lambda$ has a maximum at $\lambda T \approx 9000$ micron-deg. We may crudely approximate $\int \lambda^3 B_\lambda d\lambda = \left(\frac{9000}{T_{eff}}\right)^3 \int B_\lambda d\lambda = \left(\frac{9000}{T_{eff}}\right)^3 \sigma T_{eff}^4$. Then the rate of free-free transitions per electron for the region where 100 μ radiation arises is approximately $2.6 \times 10^{-17} n_H$ sec^{-1}. We wish to compare this to the electron capture rate $\sigma_H n_H v$. The speed of a .5 ev electron is about 4×10^7 cm/sec; σ_H has a maximum value of 2.5×10^{-22} cm^2. The capture rate is approximately $10^{-14}\ n_H$ sec^{-1}. Therefore only one electron in four undergoes a single free-free transition on the average between creation and annihilation; the effect of the free-free transitions on the electron velocity distribution may be neglected.

We conclude on the basis of the above calculations that the electron velocity distribution in the lower chromosphere never deviates significantly from a Maxwellian velocity distribution.

Pagel (1957) has shown that, given a Maxwellian velocity distribu-

tion of the free electrons, the free-free absorption and emission occurs just as if the system were in thermodynamic equilibrium at the electron temperature. The emission by a given electron depends only upon its velocity, the impact parameter, and atomic constants. Thus the emission by an ensemble of electrons depends, apart from atomic constants, only upon the velocity distribution. If the velocity distribution in a non-equilibrium system is the same as in thermodynamic equilibrium, the spontaneous emission will be the same regardless of the non-equilibrium conditions. Similarly the absorption coefficient depends only on the velocity distribution and atomic constants. In thermodynamic equilibrium at temperature T_e, $j_\lambda = \kappa_\lambda B_\lambda(T_e)$ by Kirchhoff's law.

We have concluded that in the chromosphere, the velocity distribution of free electrons is always Maxwellian and that the only significant source of far infrared opacity is the free-free transitions. We therefore obtain the important conclusion that for the far infrared radiation from the chromosphere, the source function $S_\lambda(s)$ is the Planck function of the local electron temperature $B_\lambda(T_e)$, that is that the concept of local thermodynamic equilibrium is applicable.

We now substitute B_λ for S_λ in equation II. 6 and write

$\kappa_\lambda(z) = \kappa_0(z)\lambda^2$ where $\kappa_0(z) = \kappa_1(T_e(z))p_e n_H/\rho$. Then

$$I_\lambda(\mu) = \frac{1}{\mu}\int_{z_0}^{\infty} B_\lambda(T_e(z))\lambda^2 \kappa_0(z)\rho(z) e^{-\frac{1}{\mu}\int \kappa_0 \lambda^2 \rho\, dz'} dz. \quad \text{(II.13)}$$

We define a new independent variable τ_0, the reference optical depth, by

$$\tau_0(z) = \int_z^{\infty} \kappa_0(z')\rho(z')\, dz' \quad \text{(II.14)}$$

Note that this definition of optical depth differs from the usual definition of monochromatic optical depth at some wavelength:

$$\tau_\lambda(z) = \int_z^{\infty} \kappa_\lambda(z')\rho(z')\, dz'$$

For wavelengths in the far infrared ($\lambda > 10\mu$) the monochromatic optical depth is obtained by multiplying the reference optical depth by λ^2:

$$\tau_\lambda(z) = \tau_0(z)\lambda^2.$$

The monochromatic optical depth is a dimensionless quantity; our reference optical depth therefore has dimensions of (length)$^{-2}$.

The limits of $z = \infty$ and $z = z_0$ correspond to $\tau_0 = 0$ and $\tau_0 = \infty$ respectively. The level z_0 was chosen deep enough that $e^{-\frac{1}{\mu}\int_{z_0}^{\infty}\kappa\rho\, dz'} \approx 0$, that is $\tau_0(z_0) \to \infty$.

With these limits, equation II.13 yields

$$I_\lambda(\mu) = \frac{\lambda^2}{\mu}\int_0^{\infty} B_\lambda(T_e(\tau_0))\, e^{-\frac{\lambda^2\tau_0}{\mu}}\, d\tau_0. \quad \text{(II.15)}$$

We find it more convenient to express the intensity in terms of the brightness temperature θ, that is the temperature of a blackbody

emitting the same intensity at the given wavelength. By definition

$$I_\lambda(\mu) = B_\lambda(\Theta(\lambda,\mu)) . \qquad \text{(II.16)}$$

The Planck function in the far infrared is approximately represented by the Rayleigh-Jeans law. We write $B_\lambda(T) = \frac{c_1}{c_2}\frac{T}{\lambda^4}\left(1+\phi(\lambda T)\right)$, (II.17) where ϕ is a function only of the product λT ; ϕ may be given approximately by

$$\phi = -\frac{c_2}{2\lambda T} + \frac{1}{12}\left(\frac{c_2}{\lambda T}\right)^2 \qquad \text{(II.18)}$$

with an error of less than 10^{-4} for $\lambda T > 5\times10^4$ micron-degrees.

Equation II. 15 then becomes

$$\frac{c_1}{c_2\lambda^4}\Theta(\lambda,\mu)\left(1+\phi(\lambda\Theta)\right) = \frac{\lambda^2}{\mu}\int_0^\infty \frac{c_1}{c_2\lambda^4} T(\tau)\left(1+\phi(\lambda T)\right) e^{-\frac{\lambda^2\tau_0}{\mu}} d\tau_0 . \qquad \text{(II.19)}$$

Defining a new observing variable

$$\xi = \frac{\lambda^2}{\mu} , \qquad \text{(II.20)}$$

we obtain

$$\Theta(\lambda,\mu) = \xi\int_0^\infty T(\tau_0)\left[\frac{1+\phi(\lambda T)}{1+\phi(\lambda\Theta)}\right] e^{-\xi\tau_0} d\tau_0 . \qquad \text{(II.21)}$$

For far infrared wavelengths $\phi(\lambda T)$ is small. Furthermore, Θ is nearly equal the T in the range of τ_0 which contributes importantly to the integral, especially near the temperature minimum. Then $[(1+\phi(\lambda T))/(1+\phi(\lambda\Theta))]$ is very nearly unity. Making this approximation for the moment, we have

$$\Theta(\lambda,\mu) \approx \xi\int_0^\infty T_c(\tau_0) e^{-\xi\tau_0} d\tau_0 . \qquad \text{(II.22)}$$

To this approximation, Θ is a function only of the combination $\xi = \lambda^2/\mu$, not of λ and μ independently. Measuring the brightness temperature of the sun at $\lambda = 20\mu$ and $\mu = 0.25$ is therefore equivalent to a measurement at 40 μ at the center of the disk. Measurement of the center-to-limb variation of brightness temperature at one wavelength is equivalent to measurement of the spectrum of the center of the disk over a certain spectral range. Since it is much easier experimentally to measure accurately relative intensities at one wavelength than at different wavelengths, this is the method that we used in the present experiment: we measure relative intensities as a function of μ at six different wavelengths, and use the results, combined with an accurate value of the brightness temperature of the center of the disk at one wavelength from the careful work of Saiedy and Goody (1959), to determine the spectrum of the center of the disk over a large spectral range.

In this approximation, $\Theta(\xi)$ is just the Laplace transform of the electron temperature as a function of optical depth. If we can measure $\Theta(\xi)$ over a large range, we can calculate $T_e(\tau_0)$ over a similar range of optical depths. To take the inverse Laplace transform, we must have an analytical representation of Θ over the infinite domain of ξ; there are, however, numerical methods

(King 1964; White 1968) of obtaining the temperature over a limited optical depth from data over a limited range of ξ.

The values of $T(\tau_0)$ obtained in this manner may be used to correct the original data on $\Theta(\xi)$ for the error introduced by the approximation

$$\left[\frac{1+\Phi(\lambda T)}{1+\Phi(\lambda\Theta)}\right] = 1.$$

We write the observed brightness temperature $\Theta(\lambda,\mu)$ as a sum:

$$\Theta(\lambda,\mu) = \Theta_0(\xi) + \Delta\Theta(\lambda,\xi) \qquad \text{(II.23)}$$

where

$$\Theta_0(\xi) = \xi\int_0^\infty T(\tau_0)\, e^{-\xi\tau_0}\, d\tau_0$$

and

$$\Delta\Theta(\lambda,\xi) = \xi\int_0^\infty T(\tau_0)\left[\frac{\phi(\lambda T)-\phi(\lambda\Theta)}{1+\phi(\lambda\Theta)}\right] e^{-\xi\tau_0}\, d\tau_0. \qquad \text{(II.24)}$$

We initially use Θ_0 in place of Θ on the right hand side of II.24 to calculate $\Delta\Theta$ which is then applied as a correction of the observed brightness temperature to obtain a better value of Θ_0. This may be repeated to obtain the correct value of Θ_0 by iteration; in actual practice the correction is so small that one step suffices to correct the observations well within the errors of measurement.

Since $\Delta\Theta$ may be expected to be quite small, we may use fairly imprecise approximations in its evaluation. We expand $T(\tau_\theta)$ in a Taylor series about τ_θ^* keeping only terms up to the second derivative. Since ϕ is already a small quantity, we keep only terms up to the first derivative in its expansion about $T(\tau_\theta^*)$. Using these expansions

$$\Delta\Theta = \xi\int_0^\infty \left[T_\circ + T'\Delta\tau_\circ + \frac{T''}{2}(\Delta\tau_\circ)^2\right]\frac{\left[\phi(\lambda\tau) - \phi(\lambda\theta_\circ) + \phi' T'\Delta\tau_\circ + \frac{\partial\phi}{\partial T}\Big|_\circ \Delta\Theta\right]}{\left[1+\phi(\lambda\Theta)\right]} e^{-\xi\tau_\circ} d\tau_\circ$$

where (II.25)

$$T' = \frac{dT}{d\tau_\circ}\Big|_{\tau_\circ^*} \qquad \Delta\tau_\circ = \tau_\circ - \tau_\circ^*$$

$$T'' = \frac{d^2T}{d\tau_\circ^2}\Big|_{\tau_\circ^*} \qquad \phi' = \frac{\partial\phi}{\partial T}\Big|_{T=\tau_\circ}.$$

Transposing terms proportional to $\Delta\Theta$ and writing $\Delta\phi$ for $\phi(\lambda T_\theta) - \phi(\lambda\theta_\theta)$, we have

$$\left[1+\phi(\lambda\Theta) + \xi\frac{\partial\phi}{\partial T}\Big|_\circ \int_\circ^\infty T(\tau) e^{-\xi\tau_\circ} d\tau_\circ\right]\Delta\Theta(\lambda,\xi) =$$

$$\xi\int_0^\infty \left[T_\circ + T'\Delta\tau_\circ + \frac{T''}{2}(\Delta\tau_\circ)^2\right]\left[\Delta\phi + \phi' T'\Delta\tau_\circ\right] e^{-\xi\tau_\circ} d\tau \qquad \text{(II.26)}$$

On the left hand side we replace Θ by θ_θ without significant error and recognize that $\theta_\theta = \xi\int T e^{-\xi\tau_\theta} d\tau_\theta$. On the right hand side we collect the coefficients of various powers of $\Delta\tau_\theta$:

$$\left[1+\phi(\lambda\Theta_\circ) + \frac{\partial\phi}{\partial T}\Big|_\circ \Theta_\circ\right]\Delta\Theta =$$

$$T_\circ\Delta\phi\,\xi\int_\circ^\infty e^{-\xi\tau_\circ} d\tau_\circ + \left[T_\circ\phi' T' + \Delta\phi T'\right]\xi\int_\circ^\infty (\tau_\circ - \tau_\circ^*) e^{-\xi\tau_\circ} d\tau_\circ$$

$$+\left[T'^2\phi' + \frac{1}{2}T''\Delta\phi\right]\xi\int_\circ^\infty (\tau_\circ - \tau_\circ^*)^2 e^{-\xi\tau_\circ} d\tau_\circ. \qquad \text{(II.27)}$$

We are free to choose any value for the expansion point τ_θ^*. Letting $\tau_\theta^* = 1/\xi$, the second integral vanishes and we obtain

$$\left[1+\phi(\lambda\Theta_\circ) + \frac{\partial\phi}{\partial T}\Big|_\circ \Theta_\circ\right]\Delta\Theta =$$

$$T_\circ\Delta\phi + \frac{1}{\xi^2}T'^2\phi' + \frac{T''}{2\xi^2}\Delta\phi. \qquad \text{(II.28)}$$

To evaluate $\Delta\phi$, we expand $\phi(\lambda\Theta_0)$ about T_0 to first order:

$$\phi(\lambda\Theta_0) = \phi(\lambda T_0) + \left.\frac{\partial\phi}{\partial T}\right|_{T_0}(\Theta_0 - T_0) . \quad \text{(II.29)}$$

To the approximation used for $T(\tau_0)$, $\Theta_0 = T_0 + \frac{T''}{2\xi^2}$ (II.30)

Hence $$\Delta\phi = -\frac{\phi' T''}{2\xi^2} . \quad \text{(II.31)}$$

Substituting II.31 into II.28, we obtain

$$\Delta\Theta = \frac{\phi'}{\xi^2}\frac{\left[T'^2 - \frac{1}{2}T_0T'' - T''^2/4\xi^2\right]}{\left[1 + \phi(\lambda\Theta_0) + \Theta_0\left.\frac{\partial\phi}{\partial T}\right|_{\Theta_0}\right]} \quad \text{(II.32)}$$

With $\phi_0 = -\frac{1}{2}\frac{c_2}{\lambda T} + \frac{1}{12}\left(\frac{c_2}{\lambda T}\right)^2$, $1 + \phi + \Theta_0\left.\frac{\partial\phi}{\partial T}\right|_{\Theta_0} = 1 - \frac{1}{12}\left(\frac{c_2}{\lambda\Theta_0}\right)^2$

For the wavelengths and temperatures with which we shall be concerned, the second term amounts to less than .005 and may be neglected in computing $\Delta\Theta$. Hence

$$\Delta\Theta(\lambda,\xi) = \frac{1}{\xi^2}\left.\frac{\partial\phi}{\partial T}\right|_{T_0}\left[T'^2 - \frac{1}{2}T''\left(T_0 + \frac{T''}{2\xi^2}\right)\right] \quad \text{(II.33)}$$

This correction may be calculated after inverting Θ_0 to determine $T(\tau_0)$. It is simpler, however, and sufficiently accurate for our purposes, to evaluate the temperature derivatives in terms of the derivatives of the brightness temperature. Using the same expansion of $T(\tau_0)$ as before, we have

$$\Theta_0 = T_0 + \frac{T''}{2\xi^2} ,$$

and
$$T' = -2\xi^2\Theta_0' - \frac{\xi^3}{2}\Theta_0'' ,$$

$$T'' = \frac{\xi^4}{2}\Theta_0'' + \xi^3\Theta_0' .$$

And setting $\left.\frac{\partial \phi}{\partial \tau}\right|_{\tau_0} \approx \frac{-1}{\Theta_0}\,\phi(\lambda\Theta_0)$,

$$\Delta\Theta = -\phi(\lambda\Theta_0)\left[-\tfrac{1}{2}\xi\Theta_0' - \tfrac{1}{4}\xi^2\Theta_0'' + \frac{4\xi^2\Theta_0'^2}{\Theta_0} + \frac{2\xi^3\Theta_0'\Theta_0''}{\Theta_0} + \frac{\xi^4\Theta_0''^2}{4\Theta_0}\right] \tag{II.34}$$

Near the temperature minimum, where we shall be concerned, $\Theta_0 >> \xi\Theta'$ and $\Theta_0 >> \xi^2\Theta''$. We shall therefore expect that the last three terms will be negligible in comparison to the first two. In this case

$$\Delta\Theta(\lambda,\xi) = \frac{\phi(\lambda\Theta_0)}{4}\left[2\xi\frac{d\Theta_0}{d\xi} + \xi^2\frac{d^2\Theta_0}{d\xi^2}\right] \tag{II.35}$$

To summarize, we have shown that the brightness temperature of the sun in the far infrared may be written as $\Theta_0 + \Delta\Theta$ where Θ_0 is a function only of λ^2/μ and as a function of this quantity is the Laplace transform of the electron temperature of the chromosphere as a function of reference optical depth, and where $\Delta\Theta$ is a small correction depending upon wavelength and the derivatives of $\Theta_0(\xi)$ to account for the failure of the Rayleigh-Jeans law.

III. THE EXPERIMENT

The instrument with which the sun was observed consisted of a telescope and radiometer mounted on a balloon borne stabilized platform along with associated control and data processing equipment. The stabilized platform was developed in the early sixties in the Laboratory of Astrophysics and Physical Meteorology of the Johns Hopkins University (Strong 1967a; Bottema 1967). It was originally planned for daytime observations of the planet Venus. It has since been adapted to other observations carrying other instruments: a solar telescope (Zander 1966); a coronagraph (MacQueen 1968); and the instruments for the present experiment.

The platform with its telescope is shown in Figure 2. The platform is supported by a central stem surrounded by two concentric hollow shafts all connected together by ball bearings. The inner balloon stem runs through the entire height of the package that it supports. A command package for ground control of balloon operation containing radio beacon, ballast, altitude trans-

mitter, recording barograph, and other equipment is connected to the bottom of the stem. The suspension lines connecting the package to the parachute and, in turn, to the balloon are fastened to the top of this stem.

A reaction wheel, mounted on the second shaft, coaxial with this stem, is a cylindrical structure 114 cm in diameter and 32 cm high. It is constructed largely of aluminum honeycomb for strength, rigidity, light weight, and ease of repair. Six lead-acid aircraft batteries are mounted around the circumference of the reaction wheel to supply electrical power in flight. Although each 24 volt battery has a nominal capacity of 40 ampere-hours, it is derated by a factor of two for flight because the low temperature during the flight reduces its capacity. New, dry charged batteries are used for each balloon flight. A few days before the flight, the electrolyte is added and the batteries are charged, discharged, and recharged to test their reliability. This cycling also increases their capacity. The regular vent caps on the battery cells are replaced by modified caps which maintain an internal cell pressure of about 100 torr.

The reaction wheel without batteries has a mass of 82 kg and a moment of inertia of 16 kg-m^2. Each battery has a mass of 36

kg, giving a moment of inertia for the battery laden wheel of about 130 kg-m^2; this is comparable to the moment of the rest of the apparatus.

An amplifier and torque motor, located inside the reaction wheel, supply the motive force for the azimuth tracking system. They are manufactured by the Inland Motor Corp.

The stabilized platform, on which the telescope is mounted, is supported by the third coaxial stem directly above the reaction wheel. Because the accuracy of the azimuth tracking system depends largely upon the bearings between the reaction wheel and the platform, they are selected to have a minimum of sticking friction.

The platform is coupled to the reaction wheel through the d. c. torque motor mentioned above. The electronic amplifier of the tracking servosystem supplies a current to the torque motor which creates a torque approximately proportional to the pointing error. Sticking friction is given careful attention because it sets a limit to the tracking accuracy. the platform will not move to correct the pointing error until the torque exceeds the sticking friction.

The platform turns in azimuth by reacting against the large moment of inertia of the reaction wheel; in this respect, the large mass of the batteries is an advantage. The rotational energy thus given to the reaction wheel is transferred to the balloon through the suspension shrouds and is ultimately dissipated. The friction of the bearings between the reaction wheel and the stem provides the coupling. The suspension system, between the balloon and the gondola, contains the parachute and its shroud lines. The suspension shrouds do not provide a rigid connection so that to a degree instead of rotating the balloon, the motion imparted to the bottom of the suspension "winds it up." This wind-up, causing a restoring torque upon the reaction wheel, makes a torsional oscillator of the system, the tracking system supplying the driving input force through the torque motor and the suspension providing the elastic member. Oscillations of the reaction wheel persist throughout the time that the tracking system is operating. The oscillations are initiated by the stick-slip bearing friction. The friction also determines the amplitude of the oscillation, so the amplitude may be used as an indicator of bearing condition. If the bearings are good, the amplitude of the oscillations of the reaction wheel will be 4 to 5° peak to peak. The period is about 20 sec.

A short horizontal axle is attached to the platform stem, and the trunnion carrying the telescope and radiometer mounts on this axle. Rotation of the trunnion about the horizontal axis is controlled by a ball bearing screw connecting the trunnion to the platform. This screw achieves the elevation tracking of the telescope. It is turned by a d. c. motor controlled by the tracking system electronics.

The telescope tracking system uses two sets of sensors: "coarse eyes" for acquisition of the sun and "fine eyes" for subsequent tracking. The fine eyes have a field of view 20^{o} x 20^{o}. The coarse eyes are used initially to point the telescope so that the sun falls within this field of view. The coarse eyes sense the azimuth of the sun only; the elevation of the telescope is preset so that the sun is within the elevation field of view of the fine eyes at acquisition.

The four coarse eyes have a 360^{o} field of view. The eyes, which are silicon solar cells, are arranged in pairs, one on the side which should face the sun, the other pair on the dark side. Mechanical shields shadow the eyes so that the output is null when pointing toward the sun and increases as the pair points away from the sun. Regardless of the initial orientation of the package, the

coarse eyes will point it at the sun within 1° after a minute or so time interval after the tracking system is activated.

At a preset time, about five minutes after the coarse eyes are activated, control of the tracking system is transferred to the fine eyes. The fine eyes, manufactured by Ball Brothers Research Corp., are four silicon photovoltaic cells, each at the focus of a small lens. Half of each cell is made insensitive by an opaque coating. The cells are used in pairs, one pair for elevation, the other for azimuth. The cells in a pair are matched to have equal response, to within 0.5%. The diameters dividing the cells into sensitive and insensitive halves are vertical for the azimuth pair, horizontal for the elevation pair. The output of a cell increases from zero to saturation as the solar image formed by the lens moves from the insensitive to the sensitive half of the cell. Motion of the solar image parallel to the line dividing the cell causes practically no change in the output. When the cells of a pair are connected in opposition, their combined output goes from positive saturation to negative saturation as the sun moves perpendicular to their dividing line. The region near the null point can be made very nearly linear by proper orientation of the cells. The output is quite insensitive to motions parallel to the dividing line; elevation errors do not produce azimuth error sig

nals. For best linearity, the eyes should be adjusted so that at the null point, the output of either cell is about 15% of the saturation value. The saturation output is about 70 mv into a 51 Ω load. The slope of the output near the null point for a properly adjusted matched pair is 1.5 mv/arcmin.

The output voltage of the fine eyes is amplified by a chopper stabilized d.c. amplifier. The adjustment of the gain of the amplifier is critical to the tracking accuracy. If the gain is too low, the tracking will be poor; if, on the other hand, the gain is too high, an instability may exist: the suspension system and gondola form a compound pendulum with period about 1.6 sec; if the gain of the stabilization servo system is too high, oscillation of this compound pendulum mode is induced. It consists of a rocking motion about either the pitch or roll axis. We call either motion "nodding."

The oscillation is excited in the following manner: when the azimuth torque motor creates enough torque to break the stick-slip friction of the bearings between the platform and the reaction wheel, an impulse of torque about the vertical axis is given to the platform. But, since none of the principal axes of the inertia ellipsoid is parallel to the vertical axis, the torque excites a

component of the angular momentum about some horizontal axis. The component of rotation about the pitch axis produces an elevation error of the same magnitude. The component of rotation about the roll axis produces an azimuth error equal to the product of the rotation and the tangent of the telescope elevation angle. The servo system strives to correct this error thereby feeding more angular momentum into the system and sustaining the oscillations.

This problem could perhaps be eliminated if one of the principal axes of the inertia tensor were made precisely parallel to the vertical axis. This is a condition which is difficult to achieve; the usual procedure is to simulate the balloon suspension, and adjust the gain of the azimuth servo system until the oscillations, if started, will spontaneously die out. The gain is then decreased an extra 25% to account for the apparent increase in solar brightness at altitude because of the absence of atmospheric attenuation and to provide a margin of safety. The gain setting is made when the sun is near the meridian since the system is most unstable at highest elevations because of the dependence of the feedback upon the tangent of the elevation angle.

After amplification, the azimuth error signal goes through an RC

network which produces a damping effect. The component choices, 300 kΩ and 1μF, give nearly critical damping. The signal then goes to a bipolar solid state preamplifier and amplifier (Inland Motor Corp. Models 626 and 597 respectively). The amplifier output drives the torque motor. The torque motor produces a torque of 0.5 n-m per amp of driving current. For small errors, the torque is nominally about .35 n-m per arcmin of error. The Inland amplifier, however, has a temperature sensitive nonlinearity for small inputs; it produces almost no output until the error exceeds a certain value. Combined with bearing friction, this effect produces a dead band, a region where a tracking error produces no corrective response. Attempts to reduce the dead band below about ±6' by increasing the gain caus' the nodding oscillation to be excited. Therefore we are forced to accept a continual, almost square wave oscillation of the platform with an amplitude of 6' and a period of 20 sec. The effects of this oscillation are removed by the image tracking system described below.

These problems do not occur in the elevation system because the inertia of the system to be driven is small with respect to the inertia of the system against which reaction is exerted and because the elevation motions are very slow. The elevation system

tracks to within a minute of arc provided there is no nodding oscillation. The elevation drive saturates at a speed of 1.5 arcmin/sec. Nodding oscillations of amplitude greater than 30" are too fast for the elevation drive to follow.

In summary, the main tracking system points the axis of the telescope in the direction of the sun with an accuracy of ± 6' in azimuth and better than ± 1' in elevation provided care is taken to avoid nodding.

The telescope is a Newtonian reflector; an optical diagram is shown in Figure 3. The diameter of the primary was chosen to fit the existing equipment; the focal length was chosen as large as could be conveniently fitted into the housing of the apparatus. The primary is 41.25 cm in diameter and has a focal length of 223.5 cm; it forms a solar image 2.089 cm in diameter. To measure relative intensities at different parts of the field of view, it is important that no part of the field be vignetted. The telescope was accordingly designed to have a field of view 1° in azimuth by .6° in elevation. This field, combined with the distance the radiometer must be located from the telescope to allow room for the stem, required that the secondary mirror be unusually large; its projection in a plane perpendicular to the optic

axis is a circle 17.8 cm in diameter. With its cell and supports, the secondary obscures about one quarter of the area of the primary.

The secondary mirror is supported by two horizontal struts. The struts were placed in this manner so that the diffraction caused by them would lie principally along the long dimension of the entrance slit. The mirror cell of the secondary is fastened to the struts by ball bearings so that the mirror may rotate about an axis in its plane perpendicular to the telescope axis. An offset arm, set in the shadow of the strut, is attached to a servo motor outside the tube. The rotation of the secondary mirror is used to effect the final stage of azimuth tracking.

A third mirror, outside the tube, reflects the beam back parallel to its original direction so that the axes of the telescope and radiometer are parallel.

One of the design problems in a solar telescope is the change in focal length caused by heating of the front face of the mirror by the incident solar radiation. Even the best mirror coatings absorb 4 to 5% of the solar flux. For a balloon borne telescope, experiments indicate that this heating would cause a temperature

difference of about 10°C between the front and back surfaces (Strong, 1967b), resulting in a change in focal length of 4 mm if our primary were of Pyrex. This estimate is consistent with the measurements on Spectro-Stratoscope (Mehltretter 1967).

Such a change in focus would result in an intolerable degradation of image quality. If such a mirror were used, a servo system must focus the telescope during flight or a very good guess must be made of the change which will occur in flight, a risky procedure at best.

This problem was solved for us by the recent availability of a form of ultra low expansion fused silica, marketed as Corning #7971 ULE modified silica glass (Rahmann et al. 1968). This material has an average coefficient of expansion in the temperature range 5°C to 35°C of only 2×10^{-8}/°C, compared with 3.2×10^{-6} for Pyrex and 5×10^{-7} for ordinary fused silica. Its other thermal and mechanical properties as well as its optical working qualities are similar to ordinary fused silica.

All three telescope mirrors, the only mirrors subjected to solar heating, were fabricated of this material by Frank Cooke, Inc. The assembled telescope was tested with the Foucault knife edge

test using a 40 cm collimator (Strong 1967a). The optical quality is suitable for use as a visual telescope; at wavelengths of 10-100 μ , it is diffraction limited.

To reduce the solar heating, the telescope mirrors were coated with evaporated silver (over chromium) rather than the more conventional choice of aluminum. The coating was done by Mr. Wilbur Perry.

The assembled telescope was tested for change in focus by locating the focal point accurately before and after applying radiation simulating the solar flux, as measured by one of the coarse eyes, with a quartz iodine lamp. The change in focus was less than 0.1 mm, the limit of accuracy in the measurement set by the turbulence in the air in the tube after heating.

The entire mechanical structure supporting the mirrors and constraining the optical path from primary mirror to focal plane was made of Invar low expansion alloy. The only exception was the third mirror holder, for which Invar was not judged necessary.

The accuracy required in focusing may be calculated from the criterion of Rayleigh (1885) that the optical path difference of

rays from all parts of the mirror be less than $\lambda/2$, yielding the formula $\Delta f = 4\lambda f^2/d^2$ where Δf is the permissible error in focusing. For a wavelength of 11μ , the shortest used in this experiment Δf is 1.5 mm.

The telescope was focused using the collimator and the knife edge test to an accuracy of $\pm$ .1 mm. It is believed that the collimator was correctly focused to $\pm$ .1 mm. The accuracy of the focus was checked by observing that the sharpness of the limb of the sun at 11μ did not vary while the focus was changed $\pm$ .55 mm. We are therefore confident that the focus error did not contribute inaccuracy to the limb profile measurements.

There are two desiderata in the location of the aperture stop: first, in order that all the chief rays from the different parts of the solar disk enter the radiometer parallel, the exit pupil should be located at infinity; secondly, in order that the direction of the chief rays be independent of the rotation of the Newtonian secondary, the exit pupil should be located at the Newtonian secondary. The best compromise places the aperture stop 43 cm in front of the primary mirror. The actual position, chosen for mechanical convenience, of 90 cm in front of the primary, is almost as good and has the added advantage of using the largest possible area of the primary mirror. The stop is 37.75 cm in diameter; the un-

obstructed area, after allowing for the secondary mirror and its supports is 781.2 cm^2.

The main tracking system, as discussed earlier, is incapable of tracking to an accuracy of better than $\pm$ 6' in azimuth. An auxiliary system, which we designate the image tracking system, controls the Newtonian secondary to provide the fine tracking in azimuth. It also provides the elevation error signals to the main tracking system. This fine tracking system is capable of maintaining the solar image stationary within 2.5 arcsec r.m.s. in both azimuth and elevation, provided there is no nodding.

The center to limb scans are performed by moving a slit horizontally from the center of the image across the limb. Only a horizontal band .45 cm high, the height of the slit, across the 2.1 cm diameter image is used for the measurement; the remainder of the image is available for the tracking system.

Six sensors are arranged around the circumference of the image when it is in its stabilized position. One pair, located at the top and bottom of the image sense its position in elevation and provide an error signal indicating any deviation from its normal position. They are located at the points at which the tangent to

the limb is horizontal, and so are insensitive to small azimuth errors. The same technique cannot be used to make the azimuth sensors insensitive to elevation errors because the vertical edges of the image are used for the measurement. Two pairs of azimuth sensors are used, one member of each pair being above and the other below the horizontal position. An elevation error increases the illumination of one member of each pair and decreases the other. To the extent that the sensors are matched, the sum of the outputs of the two pairs is immune to small elevation errors.

The sensors are silicon NPN phototransistors manufactured for us by General Sensors, Inc. The sensors of a pair are matched to 2%, but there is considerable difference in the sensitivity of different pairs. The sensors act very much as current sources whose current output is proportional to the illumination for moderate illumination levels and almost independent of the voltage across them. The difference in currents from a pair is passed through a 20 kΩ resistor to provide a voltage proportional to the difference in illumination of the sensors.

The radiation forming the top and bottom of the image is directed to the sensors by small fused quartz reflecting prisms. The front

of the prisms is coated with an aluminum film of about 1/2% transmission to reduce the illumination of the sensors to avoid saturation. The sensors are hermetically sealed in glass packages 2 mm in diameter and 10 mm long. The sensitive area is approximately 1 mm square. The sensitivity of the three pairs of sensors varies from 102 μa/μw to 440 μa/μw . Saturation occurs at an illumination of about 400 $\mu w/cm^2$.

The output from the sensors controls the servo system which is a modification of the gimballed startracker built for the balloon flights to observe Venus. The operation of the portions of the startracker used in this experiment may be briefly outlined as follows: a 400 Hz inverter powers the field winding of a servo motor; the same voltage is phase shifted 90° and used to drive a solid state chopper. The d. c. signal generated by the difference in the azimuth sensor currents is chopped and amplified to provide an a. c. current which is 90° ahead or behind the field coil current depending on whether the d. c. signal was positive or negative. This a. c. current is applied to the armature of the servo motor, causing the motor to turn in a direction governed by the sign of the azimuth error signal with a speed proportional to the magnitude of that signal. The motor in turn rotates the Newtonian secondary to correct the azimuth error.

The d.c. error signal generated by the elevation image sensors is simply amplified by the startracker electronics. At a preset time, the input to the elevation tracking system is switched from the fine eyes to the amplified output of the elevation image sensors; thereafter the elevation position of the image controls the elevation tracking system.

During preflight testing under conditions simulating the balloon suspension, the azimuth tracking errors had an r.m.s. value of 2.5" and a maximum value of 7". The elevation error was not measured accurately because elevation errors are not as important to the data, but it was not much larger. During the actual flight the tracking was not nearly this good. The nodding oscillation occurred, increasing with solar elevation angle. The average elevation error was about 30" r.m.s. This error alone is not serious since the observing slit is vertical, although curved. The elevation oscillation induced an oscillation in azimuth. The azimuth null position depended upon the elevation position because of imperfect matching of the sensors. Therefore when the elevation oscillation occurred, the azimuth servo system strove to correct a non-existent error. The result was an oscillation in azimuth amounting to about 10" r.m.s. This was more of an annoyance than serious problem. The corrections introduced for this oscilla-

tion will be discussed in the final chapter.

The final stabilized image was focused on the front of a two channel radiometer built especially for this experiment by Philips Laboratories, a division of the North American Philips Co. We designate the two channels of the radiometer, which operated simultaneously, as A and B; channel A measured radiation of the shorter wavelengths, channel B, the longer wavelengths. Two slits in the front of the radiometer admitted radiation to the two channels. The slits were separated by the diameter of the solar image so that they looked at opposite limbs of the sun at the same time.

The radiometer was constructed within a box 112 x 31 x 34 cm which was suspended from a pivot near the top of the package much like a lifeboat hanging in davits. The entire radiometer was moved to scan the entrance slits across the solar image. This rather complicated procedure was intended to insure that radiation from different points on the sun was all treated exactly the same by the radiometer, i.e. that no spurious limb darkening would be introduced by the radiometer. Certain mechanical problems obviated much of this advantage; these will be discussed below.

The motion of the radiometer was controlled by two cams near opposite ends of the box. A motion with constant velocity is unsatisfactory because the pertinent variable μ varies slowly with position near the center of the disk but very rapidly near the limb. The cams are designed so far as is practicable to produce a constant rate of change of $ln\ \mu$; a constant velocity is maintained for $\mu < .25$ and $\mu > .8$. A computer generated design for the cams was produced from the equation for the velocity; the cams were manufactured on a milling machine with the coordinates calculated by the computer.

The entrance slit for channel A, operating at wavelengths from 11μ to 52μ, was .0127 cm in width and .447 cm high; it was curved to conform to the image of the limb. The angular field of view was 11.7' x 6.9'; for comparison, the angular solar radius on the day of flight was 964.1". The 11.7" slit width corresponds to the Rayleigh resolution, 1.22 λ/d, at 17μ. Choosing a slit wider than the resolving power costs information; choosing a narrower slit costs signal without a compensating increase in resolution.

The slit for channel B, which operated at wavelengths from 80 to $120\ \mu$, was the same height, but .0653 cm wide. The angular field was 60.2" in width, corresponding to the resolution at $87\ \mu$.

Considerable effort was spent on the proper thermal design of the slit region of the radiometer. The solar image, neglecting reflection losses at the three mirrors, contains 109 watts of radiant power; absorption of any considerable fraction of this power produces serious problems. The slit jaws were made of sterling silver and were polished just before flight to reflect as much power as possible. The front of the radiometer was a copper plate 3 mm thick; the silver slits were in good thermal contact with the copper plate to dissipate the absorbed heat. The copper plate was painted black; cooling fins were mounted on it and on the plate holding the image tracking sensors. A fan blew cooling air across the fins.

On the basis of laboratory tests of the effects of the fan at reduced pressures, we predicted that the temperature of the slit assembly would be approximately 20°C during the flight. It actually varied between 18°C and 20°C as measured by a thermistor mounted on the back of the slit assembly.

If the slit width were to change due to thermal effects during a scan, the resulting change in signal would be erroneously interpreted as limb darkening. Change in the radiation reaching the detector from the slit jaws themselves could introduce similar

spurious effects. The former effect was eliminated by constructing the slits from a single piece of silver rather than mounting two jaws on separate supports; the latter was reduced by gold-plating the back of the slit jaws to reduce their emissivity and restricting the area seen by the detector.

The frame of the radiometer was a 12 inch aluminum I beam and a 12 inch aluminum channel for rigidity; they were connected by several cross members. The I beam ran down the middle of the radiometer and separated the apparatus of the two channels, as shown schematically in Figure 4. Immediately behind the entrance slits, both beams are chopped by a reciprocating chopper. A radiometer for measuring the far infrared from the sun faces a severe problem in filtering out the visible and near infrared; the radiance of the sun at 5000 Å is about 2×10^6 times greater than at 50 μ . The Czerny chopper provides the first stage of the required filtering. The beam is chopped ten times per second by a small crystal, lithium fluoride for channel A and cesium bromide for channel B, which is opaque to the desired radiation but transparent in the visible and near infrared. Therefore the chopper does not chop the unwanted radiation, so that this radiation is not detected by the a.c. detection system. Actually the crystals do modulate the visible by about 10% due to reflections at the two

surfaces; this modulation is largely eliminated by masking 10% of the slit height when the crystal is not in the beam. The chopper alone discriminates against radiation shorter than 7 μ in channel A and 60 μ in channel B by a factor of about 100.

In channel A the slit is reimaged by a two mirror relay system with a magnification of two onto the filter. We chose filters using the selective reflection properties of certain crystals in the far infrared (reststrahlen bands). because of the location of their pass bands and because of their very good rejection of unwanted radiation combined with high transmission in the pass band. Reststrahlen filters have broad bands, but that is not a drawback in this experiment. The ratio of transmission at the desired wavelength to transmission in the visible increases exponentially with number of reflections; we calculated that four reflections should give sufficient selectivity.

The chief practical difficulty with a four reflection reststrahlen filter is the difficulty of aligning four different optical elements and maintaining that alignment while automatically changing filters. We have devised a filter, shown in Figure 5, which meets the requirements. The central portion of the filter is machined from a solid block of aluminum; the crystals are mounted flush

on the faces of the block and held in place by spring clips which are not shown in the figure.

The converging f/11 beam enters the block through a machined hole and strikes the first crystal at an angle of incidence of 50°. The radiation in the reststrahlen band and a small amount of the unwanted radiation is reflected. The bulk of the unwanted radiation is absorbed by the crystal or is transmitted and absorbed by a small metal baffle. The reflected reststrahlen radiation is unpolarized (for a cubic crystal), but the unwanted radiation is strongly polarized because the angle of incidence is near the Brewster angle.

The radiation reflected from the first crystal strikes the second and third crystals arranged as a roof reflector. The slit image is formed at the apex of the roof with the long dimension perpendicular to the apex line. Irregularities in the edges of the crystal affect only the radiation from the very center of the slit height.

From the geometry of this arrangement it is seen that the σ and π polarization components of the radiation are interchanged between the first and second reflection. The polarization component favored in the first reflection is discriminated against in the sec-

ond. This technique, originally due to Czerny (1923), results in better rejection of the unwanted radiation than two reflections at normal incidence.

After two reflections at the roof, the beam is reflected by a fourth crystal mounted similarly to the first and leaves the filter in the same direction that it entered it.

The entire filter unit is mounted on a filter wheel with three pairs of push-pull screws. The filter is sensitive to misalignment. Because it is located at a focus, rotational misalignment causes little error in the position of the final image; it can cause vignetting. Translation of the filter causes a translation of the final image. After the filter wheel is advanced by a stepping mechanism, a tapered pin engages a slot, locking the filter in position. This assures repeatably relocating the filter. The fluctuations in signal from scan to scan during the flight, which can be attributed to errors in relocating the filter, averaged only 1.3%.

The individual crystals may be removed and replaced on the filter block repeatably. This allows replacing the crystals with plane mirrors to align the filters.

The simplicity of the mounting, with no adjustments of the individual crystals, makes the filter easy to use and resistant to misalignment from thermal effects or mechanical shock.

It is easy to use transmission filters in conjunction with the crystal filters by simply mounting the transmission filters on the ends of the aluminum block. One of the four filters, in fact, was a narrow band interference filter centered at 11.1 μ . On this filter block, aluminized mirrors were used instead of crystals.

The crystals were 25 mm square and 3.5 mm thick, beveled on one side to fit close to the baffle in the middle of the block. The crystals were oversized for convenience in mounting and handling. Because the crystals are located near a focus, they may be quite small and do not need very good surface finish.

Figure 6 shows the measured transmission of a filter with four crystals of magnesium oxide compared to the transmission calculated from the reflectivity of magnesium oxide measured by Madden (1956). The measured transmission is relative to the transmission with four newly evaporated aluminum mirrors in place of the crystals. The measured values at short wavelengths should be regarded only as upper bounds on the transmission;

they probably represent scattered light in the monochromator.

In addition to the interferer ce filter, channel A used fil ters with four crystals of magnesium oxide, sodium fluoride, and sodium chloride. The interference filter, manufactured by Infrared Industries, had a peak transmission of 42% at 11.10 μ with a full width at half maximum of .32 μ . Extra blocking was used on the short wavelength side of the pass band to eliminate the visible and near infrared radiation. The wavelength was chosen to coincide with the wavelength used by Saiedy and Goody (1959).

Figure 7 shows the transmission for the four filters of channel A. The results for the first three filters represent actual measurements; the transmission for the sodium chloride filter is calculated from the reflectivity measurements of Mitsuishi, Yamada and Yoshinaga (1962). For the purposes of this experiment, we define the effective wavelength λ_0 for a filter by

$$\lambda_0^2 = \frac{\int_0^\infty B_\lambda T_\lambda \lambda^2 d\lambda}{\int_0^\infty B_\lambda T_\lambda d\lambda} \qquad \text{(III.1)}$$

where T_λ is the transmission of the filter at wavelength λ and B_λ is the radiance of a 5000° blackbody at that wavelength. The definition is chosen to give the proper mean value to the independent variable $\xi = \lambda^2/\mu$. Table II lists the effective

wavelengths for the filters used in this experiment.

The filtered radiation is imaged onto the detector by an ellipsoidal mirror which demagnifies the image by a factor of five; the final image fits in a rectangle 2.03 x .163 mm. The detector area was 2.5 x 1.0 mm; an oversized detector was necessitated by a slight shift in the image position during the scan -- this will be discussed in more detail below.

The detector was a special far infrared thermopile constructed by Perkin-Elmer Corp. Ordinary radiation thermopiles become inefficient in the far infrared because of reduced absorption of the black on the receiver. This particular detector was designed to be efficient at wavelengths past 100 μ at some cost of overall sensitivity. The window was diamond. The responsivity was approximately 0.5 volt/watt for radiation with $\lambda > 70\mu$. The noise equivalent power was 4×10^{-10} watts with .125 Hz bandwidth.

Channel B operates at longer wavelengths than channel A and consequently needs better rejection of short wavelength radiation and a larger spectral bandwidth to obtain sufficient signal. We obtained the requisite bandwidth by using one reststrahlen reflection;

to obtain the spectral purity we used the method of focal isolation devised by Rubens and Wood (1911). The index of refraction of crystal quartz in the visible is about 1.5; at 100 μ it is about 2.1. The focal length of a crystal quartz lens in the visible is more than twice its value at 100 μ . Rubens and Wood utilized this fact to focus the far infrared with a crystal quartz lens while permitting the visible light to diverge. We have used one of the lenses originally used by Rubens and Wood to isolate the far infrared; it has a diameter of 8 cm and a focal length of approximately 14 cm at 100 μ . For filtering we used, in addition, .2 mm of black polyethylene, which is almost totally opaque at wavelengths shorter than 3.5 μ , but which transmits about 60% at 100 μ . A cesium bromide chopper further rejects the unwanted radiation. With this filtering, the amount of signal from the sun while observing through the atmosphere from the ground (so that the far infrared is absorbed by the atmosphere) is less than the noise of the system. Laboratory tests indicate that 5-10% of the observed signal during the flight comes from spectral contamination by shorter wavelengths; virtually all of the contamination is at wavelengths of 3-4 μ where both quartz and black polyethylene have a small amount of transmission.

The mirror M7 in Figure 4 is one of two reststrahlen crystals which

reflect the desired band of wavelengths into the focal isolation apparatus. A rotating mechanism interchanges the two crystals between scans. Figure 8 shows the transmission of the filters for channel B. The crystal mirrors are made of potassium bromide and cesium bromide.

The crystal quartz lens has a large amount of spherical abberation; a fairly large detector is needed to receive all the signal. We used a Golay pneumatic detector with diamond window and 3mm diameter receiver, manufactured by Eppley Laboratories. The responsivity of the detector with 135 volt bias and 2.5 volt lamp supply is 4.75×10^3 volts/watt averaged over the spectrum of a 1000°C blackbody. It is expected to be independent of wavelength. The responsivity is almost independent of bias voltage, but varies as the 4.5 power of the lamp supply voltage. The responsivity is slightly temperature sensitive with a broad peak about 0°C; it is 12% less than the maximum at -20°C and +25°C. The noise equivalent power is 5×10^{-10} watts independent of the bias and lamp voltages, with .125 Hz bandwidth.

During the flight the temperature of the Golay cell and the lamp voltage, supplied by nickel-cadmium batteries, was recorded. Bias voltage of 135 volts was supplied by dry cells.

The detector signals are amplified by modified Type B preamplifiers manufactured by Princeton Applied Research for their HR8 amplifier. The preamps are low noise transformer input amplifiers with nuvistor first amplifier stage; we operate them from nickel-cadmium batteries in lieu of the normal amplifier power supply. The Golay cell signal is applied directly to the grid of the nuvistor rather than coupled through the transformer.

The preamp outputs go to a custom two channel synchronous rectifier amplifier. Figure 9 shows a schematic of the A channel of the amplifier. The amplification is done by two Idealab solid state operational amplifiers. The gain of the first amplifier may be changed by changing the negative feedback with a resistor network controlled by a stepping relay operating in synchronism with the filter changes. The gain for each filter is adjusted to keep the final output approximately constant.

The synchronous rectification was performed by a DPDT reed relay. A low impedance demodulator is necessary because of the low impedance of the recorder galvanometers. The chopper generates a reference signal in phase with the chopping by rotating a small blade between a neon bulb and a phototransistor. This reference signal is amplified and used to drive the demodulating

ready

The demodulated output is averaged by a RC network with time constant of 1.0 second. The d.c. current operates the recorder galvanometers. Four galvanometers with different series resistors are used to provide large dynamic range in recording.

The amplifier for channel B differs in two respects: switchable gain is unnecessary since both filters produce almost the same signal; the time constant is 3 sec because of the wider slit in channel B.

The data were recorded on two Century model 409 recording oscillographs. Each recorder has 12 mirror galvanometers; the galvanometer traces are recorded on a strip of Kodak 705 Linagraph Paper 9.2 cm wide. This is a two color line recording medium; by proper choice of filters in front of the galvanometers, a trace can be made red, blue, or black, a great convenience when several traces intersect. Eight channels are recorded on the channel A recorder: detector outputs at four different sensitivities, two tracking system error signals, a radiometer position signal, and a slit temperature signal. The other oscillograph recorded detector output from channel B at four sensitivities,

angular position of the Newtonian secondary mirror, Golay cell temperature, radiometer position, and the output of an extra tracking sensor aimed at the sun. This last item was to compare the apparent brightness of the sun at altitude with the same quantity measured from the ground.

A cam which closes a microswitch at 16 selected points in the scanning cycle was attached directly to the cam which moves the radiometer. This determines the position on the sun to which the data refers at that point. In addition a signal is superposed on this trace to indicate which filter is in place.

Once each revolution of the cams another switch is actuated which causes the filter in one channel to change. The filter changes occur when the slit of that channel is aimed 32' from the center of the sun, that is 16' past the limb, so that no data are lost during the 10 sec required for the change.

An entire scanning cycle requires four minutes. Starting with a filter change, the cycle is as follows: the slit rapidly approaches the image of the limb; as it gets near the limb, it slows down, crossing the limb very slowly one minute after the cycle starts; as the slit approaches the center of the image, where μ varies

more slowly with position; it scans faster, reaching the center of the image two minutes after the start of the cycle. At this point the slit for the other channel is 16' past the limb and the filter in that channel changes. During the next two minutes the process is reversed. Each cycle produces two center-to-limb curves from each channel, one as the slit moves from limb to center, the other as the slit moves from center to limb. Half the time is spent with the slit beyond the limb of the solar image.

There are a large number of tests and calibrations which must be made before one is ready to commit such an instrument to flight. Any tests which are to be made must be made before flight as there is no assurance that the equipment will survive the flight at all, much less remain unchanged in calibrations. It may be noted, however, that in eight flights of this basic package, with six different experiments, not a single optical component has been broken.

Tests and adjustments such as aligning the tracking sensors with the axis of the telescope and setting the brightness of the recorder lamps to properly expose the film are so obvious as to require no further mention. Several important tests do deserve closer examination. These are all designed to insure that the final deflection of the trace on the film is indeed proportional to the radiance of

the source and independent of the other variables.

The first requirement is that the detection, amplification, and recording system be linear. At the signal levels of this experiment, there is no problem with non-linearity in the detectors themselves; tests show they would respond linearly to orders of magnitude more signal. The outputs of the various amplification stages are all far below their saturation values and the large negative feedback combined with the large open loop gain of the operational amplifiers guards against nonlinearity. The switchable gain of the channel A amplifier is further insurance.

The most suspect element is the galvanometers. The linearity of all the galvanometers which record the center to limb data was tested by putting precisely measured currents through the galvanometers and measuring the deflection of the trace in the film plane. Non-linearities, although they exist, are so small that they introduce negligible error.

The final linearity test checks the entire system. The telescope is illuminated with collimated radiation from a blackbody; the galvanometer deflection is measured for different temperature settings and plotted against source radiance. A typical result is shown in

Figure 10. Clearly deviations from linearity are not important.

The next factor to be checked is the independence of the sensitivity of the radiometer to position during the scan. This presented a serious problem involving the basic mechanical design of the radiometer. The test was made by fastening an infrared source to the front of the radiometer and recording the signal as both source and radiometer moved through a scan. It was observed that the signal varied with the position of the radiometer in its scan; the variations were correlated with the steepness of the driving cam. We concluded that there was a mechanical distortion of the radiometer frame due to the forces, approximately 100 newtons, exerted by the driving cams, causing motion of the final image on the detector. Some optical components were mounted on the I beam; others, on the cross members. A motion of 5- 10 μ of the image on the detector could account for the observed variations.

The use of an oversized detector reduced the variation to a barely tolerable value. The result was a sensitivity which rose smoothly from .995 times the mean sensitivity at the limb to 1.000 at the center. On the steeply descending part of the cam the sensitivity increased to 1.010, decreased to 1.000 about 5' from the center, and fell smoothly to .995 at the limb.

To measure to fractional percent accuracy with laboratory sources is difficult; some uncertainties remain in the values given. The results are consistent with measurements with all four filters in channel A, although the signal to noise ratio with the NaCl filter wasn't sufficient to be certain whether the distortion affected that filter. We estimate the remaining uncertainties due to this cause to be 1/2%.

This difficulty should not appear in channel B, although we cannot state from the data that it is absent. The optical components for channel B are mounted in a brass tube which serves as an optical bench; this tube in turn is mounted only on the I beam. Furthermore, the detector is so large and the image so fuzzy that small motions of the image on the detector would not be noticeable.

The effect of the tracking deadband is to cause the radiation to strike a slightly different part of the telescope mirrors and to enter the radiometer at a slightly different angle. The effect of these changes on the signal was measured by measuring the signal at a fixed position on the sun while moving the telescope around within the deadband. No change was observed in the signal at 11 μ and 18 μ . Furthermore, there is no evidence in the flight records for correlation between the signal and swings across the deadband.

We conclude that errors due to this source are negligible.

The most important and difficult calibration is the determination of the scanning function, that is, the response of the system to a point source. This is related to the optical transfer function of the telescope and the geometry of the slit. The response of the system to a point source is not a delta function because of the geometrical width of the slit, the aberrations of the telescope, diffraction, scattering, and the time constant of the amplifier. The first two are independent of wavelength. Diffraction depends in a simple manner upon wavelength; both the intensity and the angular distribution of the scattered radiation may depend upon wavelength in a complicated manner. The effect of the time constant is negligible in our case.

The scanning function was measured for the three shortest wavelength filters by illuminating the telescope with collimated radiation from a narrow slit in front of the 1000°C blackbody. The radiometer was scanned across the image of the source and the response measured. The source is not a point, but the effects of its known width can be simply removed from the results. It is necessary that the source have the same curvature as the entrance slit and that the telescope and collimator be carefully

aligned.

It was not possible to measure experimentally the scanning function for the three longest wavelength filters because six meters of humid air is opaque at wavelengths in their pass bands. It is necessary either to extrapolate the measurements to longer wavelengths or to calculate the scanning function.

It is possible in principle to calculate the scanning function except for scattering at the mirrors. The diffraction calculation for the aperture pattern of the telescope is tedious but not difficult; it is tractable with a large computer. The results of such a calculation at wavelengths where measurements can be made do not, however, agree with the measurements. This is the biggest difficulty in the present experiment, producing the largest uncertainties in the results.

We have been forced therefore to extrapolate the measurements at shorter wavelengths to the longer wavelengths. We have assumed that the wavelength dependence of the scanning function $S_\lambda(x-x')$, that is the response of the radiometer at position x to radiation of wavelength λ from a point source whose geometrical image is at x', may be included by writing

$$S_\lambda(x-x') = S\left(\frac{x-x'}{\lambda}\right) \quad ; \qquad \text{(III.2)}$$

in other words, we assume that the size of the image of a point object is proportional to wavelength. This assumption depends upon the fact that we expect diffraction to be the dominant effect rather than geometrical aberrations or finite slit width. Therefore, to obtain the scanning function at long wavelengths, we have simply scaled the coordinate of the short wavelength measurements by the ratio of the wavelengths.

For this purpose we have used the measurements with the 18 μ filter. We chose to use the measurements at this wavelength because they had the highest signal tc noise, their spectral bandwidth more nearly simulated that of the longer wavelength filters, and the ratio of wavelength to slit width most closely simulates that of the channel B filters.

The extrapolated scanning function was used in analyzing the data from the NaCl, KBr, and CsBr filters. The uncertainty in the scanning function represents the largest uncertainty in this experiment. There is one piece of evidence which gives confidence in this procedure: the extrapolated scanning function predicts fairly accurately the observed signal when the slit is beyond the limb of the sun.

The package was launched from the National Center for Atmospheric Research Scientific Ballooning Station at Palestine, Texas (31°47'N., 95°42' W.), at 1223 UT on 23 March 1968. The weather was clear with winds from the north at four knots. Payload weight at launch was 1075 kg. The balloon, manufactured by Winzen Research, Inc., was a 2.96 million cubic foot (83,000 m^3) balloon of 1.5 mil polyethylene with 650 lb test load tapes on the seams. It was inflated with 2161 m^3 of helium at STP giving a gross lift of 1967 kg and a free lift of 146 kg above the gross load of 1821 kg. The package ascended at a nearly uniform rate of 4.0 m/sec reaching ceiling of 27.2 km about 1415 UT. The first automatic operation, coarse tracking, commenced at 1426. The system was fully operational with the transfer of the elevation control from the fine eyes to the image sensors at 1517. Data were taken continuously until 2018 at which time the radio command was given to terminate the flight. The package descended by parachute landing in a field near McComb, Mississippi, about 2100 UT. Minor damage was sustained due to dragging of the package by the parachute.

In addition to the data on the center to limb variation of the solar infrared radiation, which will be discussed in the final chapter, it is worthwhile to record a few engineering data obtained. There were three recording thermometers aboard; their records are

shown in Figure 12. One was located on the floor directly under the telescope, near the center of the package; the second was also on the floor, but near the outside wall; the third was inside the electronics tank. The temperature in the tank was somewhat buffered by the addition of twelve half liter water bottles, six of which were frozen. The tank was thermally insulated. The effects of passing through the tropopause, a temperature of -62°C at 18.6 km altitude, may be seen on both ascent and descent. Temperature at altitude, with the sun shining on the package, was not greatly different from ground temperatures.

The output of the sun brightness monitor, a silicon cell identical with the coarse eyes, was 25 % greater at altitude than on a clear day in Palestine a few days before launch. The difference is attributed to the lack of atmospheric absorption and scattering at altitude.

Finally, it seems appropriate to close this chapter on instrumentation with some remarks on how we would improve the experiment with the benefit of hindsight. It is inherent in the nature of balloon experiments that one has little opportunity to correct his mistakes; perhaps future experiments can profit from these observations.

it should be possible to make any effects of tracking errors negligible. The image tracking system is intrinsically accurate. The difficulty lay in the frequency response of the servo systems: in particular, the elevation drive is too slow to follow the nodding of the package. We attempted to eliminate the nodding; Nidey (1968) says it is better to assume that the nodding is inevitable and design the servo system to counteract it. He advocates replacing the worm drive with a torque motor. The telescope would then not be aware of the nodding except through bearing friction; the torque motor would be fast enough to eliminate errors from this source. Such a system, combined with the present image tracking system in cross elevation, should provide tracking accuracy to better than 5" despite gondola motions of several minutes.

The radiometer should be fastened rigidly to the telescope rather than moving to effect the scan; this would eliminate the problem of mechanical distortion of the radiometer during a scan. The scan could be produced by moving the image sensors and allowing the tracking system to move the image to follow sensors. The input to the main azimuth servo system could be the deviation of the Newtonian secondary from its neutral position as measured by a pot attached to the servo motor; this would avoid the difference in direction of the chief rays entering the slit from different parts of

the sun, the problem which caused us to abandon this approach in the first place. Under the proposed scheme the axis of the telescope would move to point at the area being observed. Any off axis aberrations of the optical system would also be avoided thereby.

Realizing after the fact the importance of an accurate knowledge of the scanning function, we would attempt to take the instrument to a vacuum test chamber where the scanning function could be measured for all the wavelengths. The uncertainties in the scanning function are the limiting factor in the accuracy of the results.

If the absolute intensity is known at one wavelength, it is possible to deduce the spectrum by measuring only relative intensities. The errors are cumulative, however, because everything is tied to one point; the farther one goes from the reference wavelength, the larger the errors become. This fact limits the usefulness of the technique, an objection which could be overcome by measuring absolute intensities. To measure absolute intensities with the accuracy of 1-2% which is required for the results to be useful is a formidable task, but it would make a significant improvement in the experiment. An assessment of the amount of water vapor between the telescope and the sun would have to be made.

On the purely instrumental side, we believe that the four crystal reststrahlen filter combined with a transmission filter of 2mm of crystal quartz and .2 mm of black polyethylene would provide satisfactory filtering for the long wave filters and would be easier to employ than the focal isolation apparatus. The difficulty of aligning an optical system with radiation one cannot see and can barely detect electronically is considerable.

IV. RESULTS AND DISCUSSION

The data were obtained in the form of analog traces on a paper strip 9.2 cm wide and 45 m long. The first, and most laborious, task was to convert the deflections into numerical values. This was done manually for several scans to obtain a "quick look" at the data. Because of the large volume of data -- some 20,000 data points were measured -- we decided to make the conversion process as nearly automatic as possible; a Perkin-Elmer DDR2 digital recorder was available for this purpose. A mechanical device was constructed which allowed the operator to set a pair of crosshairs on the point to be measured; a linear encoder followed the motion of the crosshairs. When the operator closed a foot switch, the recorder punched the position of the crosshairs onto paper tape. The resolution of the encoder is .12 mm, about .15% of the maximum deflection. The conversion of the punched paper tape to useful form proceded in a rather round-about way. The paper tape was converted to magnetic tape by National Cash Register Co.; the magnetic tape was interpreted and edited by the University of Massachusetts computer which eventually punched the results onto cards. The cards were then used as input to the data analysis programs.

The analysis of the data from channels A and B differed somewhat because of the markedly different signal to noise ratio. The ratio of signal to r.m.s. noise was greater than fifty for all filters in channel A; each scan gave a well defined center-to-limb curve. The signal to noise ratio for the data from channel B, on the other hand, is only about 6, so that the limb curve for one scan is very ill defined. It was necessary to average all the scans from a single filter of channel B before determining the signal as a function of distance from the limb.

The record from each scanning cycle of channel A was marked at 125 particular points; 32 of these points were marked by signals from the drive mechanism at fixed intervals during the scan; the remaining points were interpolated between these reference marks.

The use of the signals from the drive mechanism to determine the position of the radiometer in its scan was essential because of variability in the speed of the paper drive in the recorders.

At each of the 125 marked points, the position of the radiometer was known to within $\pm$.002 cm from preflight calibration of the position signals. At each of these 125 points the deflection was recorded. When the slit was near the edge of the image, the signal

oscillated with peak-to-peak amplitude on the order of 50% of the signal. This oscillation was due to the motion of the image in azimuth because of stabilization errors. Where these fluctuations occurred, separate points were measured at the maximum and minimum; the average of these two was taken as the correct value at that point.

These fluctuations near the limb affected only the determination of the position of the limb. The data on relative intensity were used only from distances from the limb which were great enough that the tracking errors did not produce noticeable effect.

The limb was defined as that point where the signal dropped to 50% of its value at the center of the sun. To obtain the central deflection a zero value, measured when the slit was more than 5' beyond the limb, was subtracted from all the data points. The central value was taken to be the average of the six data points nearest the center of the sun; for all these points $\mu > 0.9$. For each scan, the point where the signal was first less than 50% was determined. Then the best straight line (in the least squares sense) of signal vs. radiometer position was fitted to this point and the two points on either side of it; the radiometer position where this line crossed the 50% level was defined to be the limb.

The error introduced by neglecting limb darkening in determining the limb in this manner is only about 12 μ at most; since this amounts to only a tenth of the width of the slit, it may be neglected.

Once the position of the limb has been determined, the distance from the limb is calculated for each of the points. To average different scans, it is necessary to know the signal at the same position on the sun for each scan. From the raw data, a three point Lagrange interpolation was used to determine the signal at 100 selected distances from the limb, 50 for each half of the scanning cycle. The data from all the usable scans were averaged to produce the uncorrected limb curve for each filter.

The data from each of the 20 scans of each filter were punched onto the paper tape. Because of operator error or equipment malfunction, some of the scans had to be discarded. Ten to fourteen usable double scans (limb to center to limb) were obtained for each filter. Since noise did not contribute appreciably to the errors in these limb curves, the data which were rejected were not repunched.

The averaged scans were corrected for the error introduced by

the mechanical distortion of the radiometer discussed in the preceding chapter; the correction varied from +0.5% to -1.0%. The center-to-limb scans were then averaged with the limb-to-center scans. In this average, the distortion correction is less than 0.5%, so an estimate of $\pm$ 0.5% for the remaining uncertainty due to the radiometer distortion is conservative.

The average curve is then corrected for the effects of the scanning function. The measured response to a point source when integrated once yields the output which would be expected if the sun were uniformly bright. The difference between this value and the observed value is due to limb darkening. Thus to the observed value, we add a correction equal to $1 - S(x)$, where $S(x)$ is the integral of the scanning function at distance x from the limb, to obtain the limb darkening curve we would expect if there were no diffraction. The correction is shown in Figure 11.

Points for which the correction applied in this manner exceeds .150 are discarded. This determines how close to the limb we accept data and consequently the minimum value of μ that we observe. This minimum value of μ for each filter, with the corresponding equivalent wavelength defined by λ_0^2/μ, is shown in Table III.

Due to the uncertainties in the correction for the scanning function, we assign to each point an estimated uncertainty which is equal to .005 plus one third of the correction for the scanning function plus the probable error due to noise. The systematic errors are larger than the random errors; we cannot call this estimated uncertainty a probable error. It merely represents our best judgment of the likely errors.

There is one remaining correction to be made to the curve for the NaCl filter, due to spectral contamination of the desired radiation with a small amount of visible and near infrared. Observation of the sun with the NaCl filter from the ground gave a signal which was 5.2% of the signal from the center of the sun during the flight. Since the atmosphere is totally opaque at wavelengths in the pass-band of the NaCl filter, this signal must represent "leakage" of visible through the filter. This leakage is expected to have the same spectrum as the sun. Therefore we have corrected the limb darkening curve for the NaCl filter for this spectral contamination by subtracting a curve which has magnitude .052 at the center of the disk and has the same limb darkening parameters as those given by Allen (1963) for the total solar radiation, namely

$$I(\mu)/I(1) = 1 - .84(1-\mu) + .20(1-\mu^2). \qquad \text{(IV.1)}$$

The remainder, radiation in the NaCl reststrahlen band, is re-normalized to give the center-to-limb curve for the effective wavelength of 52 μ.

There is no evidence for significant "leakage" by the other three filters of channel A. From the nature of the reststrahlen filters, we expect that the leakage would be almost independent of the wavelength of the filter; roughly speaking, visible light can't tell the difference between NaCl and NaF. Therefore the fraction of the signal coming from leakage is inversely proportional to the signal. All the other filters have at least 10 times the signal from the NaCl filter, so we expect none should have more than .5% contamination, which would only change the limb darkening by .2%, an error negligible in comparison with the other errors in experiment.

The limb darkening curves for the channel B filters are constructed in a similar manner with one exception. Because of the low signal to noise, all the scans from a filter are averaged before determining the location of the limb. The fluctuations due to tracking errors and the small amount of long term drift of the tracking system are not as important as in channel A because the spatial resolution is poorer at the long wavelengths of channel B.

The records were sampled at 91 points per scan rather than 125 as in channel A because of the decreased resolution and the longer time constant of the channel B amplifier.

A total of 41 scans for each filter were averaged. No corrections were made for distortion or spectral contamination. There is no evidence for any distortion, but laboratory tests indicate the possibility that 5 to 10% of the signal might be due to the short wavelengths. This short wavelength radiation could only come from wavelengths near 4μ. The sun at 4μ has virtually the same limb darkening curve as we observe at the longest wavelengths, so the correction makes essentially no change in the results.

The corrected limb darkening curves for the various filters are shown in figure 13. The individual points shown are the average of 20 to 30 measurements for the channel A filters and 41 measurements for the channel B filters. The solid curves shown are based on a smooth curve fitted to the whole spectrum.

We have a high degree of confidence in the accuracy of the limb darkening curves from channel A. There is more room for uncertainty regarding the curves from channel B because of the lower signal-to-noise ratio, because of the impossibility of making

many of the tests to check the constancy of the sensitivity of the apparatus during a scan, and, most importantly, becaus of the uncertainty of extrapolating to channel B the scanning function measurements on channel A. We believe the results to be essentially correct, but cannot absolutely exclude the possibility that the absolute value of the limb darkening is significantly in error. The conclusion is clear, however, that there is considerably more limb darkening at 85 μ than at 115 μ. There seems to be no way that this conclusion could be erroneous, and this fact strongly supports our conclusion that the Bilderberg model incorrectly predicts the infrared spectrum in this spectral region.

Once the corrected center-to-limb intensity curves have been constructed for all six filters, the brightness temperature at the center of the disk must be assigned. For the 11 μ filter, we adopt the value of 5036 ± 30°K given by Saiedy and Goody (1959). The value for each of the successive filters is determined from the limb darkening curve for the preceding filter as follows: the relative intensity is converted to absolute intensity by multiplying by the intensity of a blackbody at the temperature of the central brightness temperature. Intensities are converted to brightness temperatures using the Planck function. A weight which is inversely proportional to the estimated uncertainty is

assigned to each point. A least squares fit of a polynomial in μ is made to all the points, using the assigned weights. Three terms are used in describing the channel A data; only two terms are used for the less accurate data of channel B. From this polynomial approximation the brightness temperature is determined at $\mu = [\lambda_i/\lambda_{i+1}]^2$ where λ_i is the effective wavelength of the filter in question and λ_{i+1} is the effective wavelength of the succeeding filter. This value of the brightness temperature is assigned to the center of the sun at the next wavelength.

After the central brightness temperature for each filter has been determined, we compute the brightness temperature of each data point along with the corresponding value of $\xi = \lambda^2/\mu$. The resulting data $\Theta(\xi)$ represents our basic experimental result.

In calculating ξ, as in all the analysis of the experimental data, the wavelength of the radiation was assumed to be the effective wavelength transmitted by the filter, that is, no correction was made for the rather large spectral bandwidth of the filters. Because of the fairly slow change of solar brightness temperature with wavelength, no very serious error was introduced by

this procedure.

Figure 14 shows the spectrum calculated from the limb darkening measurements of the present work (solid curve) and a representative number of data points with their estimated uncertainties, along with the results of a number of investigators. The predictions of the Bilderberg model are also shown (dashed curve).

There have been several ground based studies of the region from 10 to 25 μ (Saiedy and Goody 1959; Saiedy 1960; Léna 1968, 1969; Kondrat'ev et al. 1965; Koutchmy and Peyturaux 1968). The results are not all consistent, but the discrepancies are not much greater than the estimated errors. The mean of the observations is probably accurate to ± 100°; it agrees well with the BCA.

The spectra in Figure 14 which are deduced from limb darkening (Saiedy 1960; Léna 1968, 1969; and the present work) have all been computed in the same manner and are all tied to the point 5036° at 11.1 μ . The value given by Kondrat'ev et al. at this wavelength, 5200°, is significantly higher. Saiedy and Goody have used great effort to make an accurate radiometric measurement, while the result given by Kondrat'ev et al. is a byproduct of an atmospheric transmission measurement. We believe that

the value 5036 is more reliable.

The present work and the measurements by Léna both agree with the limb darkening measurements of Saiedy; those results only extend to $\mu = 0.4$. At smaller μ, our measurements and Lena's disagree in that his show a dip near $\mu = 0.3$ which is not apparent in the balloon data. His results should be more reliable since he used a larger telescope, the 150 cm McMath solar telescope at Kitt Peak, and longer observing time and had no tracking problems. The advantage of a balloon telescope, freedom from atmospheric absorption, is not important at 11 μ We conclude that it is probable that at wavelengths greater than 20 μ, our results are too high by about 100°. The absolute intensity measurement by Koutchmy and Peyturaux at 20.5 μ yields an even lower temperature.

The Bilderberg model, then, appears to be quite accurate to wavelengths of 30 μ. Beyond this point, there is greater ambiguity. The eclipse limb darkening measurements of Noyes, Beckers, and Low (1968) imply that the slope of the spectrum $d\Theta/d\lambda$ near $\lambda = 60\mu$ is nearly zero, although slightly negative, which is entirely consistent with our results. Beer (1966) gives only a power law for the intensity from 10 μ to 70 μ

$I_\lambda \propto \lambda^{-4.075}$ based on his balloon flight data. Taken literally, this would imply a slope in the spectrum $d\theta/d\lambda \approx 10°/\mu$ near 50 μ.

A group from Meudon Observatory (Gay et al. 1968) also measured the absolute brightness from a balloon at wavelengths of 50 to 200 μ. Their results at all wavelengths are higher than our results, but if reduced by a constant factor, their shape is consistent with our spectrum, and also agrees with results mentioned above near the short wavelength end of their spectral region and with the results of Eddy, Léna, and MacQueen (1968) at the long wavelengths.

The only other results available in the 100-200 μ region are the results described in this paper and the absolute intensity measurements of Eddy, Léna, and MacQueen made from the NASA Convair 990 aircraft. Their results imply a temperature minimum higher in the atmosphere than the Bilderberg model, with a lower value of the temperature. Our results at the longest wavelengths are lower still, but are consistent within the estimated errors of the two experiments.

Recent rocket measurements of the ultraviolet continuum by

Parkinson and Reaves (Gingerich 1969) have resulted in an ultraviolet brightness temperature minimum of about 4300° in contradiction to the earlier rocket work. Since the BCA relied heavily on the UV measurements in determining the temperature minimum, the work of Parkinson and Reaves casts serious doubt on the validity of the BCA.

Gingerich (1969) has constructed a new model incorporating the work of Parkinson and Reaves and the infrared measurements of Eddy, Léna, and MacQueen. This model is characterized by a minimum at a lower temperature, 4250°, than the BCA, but which occurs higher in the chromosphere.

The predictions of the Gingerich model differ from those of the BCA primarily in the region covered by our channel B filters. Our results favor the Gingerich model over the Bilderberg. It should be noted that Gingerich himself was one of the principal authors of the BCA.

It is interesting to note the rapidity with which ideas about the solar temperature minimum have evolved in the past few years. At the time the present experiment was first proposed (1966), it was thought that the minimum in the solar infrared brightness

temperature would occur near 15 μ (de Jager 1964; Noyes 1966). At the time of the balloon flight (March 1968), the Bilderberg model was believed to be correct, implying that the minimum occurred near 100 μ . At the present writing (April 1969), there is some evidence that it may occur as far out as 300 μ.

We now proceed to construct an empirical model of the lower chromosphere based almost entirely on the limb darkening measurements reported here. We do not represent this as the best model which can be constructed with all the available data and the best current theoretical understanding of this region; the construction of such a model is beyond the scope of this paper. The model we construct merely best reproduces the measured infrared limb darkening.

We make the assumptions discussed in Chapter II, namely: the electron temperature is a function only of height in the chromosphere; the far infrared source function is the Planck function of the local electron temperature; the only source of opacity is free-free transitions of negative hydrogen, with opacity proportional to λ^2. Then it follows that the brightness temperature $\Theta_0(\xi)$ corrected for the departures from the Rayleigh-Jeans law is just the Laplace transform of the electron temperature as

a function of reference optical depth.

To determine the chromospheric temperatures from the observations of the brightness temperature we must fit the brightness temperature with a function whose inverse Laplace transform we may obtain analytically or numerically (White 1968) or, alternatively, to start from some assumed function $T(\tau_0)$ and calculate $\Theta_0(\xi)$ subsequently adjusting the assumed $T(\tau_0)$ to obtain a good fit of the observations.

The first procedure is notoriously unstable (Twomey 1965) in the sense that the mathematical fitting procedures may produce unphysical results such as negative temperatures. Our final procedure was somewhere between the two extremes. We first attempted to fit the data $\Theta(\xi)$ with a polynomial in $\frac{1}{\xi}$:

$$\Theta(\xi) = \sum_{n=0}^{N} a_n \xi^{-n} . \qquad \text{(IV.2)}$$

The corresponding chromospheric temperature distribution $T(\tau_0)$ is

$$T(\tau_0) = \sum_{n=0}^{N} \frac{a_n}{n!} \tau_0^n . \qquad \text{(IV.3)}$$

It was not possible to find a polynomial approximation which satisfactorily represented all the data. The reason for this is clear: the range of values of $1/\xi$ is so large that the coefficients

of the polynomial are determined almost entirely by the values of Θ_0 at short wavelengths. The long wavelength data, where Θ_0 varies rapidly with $1/\xi$ cannot be fitted with the polynomial.

Thus we were led to divide the data into two overlapping ranges: 11-80μ and 50-180μ. We then fitted separate polynomials in $1/\xi$ to $\Theta(\xi)$ over these two ranges. It was possible to obtain a good fit of the data points which gave physically acceptable temperature distributions $T(\tau_0)$ in the two ranges of which contribute most to the spectrum in the corresponding spectral ranges. From the polynomial approximation for the first range, the correction for the failure of the Rayleigh-Jeans law

$$\Delta\Theta(\lambda,\xi) = \frac{\Phi(\lambda\Theta)}{4}\left[2\xi\frac{d\Theta}{d\xi} + \xi^2\frac{d^2\Theta}{d\xi^2}\right] \qquad (IV.4)$$

described in the second chapter was applied. This correction was very small -- at most 12° -- and was not applied except to the data from the 11μ filter. The polynomial approximation was then corrected for this change.

The two polynomial approximations to $T(\tau_0)$ did not agree in the region of overlap. This is not surprising since the fitting procedure can vary the temperature distributions radically near the

ends of the range to get the best fit over the major portion of the range. We fitted the two distributions together with a simple function which we adjusted to give the best spectrum in the 50-100 μ region. The function which best reproduced the observed spectrum over the entire range of data was

$$T(\tau_0) = 5185^\circ K \qquad \tau_0 \geq .01\,\mu^{-2} \qquad \text{(IV. 5a)}$$

$$T(\tau_0) = 4625.3 + 1.6655\times10^{5}\,\tau_0 - 1.4834\times10^{7}\,\tau_0^2 + 4.254\times10^{8}\,\tau_0^3 - 3.845\times10^{9}\,\tau_0^4 + 9.327\times10^{9}\,\tau_0^5 \qquad \text{(IV. 5b)}$$
$$.01 > \tau_0 \geq .00021$$

$$T(\tau_0) = 5062 + 110\log_{10}\tau_0 \qquad \text{(IV. 5c)}$$
$$.00021 > \tau_0 \geq .000063$$

$$T(\tau_0) = 4300 + 1500(\log_{10}\tau_0 + 4.4) \qquad \text{(IV. 5d)}$$
$$.000063 > \tau_0 \geq .000025$$

$$T(\tau_0) = 4002. - 3.196\times10^{6}\,\tau_0 + 6.842\times10^{10}\,\tau_0^2 - 1.2345\times10^{14}\,\tau_0^3 + 4.738\times10^{16}\,\tau_0^4 \qquad \text{(IV. 5e)}$$
$$.000025 > \tau_0 .$$

Equation IV. 5a represents a boundary condition on the model; it should not be taken to mean we believe the solar atmosphere to be isothermal below $\tau_0 = 10^{-2}$. Our data supply very little information on that region, and we could have equally well taken a more realistic approximation for that region without seriously affecting the model at higher levels. Equation IV. 5b and c represent the polynomials fitted to the data in the short and long wavelength regions respectively; equations IV. 5 c and d represent the

transition region. This temperature distribution is shown in Figure 15.

In determining the spectrum $\Theta_0(\xi)$ from the temperature distribution $T(\tau_0)$ to check the accuracy of the representation, a five term Gaussian quadrature was employed as described by Chandrasekhar (1960). The integral

$$\Theta_0(\xi) = \xi \int_0^\infty T(\tau_0) e^{-\xi\tau_0} d\tau_0 \qquad \text{(IV.6)}$$

is approximated by the sum

$$\Theta_0(\xi) \approx \sum_{i=1}^{5} a_i T\left(\frac{x_i}{\xi}\right) \qquad \text{(IV.7)}$$

where the x_i are the zeroes of the fifth Laguerre polynomial and the a_i are the corresponding Christoffel numbers, given by Chandrasekhar.

Figure 16 shows the measured values of $\Theta_0(\xi)$ with the results of the curve fitting.

The range of the chromosphere over which this approximation may be expected to apply must be determined. It does not hold where $\tau_0 \xi_{max} \ll 1$ because the opacity and hence emissivity of these regions is so low that they do not appreciably affect the longest wavelength radiation we observe; on the other hand,

radiation from regions where $\tau_0 \xi_{min} >> 1$ also is not observed since at even the shortest wavelengths we observe, it is almost all absorbed by the overlying layers. Since

$$\xi_{min} = 123\,\mu^2 \quad \text{and} \quad \xi_{max} = 32{,}500\,\mu^2$$

we may expect our temperature distribution $T(\tau_0)$ to apply over the range

$$10^{-5}\,\mu^2 \lesssim \tau_0 \lesssim 10^{-2}\,\mu^{-2}$$

The quantity $T(\tau_0)$ does not, of course, completely describe a model. We must specify also the other physical quantities such as density, pressure, composition, and electron pressure as a function of height or of optical depth. The variation of the other quantities must be deduced from $T(\tau_0)$ with the aid of physical laws, other experimental data, or assumptions.

Normally in constructing a model, one starts at $\tau = 0$ with the boundary conditions $P = \rho = 0$ and works inward. Our model does not extend to $\tau_0 = 0$, so we must decide on appropriate boundary conditions. The pressure at τ_0 depends upon the structure of the atmosphere above that point, about which our data give no information. For lack of any better assumption, we assume that the pressure P_0 at $\tau_{0_{min}}$ is given correctly by the Bilderberg model.

We assume, in common with other models of the low chromosphere, a homogeneous layer in hydrostatic equilibrium. We assume a composition of hydrogen and helium in the ratio 10:1 by number plus a fraction of heavier elements which is negligible in computing the pressure and density, but which serves as a source of electrons. Most of the free electrons come from the ionization of the small fraction of metals; sodium, for example, is more than 99.9% ionized throughout this region.

Since the infrared free-free opacity is proportional to the number density of free electrons as well as the number density of neutral hydrogen atoms, we must know the electron density to calculate τ_0. We cannot determine the electron density directly from our far infrared data. We have three alternatives: a) assume a composition for the atmosphere including the abundance of metals, and calculate the ionization equilibrium from Saha's equation, or, better yet, by non-LTE methods; b) use experimental data such as the eclipse measurements of scattering near $\lambda 4700\text{Å}$; or c) extract the electron density from some other model.

The first alternative requires essentially a complete solution of the chromospheric problem, which is beyond the scope of this paper. The second is inaccurate because of difficulties in fixing

the height scale and because of other sources of emission at $\lambda 4700\text{Å}$ such as emission from negative hydrogen ions or the Paschen continuum. Therefore we have adopted the third alternative: we assume that the electron density corresponding to a given hydrogen density is the same as in the BCA. This should be fairly accurate at depths $\tau_0 > 5\times10^{-5}\mu^{-2}$ where our temperature distribution does not differ greatly from the BCA. Moderately large errors may be expected in the vicinity of $\tau_0 = 2\times10^{-5}\mu^{-2}$.

With these assumptions, we may complete the model. Starting with P and T at $\tau_{0_{min}}$, we compute the number density of hydrogen from the ideal gas law and the assumed composition:

$$P = (n_H + n_{He})\,kT = 1.1\, n_H kT. \qquad \text{(IV.8)}$$

From the number density of hydrogen, we determine the electron number density from the BCA. Using the value of the free-free opacity given by John (1966), which we approximate to an accuracy of 1% by

$$K_\lambda = 8.472\times10^{-24}\,\lambda^2\, n_H\, p_e\, T^{-0.85} \quad \text{cm}^{-1}, \qquad \text{(IV.9)}$$

we calculate $d\tau_0/dz$ from

$$\frac{d\tau_0}{dz} = -\frac{K_\lambda}{\lambda^2}. \qquad \text{(IV.10)}$$

The pressure gradient is given by the hydrostatic balance equation

$$\frac{dP}{dz} = -\rho g, \qquad \text{(IV.11)}$$

and $\rho = n_H m_H + n_{He} m_{He} = 1.4 m_H n_H$,

so that

$$\frac{dP}{d\tau_0} = \frac{1.4\, g\, m_H}{8.472 \times 10^{-24}\, n_e\, k T^{0.15}} \quad . \qquad \text{(IV.12)}$$

We may now integrate this system numerically to obtain P, N_H, N_e, P, and z (measured from the starting point) over the range of τ_0 for which $T(\tau_0)$ is applicable.

The customary independent variable used in describing models is τ_5, the optical depth at λ 5000 Å rather than height because of the arbitrariness in determining the origin of the height scale. For comparison of our model with others, we have computed τ_5. We have arbitrarily fixed our height scale in addition so that it agrees with the BCA at $\tau_5 = 10^{-2}$. In computing the opacity at λ5000 Å we used the polynomial approximation given by Gingerich (1961).

Tables V and VI give the values of the various physical quantities at different levels in the chromosphere in this model. Table VII compares the properties of this model with the Bilderberg Continuum Atmosphere.

The details of this model must not be taken too seriously. It is

based on only one set of observations over a limited range. Furthermore, the process of inverting the observations to obtain the temperature profile is, as mentioned above, unstable in that small changes in the observed quantities can introduce large differences in the model. In addition, the computation of the complete model from the temperature profile is very unsophisticated and relies on some imperfect assumptions, particularly with regard to the electron density.

Nevertheless, we believe the divergence between this model and the BCA at the upper levels is real and that this model indicates the direction in which the BCA must be modified to fit the real sun, that is, a fairly steep drop in temperature near $\tau_5 = 10^{-3}$ above an almost isothermal region with $T \approx 4600^{\circ}$, followed by a cooler, higher region.

The results reported here decrease in reliability as they proceed further from the direct observations. We believe that the limb darkening curves are reliable, especially from the channel A filters. The spectrum computed from these curves is less reliable because of the cumulative effect on the errors of attaching the start of one curve on the end of the preceding one. The temperature vs. optical depth curve is still less reliable because of

the mathematical difficulties of the inversion process. Finally the complete model is still less reliable in its details because of the inaccuracy of the assumptions.

The quantitative conclusions of this work are primarily included in the appended tables and graphs; qualitatively the principal conclusions are that the 4600° minimum of the BCA represents a plateau rather than a true minimum and that the true minimum temperature is a lower value which occurs higher in the chromosphere.

Clearly there is still significant uncertainty in the solar far infrared spectrum, especially at wavelengths greater than 100 μ, and consequently there is still significant uncertainty in the temperature structure of the lower chromosphere.

In addition, variation of the chromospheric temperature structure with the solar cycle has not been investigated at all. Practically all the infrared measurements have been made within the past three years and so represent conditions near the maximum solar activity. Another decade's observations are needed to answer this problem.

A related problem is the infrared radiation from active features. How do sunspots and flares, for example, affect the infrared spectrum. It is possible that the data from this balloon flight will give some results about active features when the scans are analyzed individually and scans where the slit crossed an active feature compared with scans where it did not. No active features are apparent in the averaged scans. This experiment was not designed to observe such small regions of the sun as a single sunspot, so it is not surprising that none were seen.

The promising directions for future work of this nature seem to be in increasing the absolute accuracy, going to longer wavelengths, using higher spatial resolution to observe active features and investigate the assumption of spherical symmetry, and observing long term variations in the spectrum.

TABLES

TABLE 1

Comparison of free-free absorption coefficient $\kappa_1(T)$ (defined by equation II. 7) in units of $cm^4 \cdot dyne^{-1}$-$micron^{-2}$ as calculated by various investigators.

	Temperature	
	6300°K	4200°K
Menzel and Pekeris (1935)	0.555×10^{-27}	0.693×10^{-27}
Wheeler and Wildt (1942)	3.31	3.11
Chandrasekhar and Breen (1946)	6.98	12.19
Ohmura and Ohmura (1960)	4.46	6.50
Geltman (1956)	5.06	7.11
John (1964)	5.05	7.58
John (1966)	5.00	7.12

TABLE II

Effective wavelengths of the filters used in observing the solar far infrared limb darkening, defined by equation II.1.

Filter	λ_0	$\Delta\lambda$ (FWHM)
Interference	11.1	.32
Magnesium Oxide	18	9
Sodium Fluoride	31	7
Sodium Chloride	52	15
Potassium Bromide	85	20
Cesium Bromide	115	45

TABLE III

Effective wavelength range spanned by filters

Filter	λ_0	μ_{min}	$\lambda_0/\sqrt{\mu_{min}}$
Interference	11	.169	27
MgO	18	.169	44
NaF	31	.290	58
NaCl	52	.306	94
KBr	85	.377	138
CsBr	115	.427	176

TABLE IV

The far infrared limb darkening and the spectrum deduced from it. For each filter the following columns are given:

μ: cosine of zenith angle on sun.

λ_{equiv}: equivalent wavelength at center of disk = $\lambda_0/\sqrt{\mu}$.

$B_\lambda(\mu)/B_\lambda(1)$: solar radiance at μ relative to value in center of disk.

ΔB: estimated uncertainty in preceding column due to both random and systematic errors.

Θ: brightness temperature of sun at λ and μ, equal to the brightness temperature at center of disk at wavelength λ_{equiv}.

$\Delta\Theta$: estimated uncertainty in Θ, including both uncertainty in $\Theta(\mu = 1)$ and in $B_\lambda(\mu)/B_\lambda(1)$.

Interference Filter

μ	λ_{equiv}	$B_\lambda(\mu)/B_\lambda(1)$	ΔB	Θ	$\Delta\Theta$
1.000	11.1	1	--	5036	30
.990	11.1	1.0017	.0050	5044	55
.972	11.2	1.0007	.0050	5039	55
.905	11.7	.9963	.0050	5019	55
.853	12.0	.9935	.0050	5007	55
.787	12.5	.9915	.0050	4998	55
.701	13.3	.9890	.0050	4986	55
.649	13.9	.9860	.0050	4973	55
.588	14.5	.9816	.0050	4954	55
.532	15.2	.9795	.0054	4945	57
.500	15.7	.9770	.0058	4934	60
.465	16.3	.9761	.0063	4930	61
.427	17.0	.9731	.0071	4918	63
.406	17.4	.9722	.0076	4914	64
.384	17.9	.9701	.0082	4903	66
.360	18.5	.9694	.0090	4901	70
.334	19.2	.9677	.0101	4892	75

TABLE IV (cont'd)

Interference Filter

μ	λ_{equiv}	$B_\lambda(\mu)/B_\lambda(1)$	ΔB	Θ	ΔΘ
.306	20.1	.9679	.0119	4892	84
.209	20.6	.9678	.0130	4892	88
.274	21.2	.9671	.0145	4890	95
257	21.9	.9630	.0165	4871	105
.238	22.7	.9593	.0196	4852	120
.217	23.8	.9504	.0252	4816	145
.195	25.2	.9406	.0362	4773	195
.169	27.0	.9455	.0554	4794	285

Magnesium Oxide Filter

μ	λ_{equiv}	$B_\lambda(\mu)/B_\lambda(1)$	ΔB	Θ	ΔΘ
1.000	18.0	1	--	4905	70
.972	18.2	1.0018	.0050	4913	95
.905	18.9	.9975	.0050	4896	95
.853	19.5	.9966	.0050	4890	95
.787	20.3	.9942	.0050	4878	95
.701	21.5	.9900	.0050	4860	95
.588	23.5	.9845	.0050	4835	95
.532	24.7	.9848	.0058	4836	100
.500	25.4	.9835	.0063	4830	102
.465	26.4	.9781	.0074	4806	105
.427	27.6	.9808	.0089	4818	110
.406	28.3	.9806	.0098	4817	115
.384	29.0	.9810	.0109	4819	120
.360	30.0	.9796	.0122	4812	125
.334	31.1	.9777	.0141	4804	135
.306	32.5	.9786	.0163	4807	145
.290	33.5	.9772	.0177	4802	150
.274	34.4	.9727	.0196	4781	160
.257	35.5	.9713	.0221	4775	170
.238	36.9	.9621	.0259	4733	190
.217	38.6	.9479	.0316	4669	215
.195	40.8	.9283	.0415	4536	260
.169	43.8	.9346	.0577	4609	335

TABLE IV (Cont'd)

Sodium Fluoride Filter

μ	λ_{equiv}	$B_\lambda(\mu)/B_\lambda(1)$	ΔB	Θ	ΔΘ
1.000	31.1	1	--	4806	135
.972	31.4	1.0011	.0050	4810	160
.905	32.6	.9966	.0050	4788	160
.853	33.6	.9923	.0050	4771	160
.787	35.0	.9890	.0050	4757	160
.701	37.1	.9860	.0050	4742	160
.588	40.5	.9787	.0050	4709	160
.532	42.5	.9788	.0063	4709	165
.500	43.7	.9794	.0076	4713	170
.465	45.3	.9819	.0095	4723	180
.427	47.3	.9834	.0124	4729	190
.406	48.4	.9840	.0143	4732	200
.384	49.8	.9866	.0167	4745	210
.360	51.4	.9912	.0202	4766	225
.334	53.5	.9975	.0252	4797	250
.306	55.8	1.0069	.0326	4838	285
.290	57.5	1.0004	.0375	4807	310

Sodium Chloride Filter

μ	λ_{equiv}	$B_\lambda(\mu)/B_\lambda(1)$	ΔB	Θ	ΔΘ
1.000	52.0	1	--	4720	225
.972	52.7	.9984	.0050	4712	250
.905	54.6	.9996	.0050	4718	250
.853	56.3	.9997	.0057	4718	250
.787	58.6	.9994	68	4717	255
.701	62.1	.9975	85	4708	265
.649	64.5	1.0012	101	4726	275
.588	67.8	.9992	124	4716	280
.532	71.3	.9976	150	4708	295
.500	73.5	1.0030	167	4734	300
.465	76.2	.9915	190	4681	315
.427	79.6	.9871	223	4661	325
.406	81.6	.9862	249	4656	340
.384	83.9	.9861	283	4656	355
.360	86.7	.9886	329	4667	375
.334	90.0	.9891	395	4670	405
.306	94.0	.9989	494	4716	450

TABLE IV (cont'd)

Potassium Bromide Filter

μ	λ_{equiv}	$B_\lambda(\mu)/B_\lambda(1)$	ΔB	θ	$\Delta\theta$
1.00	85	1.0050	.0281	4608	450
1.00	85	.9877	.0300	4530	460
1.00	85	.9981	.0376	4576	475
1.00	85	.9545	.0366	4380	470
1.00	85	.9634	.0372	4420	470
1.00	85	1.0240	.0404	4693	485
1.00	85	.9974	.0393	4573	480
.99	86	1.0200	.0401	4675	485
.98	86	1.0422	.0378	4775	475
.95	87	1.0179	.0394	4666	480
.94	88	1.0116	.0354	4637	460
.91	89	1.0148	.0343	4652	455
.86	92	1.0168	.0402	4661	485
.80	95	.9955	.0356	4565	460
.72	100	.9687	.0406	4444	485
.68	103	.9594	.0406	4402	485
.62	108	.9250	.0464	4247	500
.58	111	.9240	.0513	4243	520
.54	116	.9528	.0519	4373	520
.50	121	.9269	.0528	4256	525
.47	124	.8926	.0550	4102	525
.44	128	.9304	.0649	4272	580
.40	134	.9076	.0814	4169	640
.38	138	.8768	.0869	4030	650

Cesium Bromide Filter

μ	λ_{equiv}	$B_\lambda(\mu)/B_\lambda(1)$	ΔB	θ	$\Delta\theta$
1.00	115	.9748	.0282	4120	515
1.00	115	.9732	.0286	4113	515
1.00	115	.9910	.0299	4188	525
1.00	115	1.0195	.0303	4306	525
1.00	115	1.0045	.0290	4244	520
1.00	115	.9958	.0238	4208	500
1.00	115	1.0212	.0334	4313	535
.99	116	1.0056	0337	4248	535
.98	116	1.0099	.0314	4266	530
.97	117	1.0064	.0283	4252	515

TABLE IV (cont'd)

Cesium Bromide Filter					
μ	λ_{equiv}	$B_\lambda(\mu)/B_\lambda(1)$	ΔB	Θ	$\Delta\Theta$
.95	118	1.0466	.0352	4419	545
.94	118	1.0034	.0297	4239	525
.91	120	1.0256	.0264	4332	510
.87	123	.9843	.0340	4160	540
.81	128	1.0118	.0310	4274	530
.68	140	.9780	.0424	4133	575
.62	146	.9521	.0360	4026	550
.59	150	.9760	.0474	4125	590
.54	156	.8854	.0495	3748	600
.50	163	.9278	.0587	3924	640
.47	167	.9497	.0649	4016	665
.44	172	.9824	0725	4152	700
.43	175	.9084	.0750	3844	700

TABLE V

Model of lower chromosphere based on far infrared limb darkening measurements.

TAU 0 = reference optical depth, τ_λ/λ^2.

TEMP = electron temperature .

CGS GAS PRESSURE = total pressure in dynes/cm^2.

ELECTRON PRESSURE = electron pressure in dynes/cm^2.

HEIGHT = height in km above arbitrary reference level, adjusted to agree with BCA at $\tau_5 = 10^{-2}$.

TAU 5 = optical depth at λ5000Å.

TAU 0	TEMP	CGS GAS PRESSURE	ELECTRON PRESSURE	HEIGHT (KM)	TAU 5
.000010	3977.	6.198E+02	7.410E-02	605.8	.000199
.000013	3972.	9.044E+02	8.468E-02	569.5	.000268
.000016	3968.	1.218E+03	9.642E-02	541.0	.000355
.000020	3964.	1.565E+03	1.095E-01	517.2	.000465
.000025	4000.	1.950E+03	1.247E-01	496.3	.000603
.000032	4150.	2.383E+03	1.432E-01	476.8	.000762
.000040	4300.	2.872E+03	1.640E-01	457.9	.000939
.000050	4450.	3.427E+03	1.874E-01	439.4	.001137
.000063	4600.	4.057E+03	2.139E-01	421.2	.001360
.000079	4611.	4.765E+03	2.422E-01	403.5	.001608
.000100	4622.	5.554E+03	2.739E-01	386.6	.001952
.000126	4633.	6.435E+03	3.097E-01	370.4	.002363
.000158	4644.	7.418E+03	3.500E-01	354.6	.002877
.000200	4655.	8.515E+03	3.955E-01	339.3	.003518
.000251	4686.	9.743E+03	4.472E-01	324.3	.004310
.000316	4686.	1.111E+04	5.052E-01	309.5	.005300
.000398	4689.	1.264E+04	5.708E-01	295.1	.006546
.000501	4705.	1.435E+04	6.450E-01	281.0	.008105
.000631	4724.	1.625E+04	7.292E-01	267.0	.010044
.000794	4748.	1.838E+04	8.250E-01	253.1	.012450
.001000	4777.	2.076E+04	9.342E-01	239.2	.015424
.001259	4812.	2.341E+04	1.060E+00	225.5	.019089
.001585	4853.	2.638E+04	1.204E+00	211.7	.023687
.001995	4902.	2.969E+04	1.373E+00	198.0	.029365
.002512	4956.	3.336E+04	1.572E+00	184.3	.035778
.003162	5016.	3.744E+04	1.810E+00	170.6	.043899
.003981	5079.	4.193E+04	2.098E+00	157.0	.053731
.005012	5138.	4.683E+04	2.454E+00	143.5	.065643
.006310	5186.	5.213E+04	2.904E+00	130.3	.080143
.007943	5210.	5.777E+04	3.486E+00	117.6	.097982
.010000	5185.	6.365E+04	4.272E+00	105.6	.120347

TABLE VI

Model of lower chromosphere.

TAU 0	=	reference optical depth.
MASS DENSITY	=	density in gm/cm^3.
ELECTRON DENSITY	=	number of free electrons per cm^3.
HYDROGEN DENSITY	=	number of neutral hydrogen atoms per cm^3.
OPACITY	=	$\kappa_1(T)p_e n_{II} = \kappa_\lambda \rho/\lambda^2$.

TAU 0	MASS DENSITY	ELECTRON DENSITY	HYDROGEN DENSITY	OPACITY
.000010	2.399E-09	1.350E+11	1.026E+15	5.617E-13
.000013	3.505E-09	1.544E+11	1.499E+15	9.386E-13
.000016	4.726E-09	1.760E+11	2.022E+15	1.443E-12
.000020	6.078E-09	2.001E+11	2.600E+15	2.109E-12
.000025	7.504E-09	2.258E+11	3.210E+15	2.941E-12
.000032	8.838E-09	2.499E+11	3.781E+15	3.855E-12
.000040	1.028E-08	2.762E+11	4.399E+15	4.984E-12
.000050	1.186E-08	3.051E+11	5.072E+15	6.381E-12
.000063	1.358E-08	3.369E+11	5.808E+15	8.104E-12
.000079	1.591E-08	3.804E+11	6.805E+15	1.073E-11
.000100	1.850E-08	4.293E+11	7.914E+15	1.409E-11
.000126	2.138E-08	4.842E+11	9.147E+15	1.837E-11
.000158	2.459E-08	5.460E+11	1.052E+16	2.383E-11
.000200	2.816E-08	6.155E+11	1.205E+16	3.078E-11
.000251	3.201E-08	6.913E+11	1.369E+16	3.934E-11
.000316	3.651E-08	7.810E+11	1.562E+16	5.069E-11
.000398	4.150E-08	8.818E+11	1.775E+16	6.506E-11
.000501	4.694E-08	9.931E+11	2.008E+16	8.290E-11
.000631	5.295E-08	1.118E+12	2.265E+16	1.054E-10
.000794	5.958E-08	1.259E+12	2.549E+16	1.336E-10
.001000	6.688E-08	1.417E+12	2.861E+16	1.689E-10
.001259	7.490E-08	1.595E+12	3.204E+16	2.132E-10
.001585	8.367E-08	1.798E+12	3.579E+16	2.688E-10
.001995	9.323E-08	2.029E+12	3.989E+16	3.385E-10
.002512	1.036E-07	2.298E+12	4.433E+16	4.260E-10
.003162	1.149E-07	2.613E+12	4.915E+16	5.392E-10
.003981	1.271E-07	2.992E+12	5.436E+16	6.842E-10
.005012	1.403E-07	3.460E+12	6.002E+16	8.750E-10
.006310	1.547E-07	4.056E+12	6.620E+16	1.133E-09
.007943	1.707E-07	4.847E+12	7.302E+16	1.494E-09
.010000	1.890E-07	5.969E+12	8.084E+16	2.036E-09

TABLE VII

Comparison of model based on present work (MS) with Bilderberg Continuum Atmosphere (BCA)

τ_5	Temperature (°K)		τ_0 (μ^{-2})		Pressure (dyne-cm^{-2})		Height (km)	
	MS	BCA	MS	BCA	MS	BCA	MS	BCA
.0003	3970	4620	.0000143	.0000199	1.09×10^3	2.15×10^3	550	481
.0010	4365	4600	.0000426	.0000622	3.04×10^3	4.25×10^3	449	407
.0032	4650	4600	.000177	.000200	7.88×10^3	8.14×10^3	347	337
.0100	4724	4610	.000631	.000643	1.63×10^4	1.36×10^4	267	267
.0316	4923	4800	.00218	.00217	3.10×10^4	2.95×10^4	193	197
.1000	5200	5140	.00811	.00809	5.85×10^4	5.52×10^4	116	124

TABLE VIII

Solar far infrared spectrum computed from new model of lower chromosphere compared with the observations.

λ = wavelength in microns.

Θ_m = solar brightness temperature deduced from limb darkening measurements

Θ_c = solar brightness temperature computed from the model

λ	Θ_m	Θ_c
10	5058	5072
15	4965	4984
20	4890	4893
25	4824	4825
30	4776	4783
35	4742	4756
40	4717	4714
45	4700	4694
50	4687	4677
55	4687	4664
60	4687	4653
65	4687	4643
70	4687	4591
75	4687	4543
80	4687	4499
85	4635	4444
90	4564	4402
95	4492	4363
100	4424	4326
110	4308	4286
120	4218	4284
130	4152	4280
140	4104	4279
150	4070	4276
160	4044	4243
170	4026	4212
180	4013	4183

FIGURES

FIGURE 1

The variation of the opacity coefficient with temperature, according to the results of John (1966).

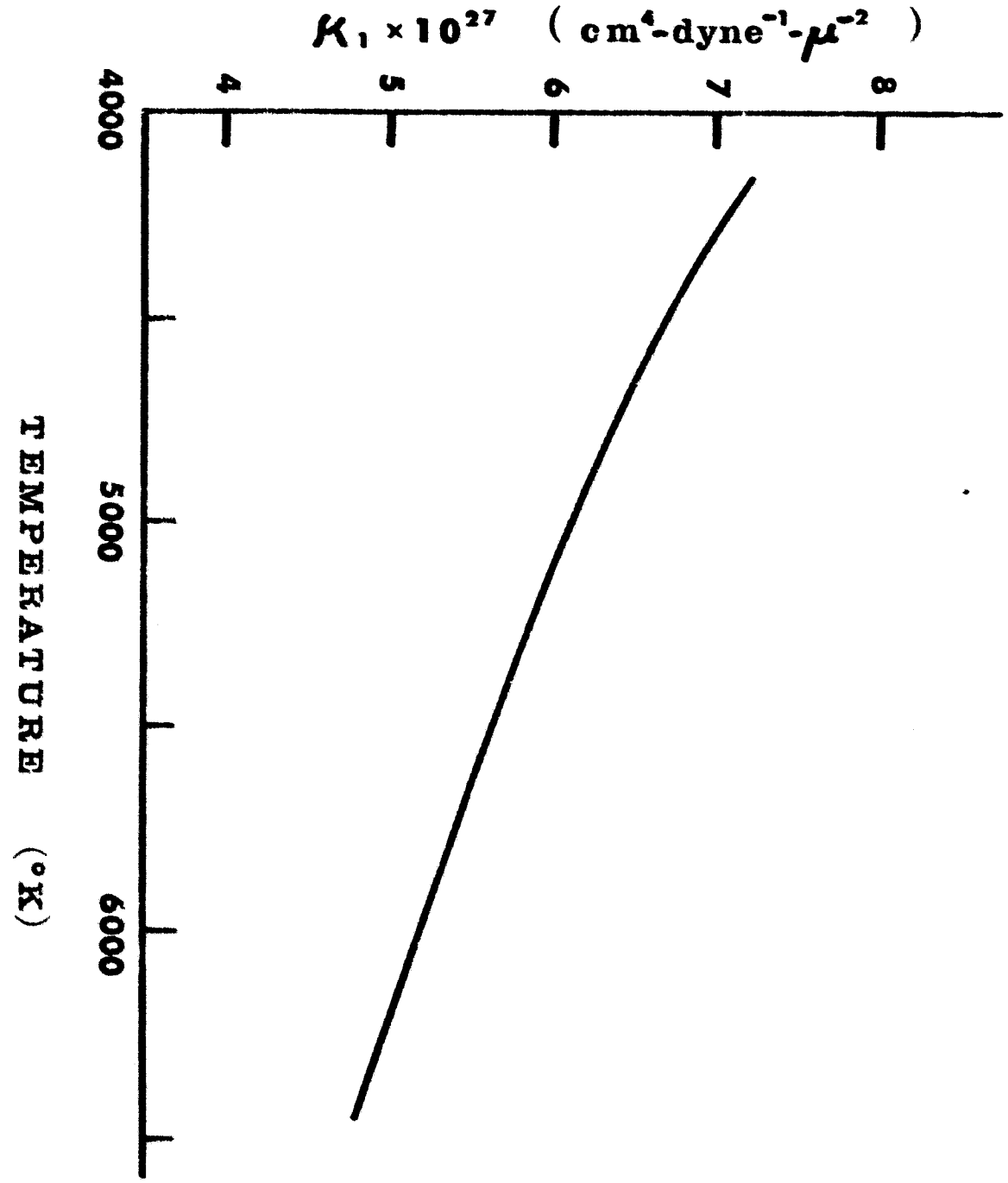
$K_1 \times 10^{27}$ (cm^4-$dyne^{-1}$-μ^{-2})
4
5
6
7
8
4000
5000
6000
TEMPERATURE (°K)

FIGURE 2

The balloon borne instrument, shown without housing or batteries.

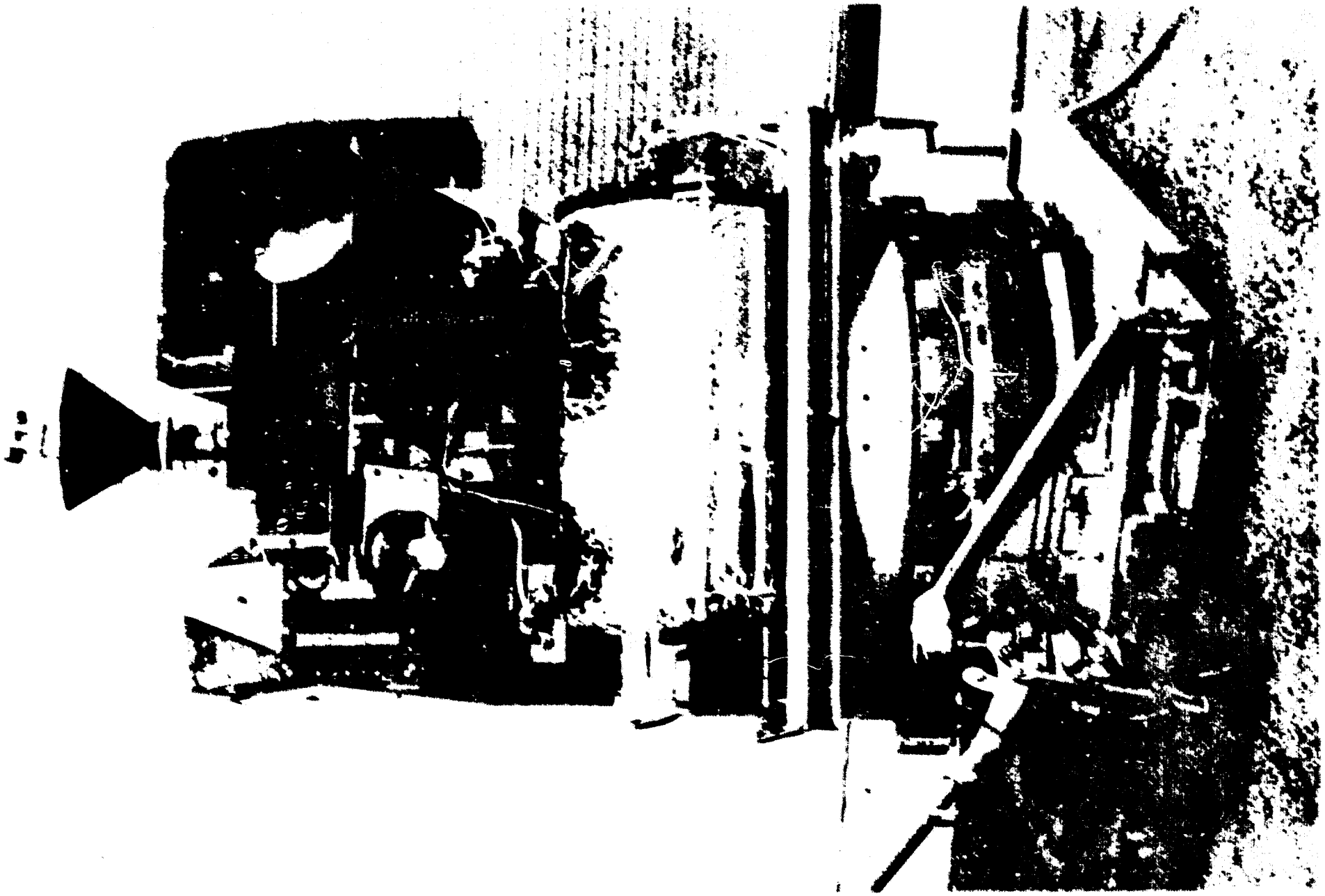

FIGURE 3

Optical diagram of the Newtonian telescope.

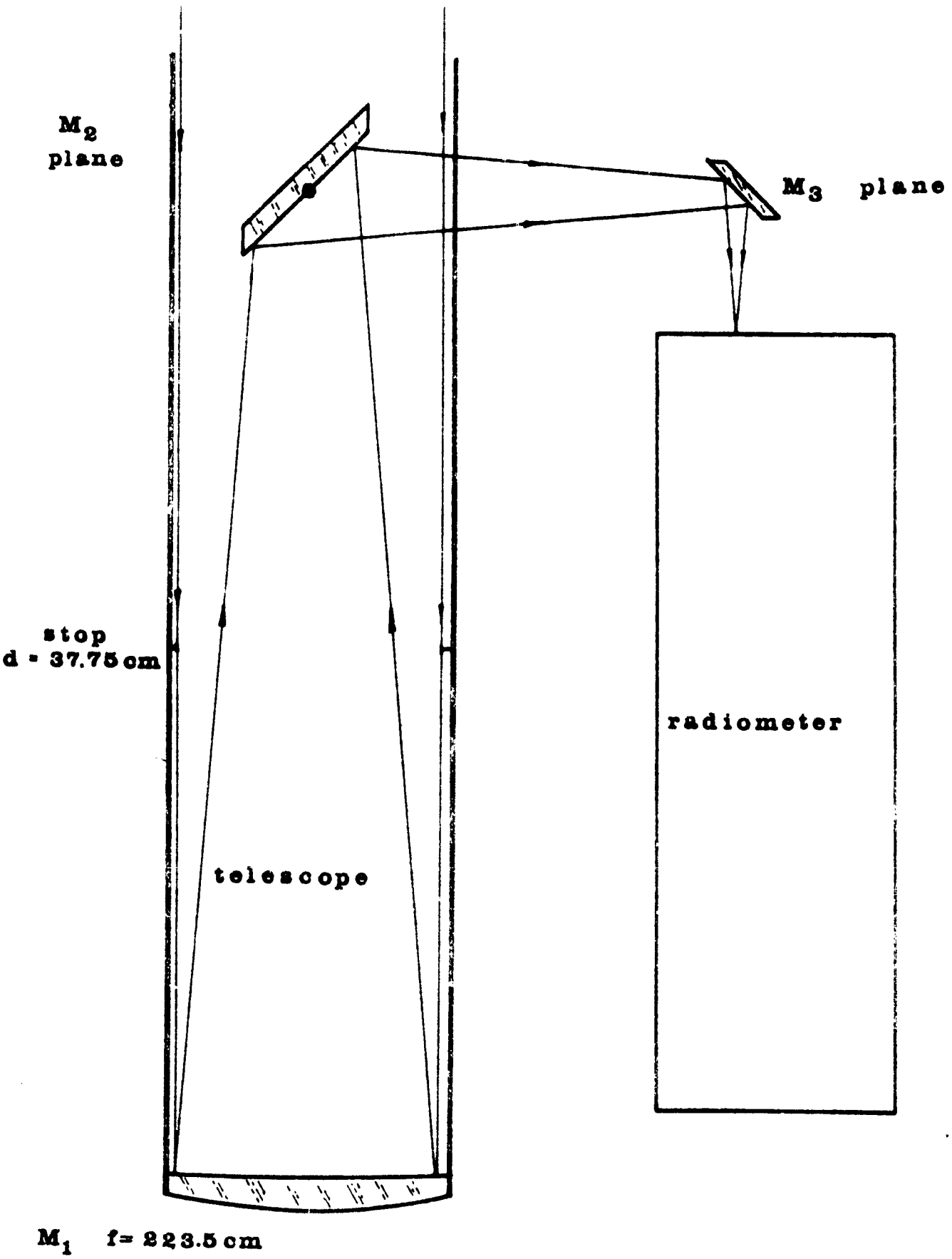

TELESCOPE OPTICS

FIGURE 4

Optical diagram of far infrared filter radiometer.

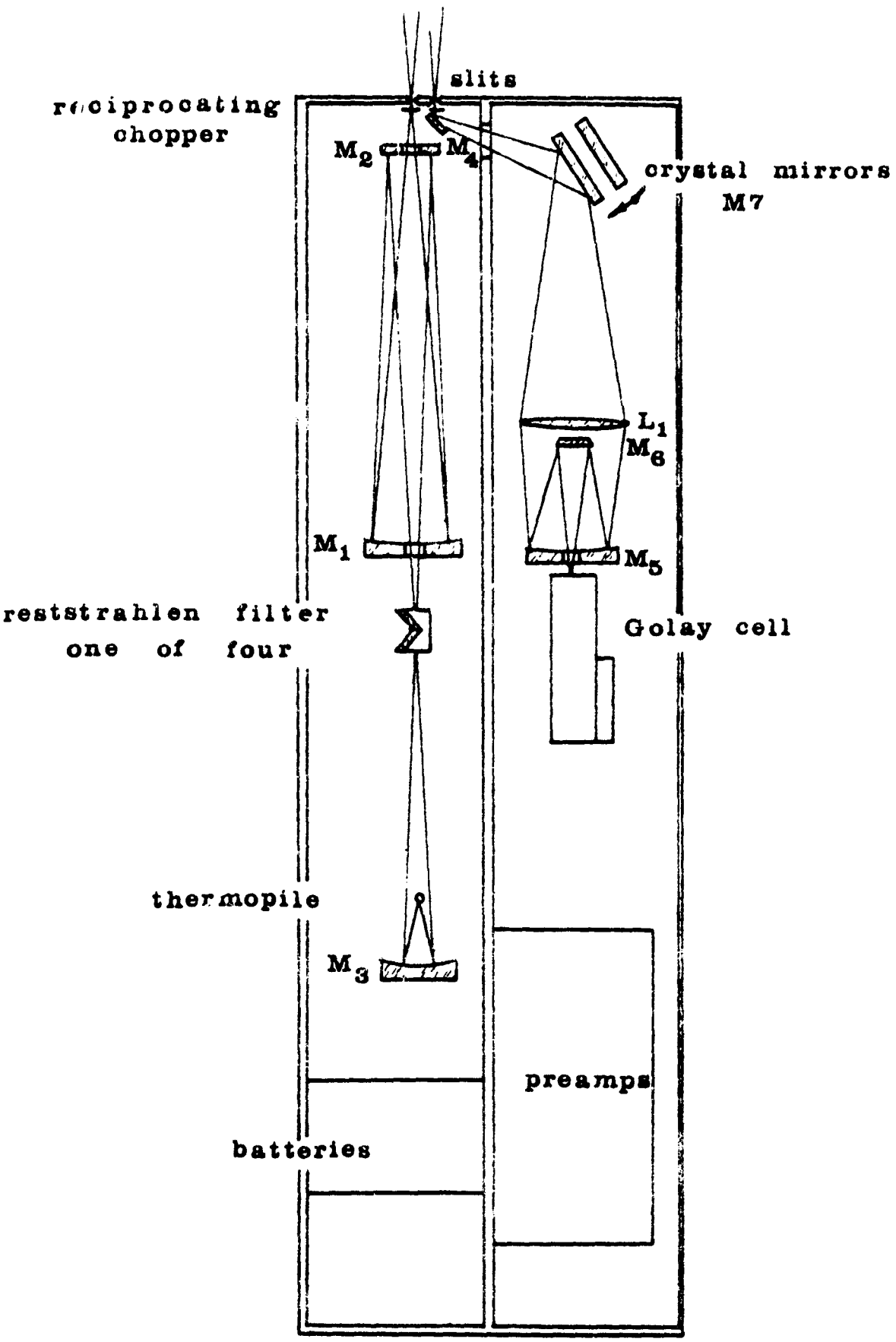

RADIOMETER OPTICS

FIGURE 5

The four crystal reststrahlen filter.

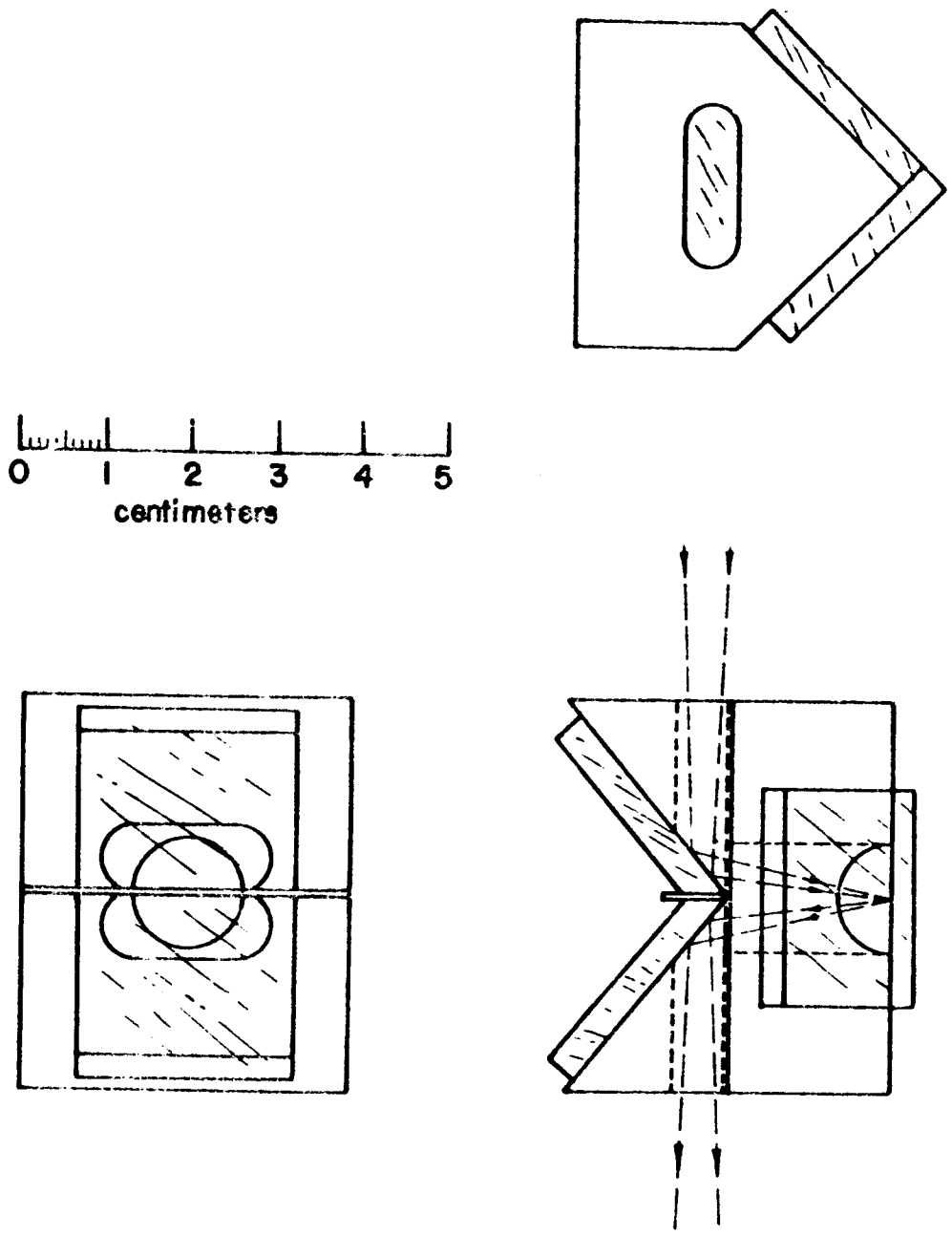
0 1 2 3 4 5
centimeters

FIGURE 6

Measured transmission of the reststrahlen filter with four magnesium oxide crystals (solid curve) compared with the calculated transmission (dashed curve) based on the measurements of Madden (1956).

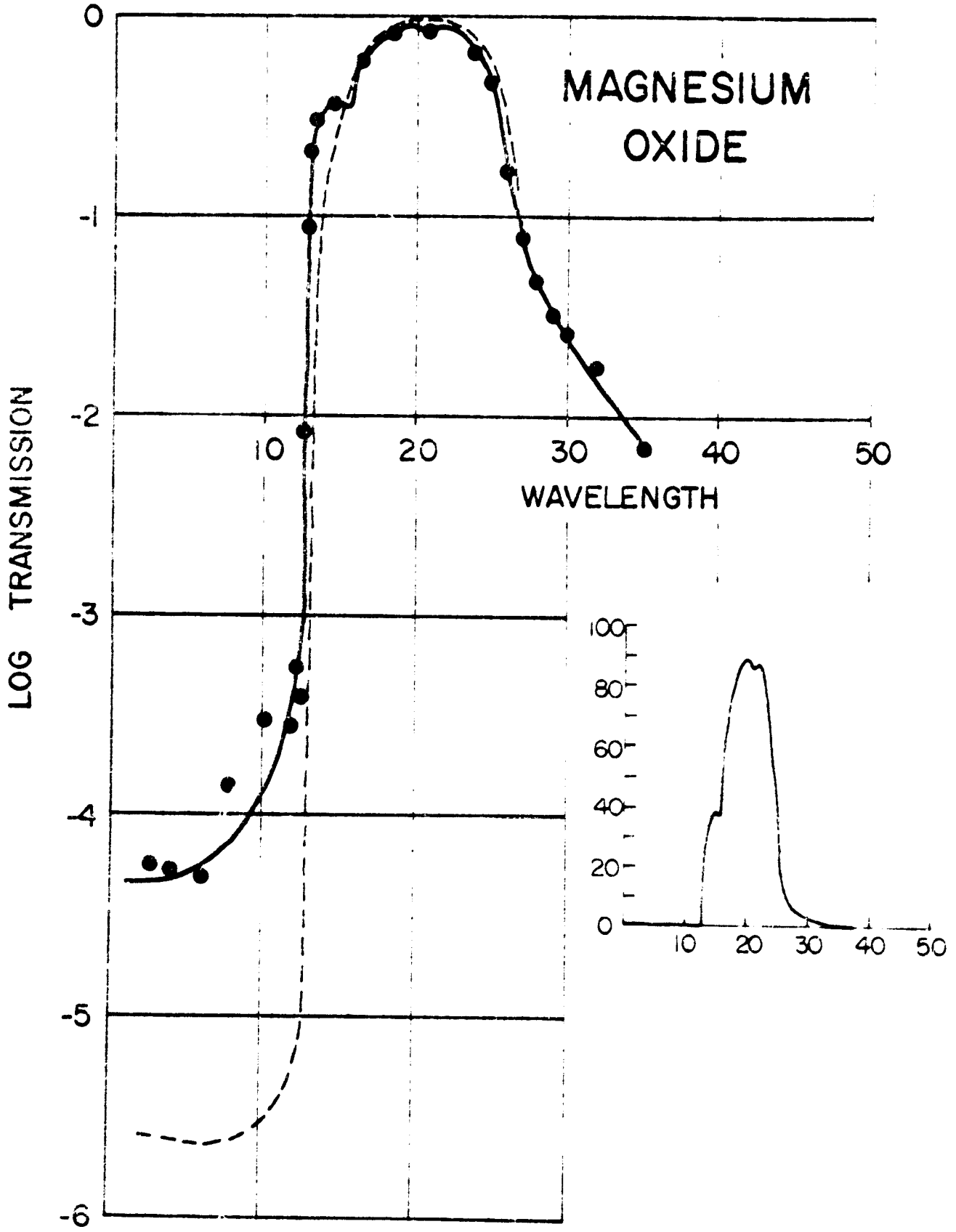
MAGNESIUM
OXIDE
LOG TRANSMISSION
WAVELENGTH
0
-1
-2
-3
-4
-5
-6
10
20
30
40
50
100
80
60
40
20
0

FIGURE 7

Transmission of the filters used in channel A of the far infrared filter radiometer.

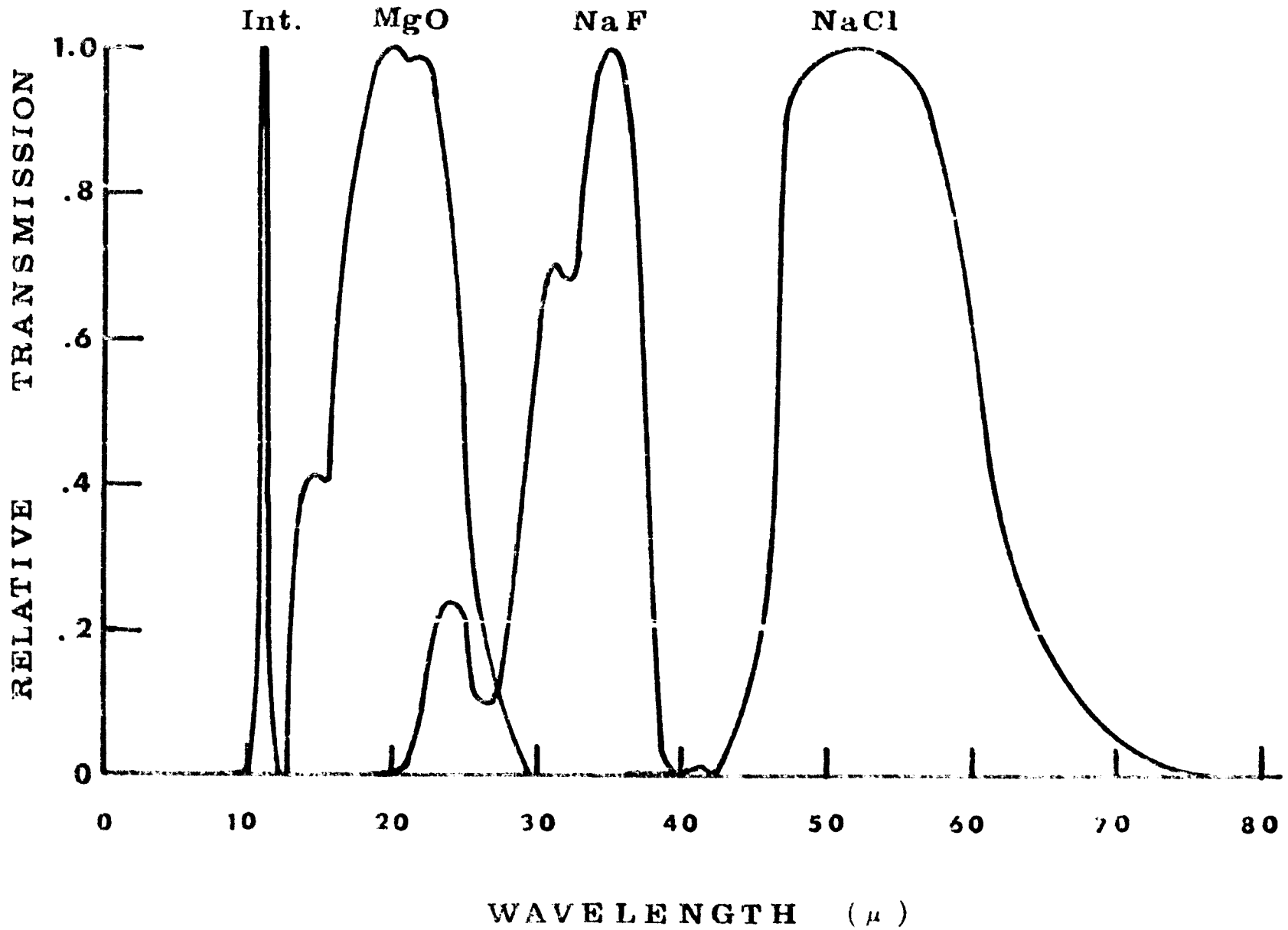
Int.
MgO
NaF
NaCl
TRANSMISSION
RELATIVE
1.0
.8
.6
.4
.2
0
0
10
20
30
40
50
60
70
80
WAVELENGTH (μ)

FIGURE 8

Transmission of the filters used in channel B of the far infrared filter radiometer.

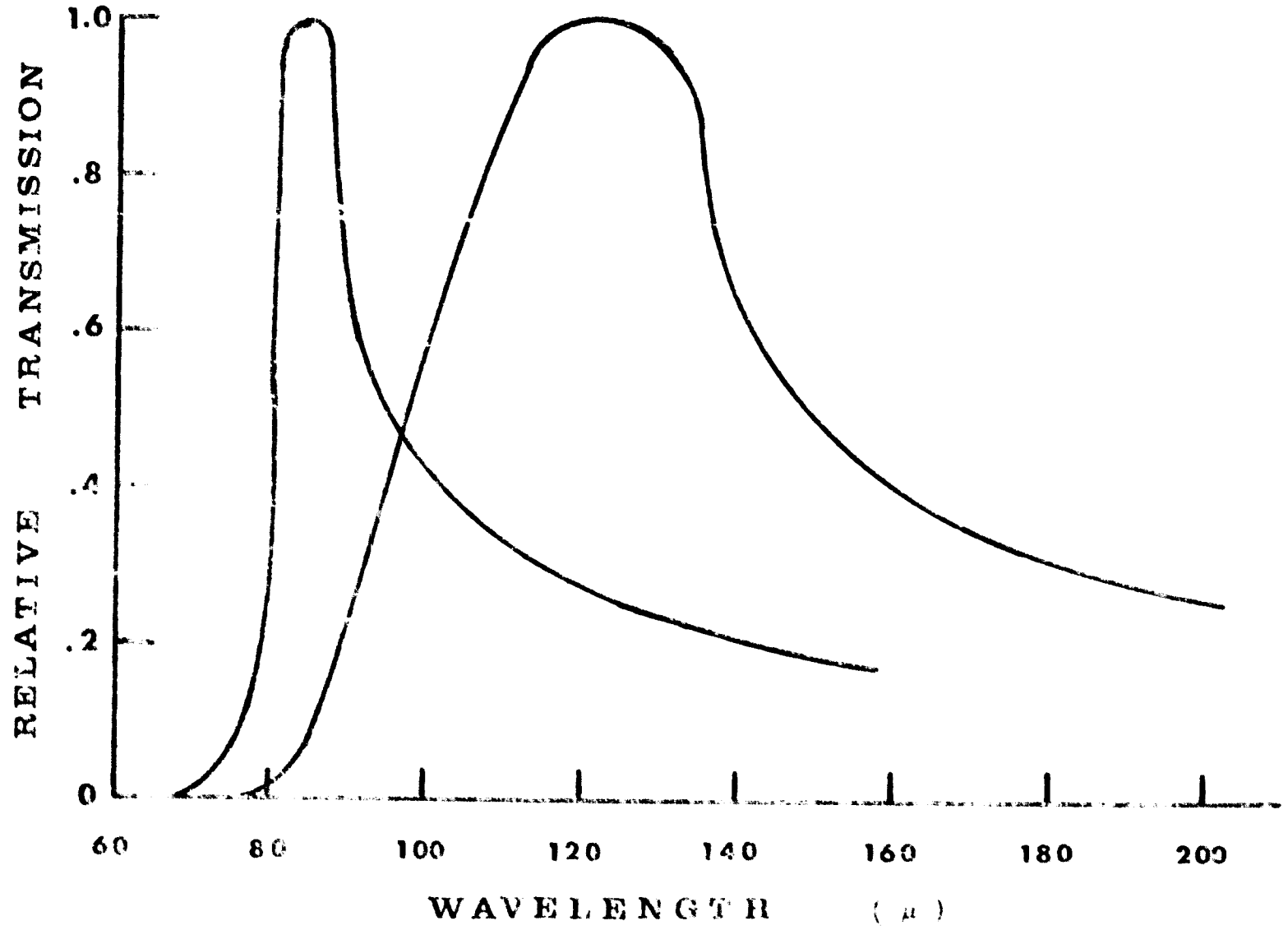
TRANSMISSION
RELATIVE
1.0
.8
.6
.4
.2
0
60
80
100
120
140
160
180
200
WAVELENGTH (μ)

FIGURE 9

Schematic diagram of variable gain synchronous rectifier amplifier.

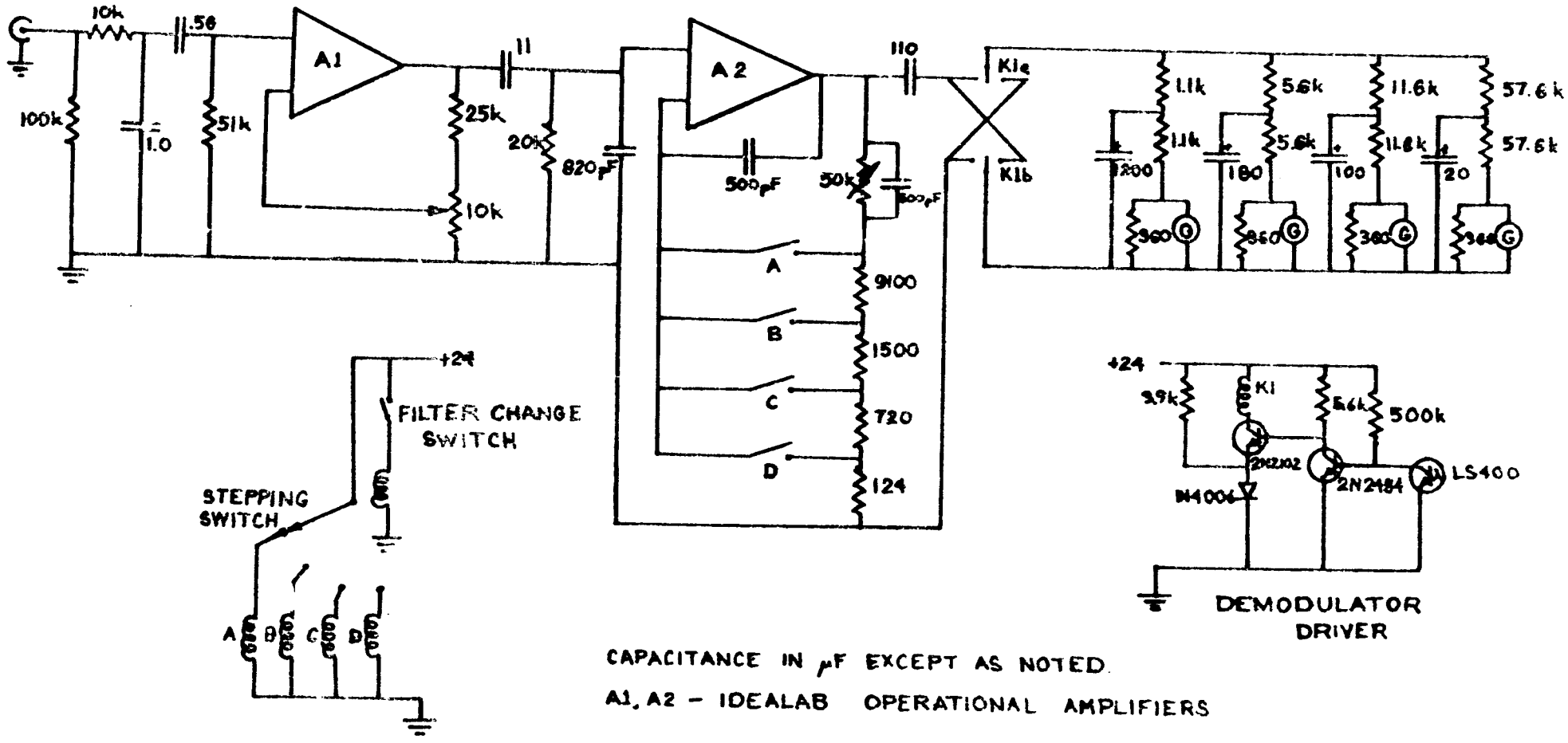

CAPACITANCE IN μF EXCEPT AS NOTED.

A1, A2 – IDEALAB OPERATIONAL AMPLIFIERS

FIGURE 10

Test of linearity of system response.

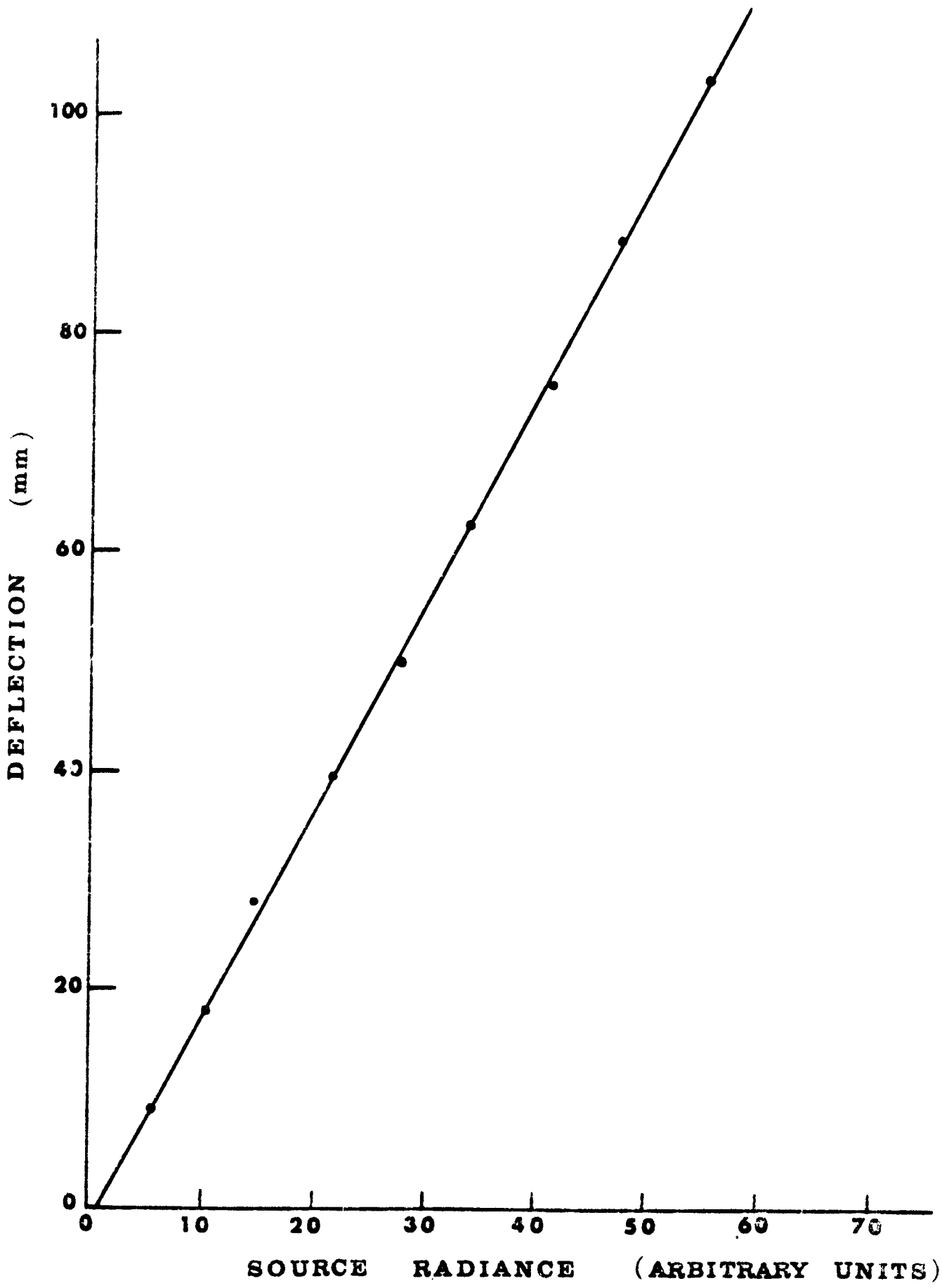
DEFLECTION (mm)
100
80
60
40
20
0
0
10
20
30
40
50
60
70
SOURCE RADIANCE (ARBITRARY UNITS)

FIGURE 11

Correction applied to the data for the effects of the scanning function, based on measurements at 18μ.

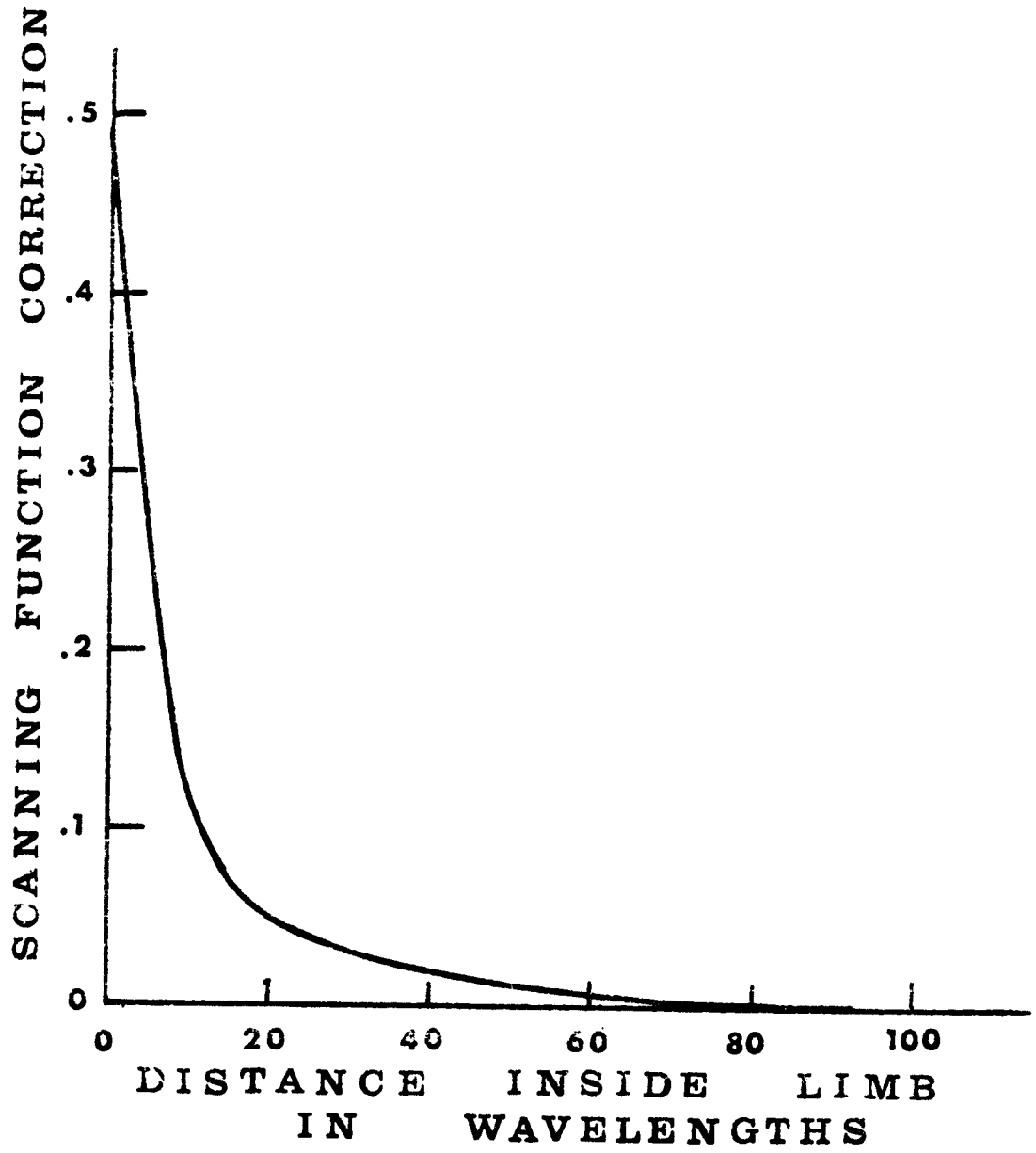
SCANNING FUNCTION CORRECTION
.5
.4
.3
.2
.1
0
0
20
40
60
80
100
DISTANCE INSIDE LIMB
IN WAVELENGTHS

FIGURE 12

Variation of temperature at various points in the instrument during flight :

———— near central stem;

- - - - - - near outside wall ;

— - — - inside electronics tank.

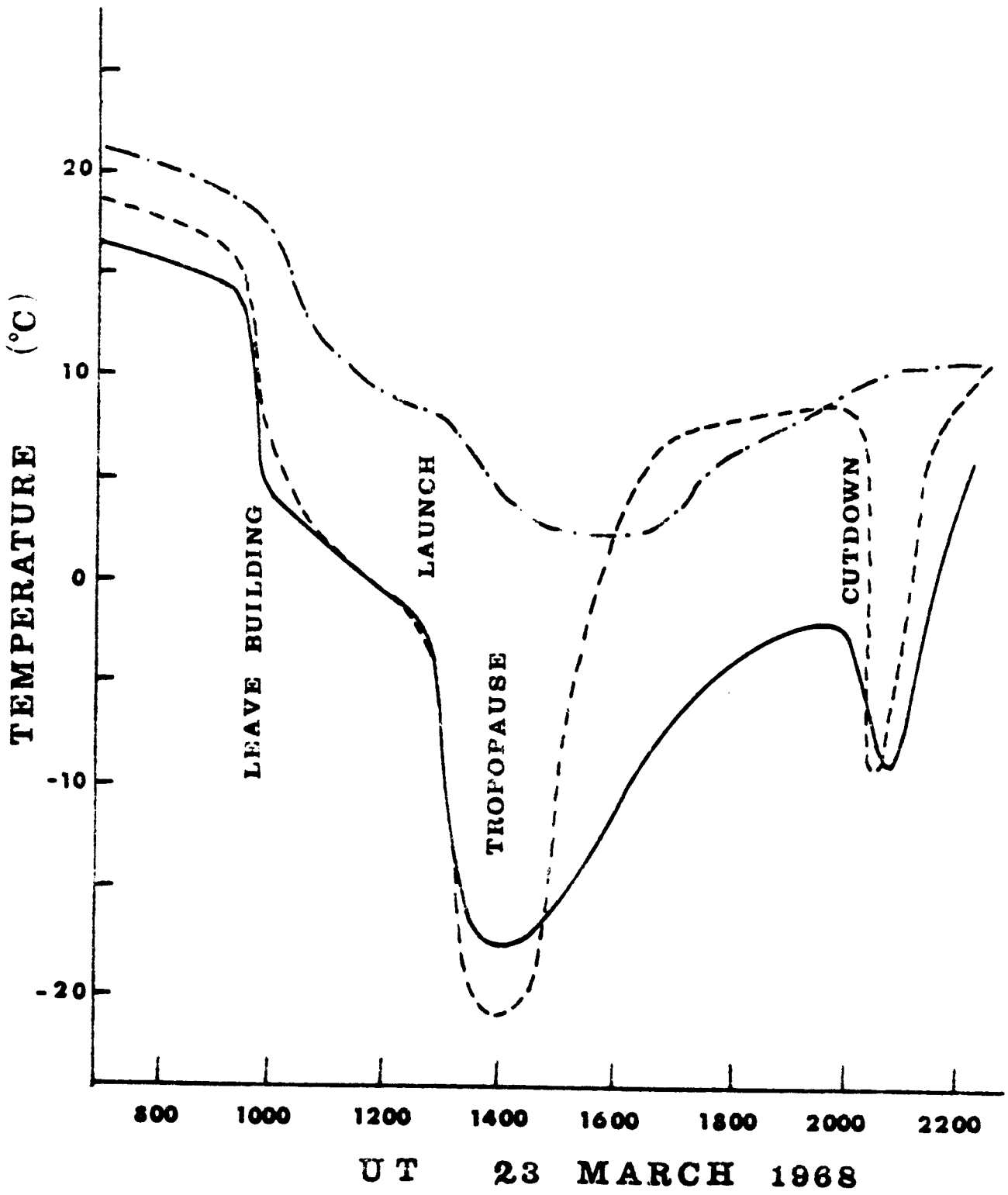
TEMPERATURE (°C)
20
10
0
-10
-20
LEAVE BUILDING
LAUNCH
TROPOPAUSE
CUTDOWN
800
1000
1200
1400
1600
1800
2000
2200
UT 23 MARCH 1968

FIGURE 13

The limb darkening is the far infrared. Circles represent average of data from 20-40 scans. Solid lines are results of fitting a smooth spectrum to all the data. Ordinates of the various curves have been displaced vertically for clarity.

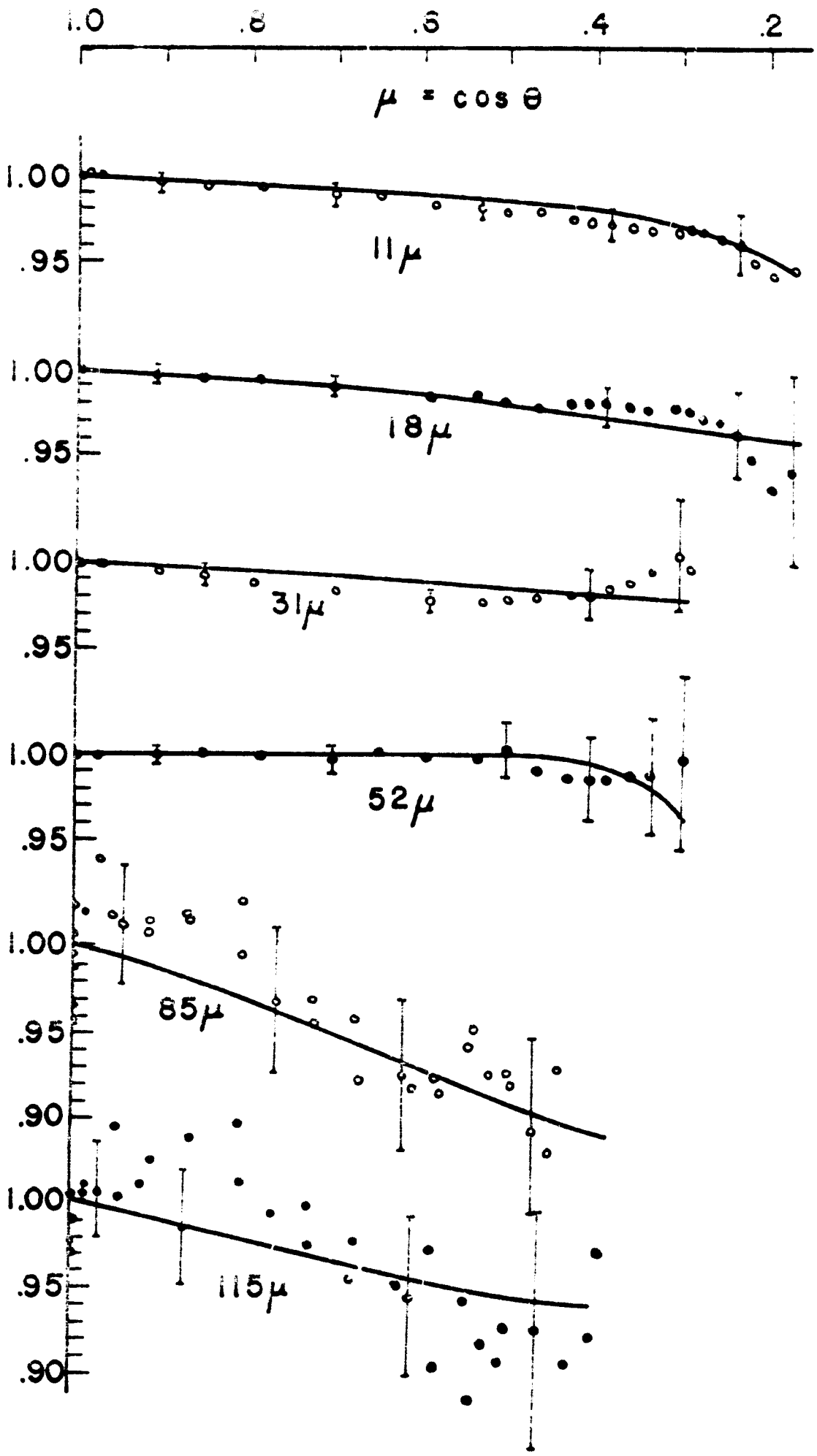
1.0
.8
.6
.4
.2
μ = cos θ
1.00
.95
11μ
1.00
.95
18μ
1.00
.95
31μ°
1.00
.95
52μ
1.00
.95
.90
85μ
1.00
.95
.90
115μ

FIGURE 14

The far infrared spectrum of the center of the solar disk deduced from the limb darkening measurements (solid curve) compared with the results of other investigators and the predictions of the Bilderberg model.

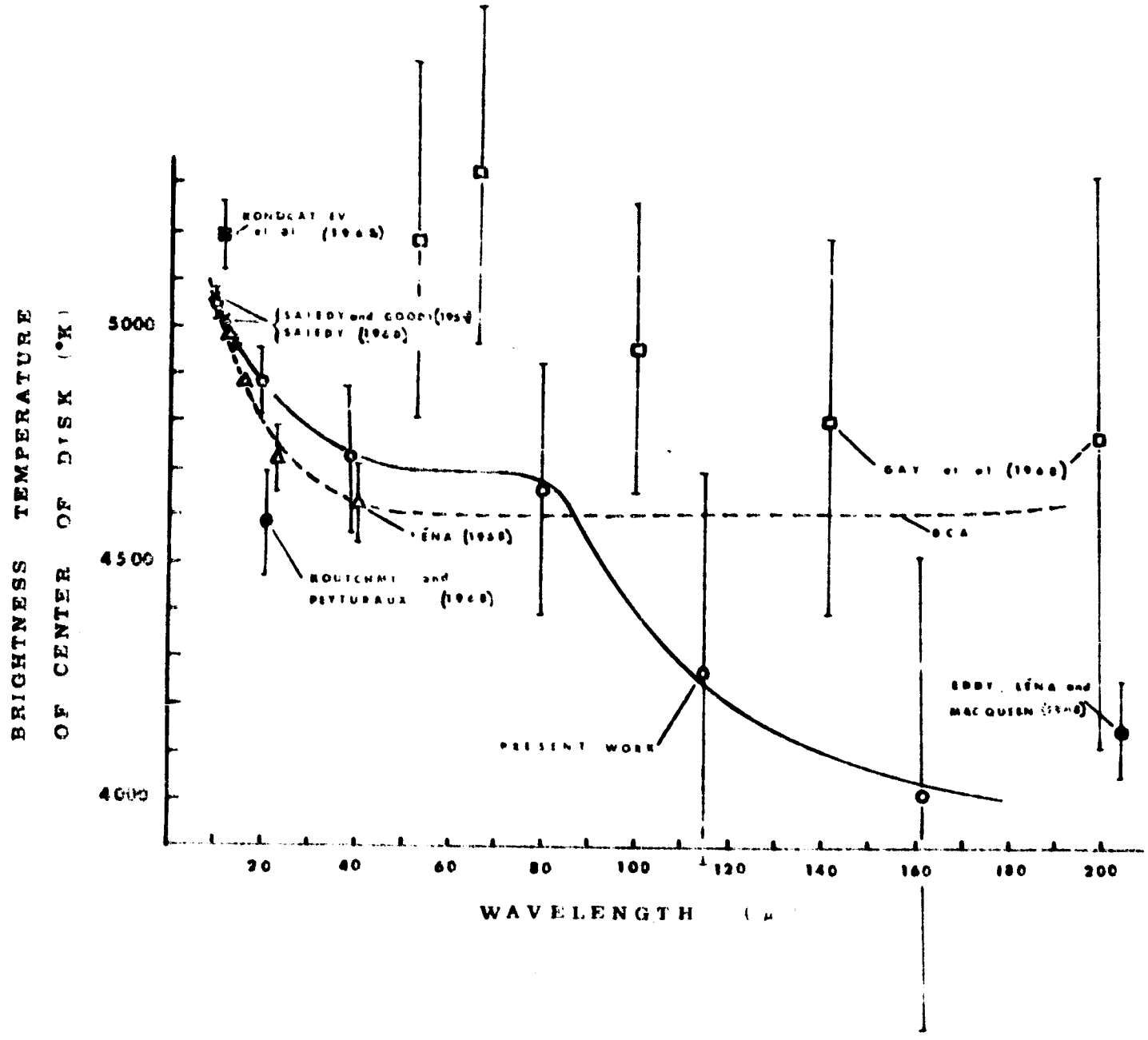
BRIGHTNESS TEMPERATURE OF CENTER OF DISK (°K)
5000
4500
4000
20
40
60
80
100
120
140
160
180
200
WAVELENGTH (μ
ROUDCAT EV et al (1964)
SAIEDY and COOPER (1954)
SAIEDY (1960)
LÉNA (1966)
ROUTCHMI and PETTURAUX (1968)
PRESENT WORK
GAY et al (1968)
OCA
EDDY, LÉNA and MACQUEEN (1970)

FIGURE 15

The electron temperature of the lower chromosphere as a function of reference optical depth, deduced from the limb darkening measurements.

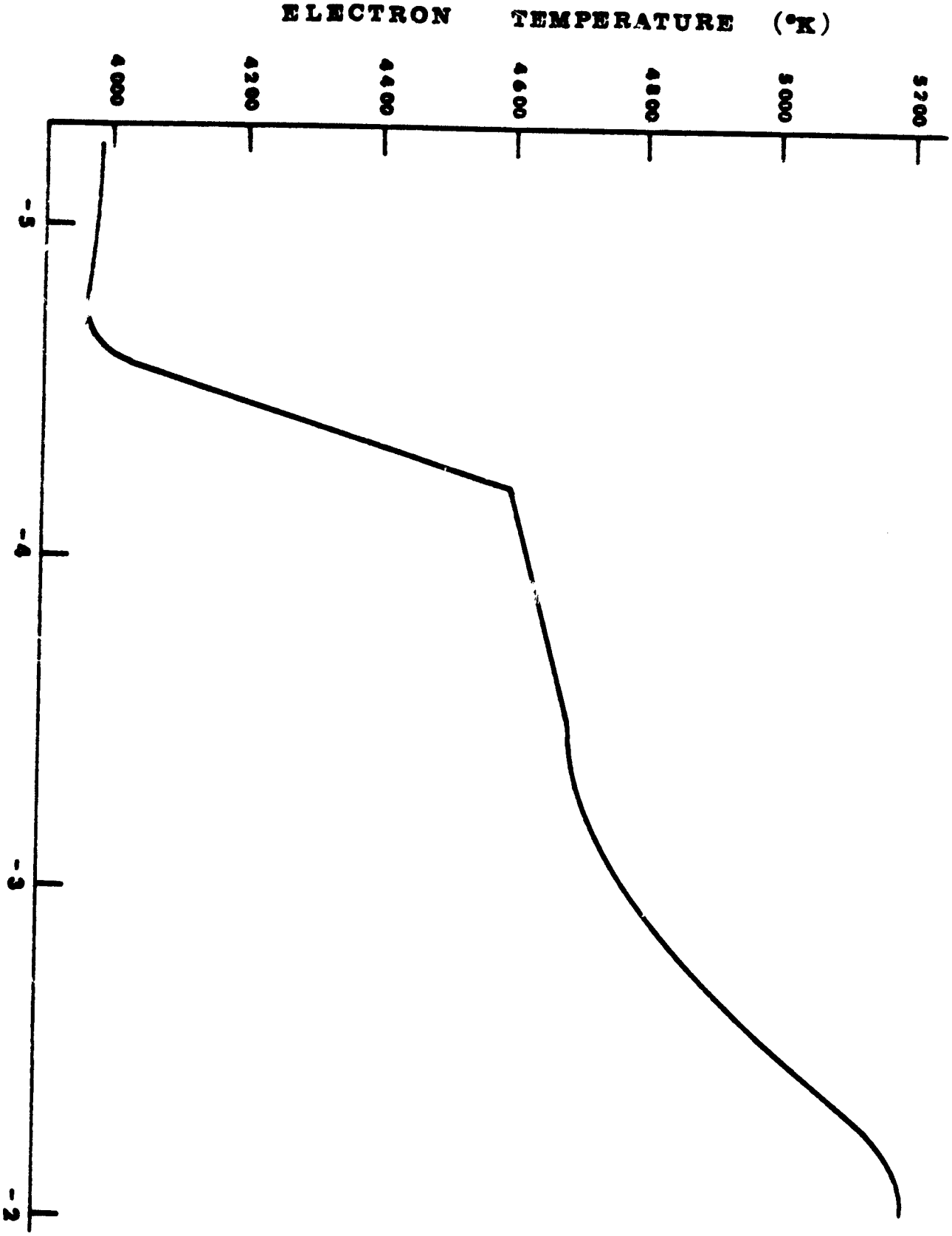
ELECTRON TEMPERATURE (°K)
4000
4200
4400
4600
4800
5000
5200
-1
-2
-3
-4
LOG T_e

FIGURE 16

The brightness temperature Θ_0 of the sun, corrected for departures from the Rayleigh-Jeans law, as a function of ξ.

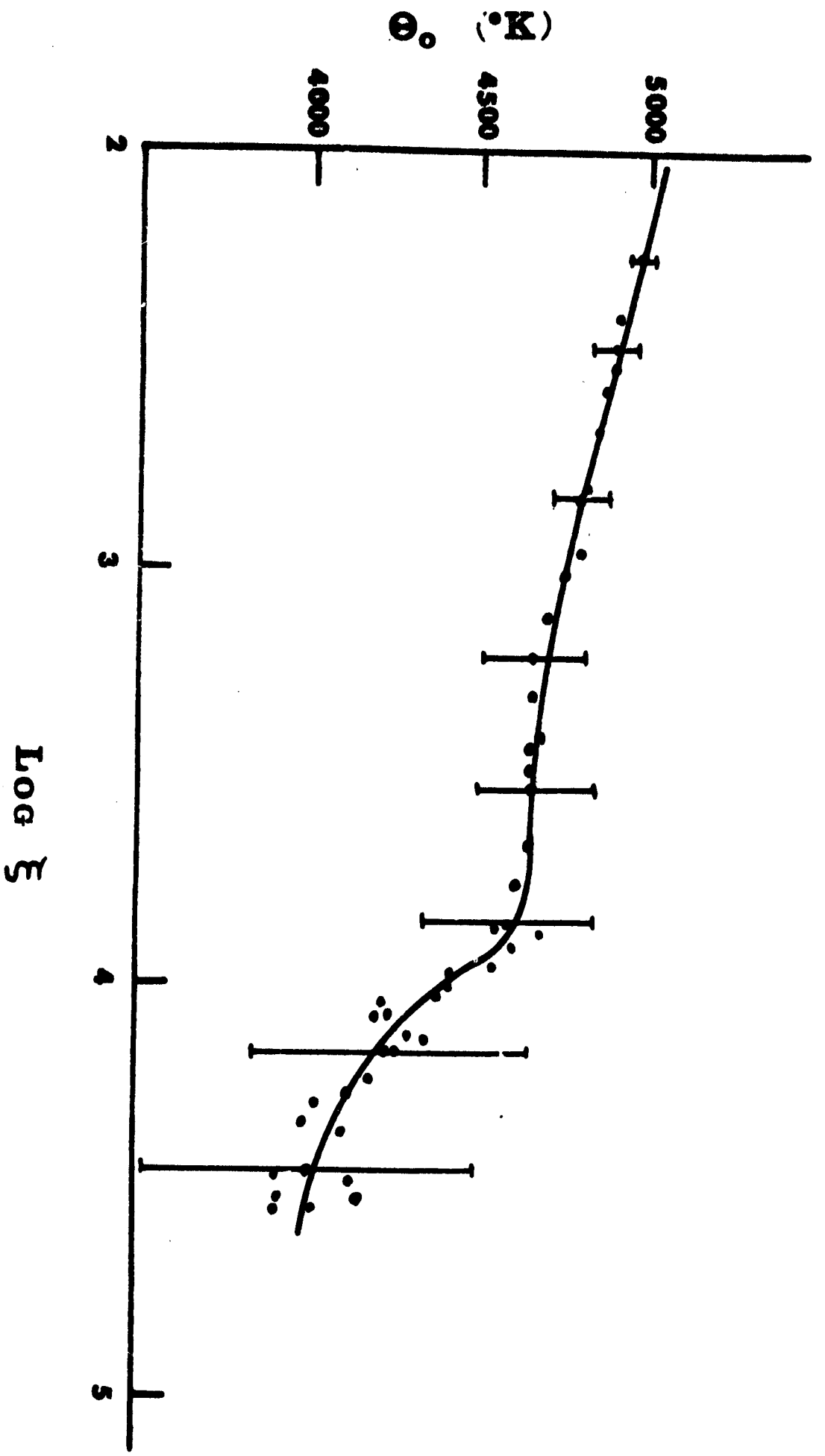
Θ_o (°K)
5000
4500
4000
2
3
4
5
Log Σ

BIBLIOGRAPHY

Allen, C.W. 1963, Astrophysical Quantities (London: Athlone Press).

Aller, L.H. 1963, Astrophysics: The Atmospheres of the Sun and Stars (New York: Ronald Press).

Athay, R.G., and Skumanich, A. 1968, Ap. J., 152, 141.

Bahng, J., and Schwarzschild, M. 1961a, Ap. J., 134, 312.

_____. 1961b, Ap. J., 134, 337.

Beckers, J.M. 1963, Ap. J., 138, 648.

Beer, R. 1966, Nature, 209, 1266.

Bottema, M. 1967, Appl. Optics, 6, 213.

Chalonge, D., and Kourganoff, V. 1946, Ann. d'ap., 9, 69.

Chandrasekhar, S. 1945, Ap. J., 101, 328.

_____. 1960, Radiative Transfer (New York: Dover Publications).

Chandrasekhar, S., and Breen, F. 1946, Ap. J., 104, 430.

Cillié, G.G., and Menzel, D.H. 1935, Harvard Observatory Circular, No. 410.

Czerny, M. 1923, Zeits. f. Physik, 16, 321.

de Jager, C. 1964, Mem. Soc. Roy. Sci. Liege, Ser. 5, 9, 151.

de Jager, C. and Neven, L. 1957, Mem. Soc. Roy. Sci. Liege, Ser. 4. 18, 3,7.

Eddy, J.A., Léna, P.J., and MacQueen, R.M. 1968, paper presented at 128th meeting of American Astronomical Society, Austin.

Gay, J., Lequeux, J., Verdet, J.P., Turon-Lacarrieu, P., Bardet, M., Roucher, J., Zeau, Y. 1968. Ap. Letters, 2, 169.

Geltman, S. 1956, Ap. J., 141, 376.

Gingerich, O. 1969, paper presented at Solar Physics meeting of American Astronomical Society, Pasadena.

_____. 1961, Ap. J., 134, 653.

Gingerich, O., and de Jager, C. 1968, Solar Phys., 3, 5.

Goldberg, L., and Muller, E.A. 1953, Ap. J., 118, 397.

Goody, R.M. 1964, Atmospheric Radiation (Oxford: Oxford University Press).

Heintze, J. 1965, Rech. Obs. Astron. Utrecht, 17, 2.

John, T.L. 1964, M.N.R.A.S., 128, 93.

_____. 1966, ibid., 131, 315.

King, J.I.F. 1964, J. Atm. Sci., 21, 324.

Kondrat'ev, K., Badinov, I., Ascheleulov, S.V., and Andreev, S.D. 1965, Bull. USSR Acad. Sci., Atmos. and Oceanic Phys. Series, 1, 363.

Koutchmy, S., and Peyturaux, R. 1968, C.R. Acad. Sci. Paris, Ser. B, 267, 905.

Leighton, R.B. 1959a, Ap. J., 130, 366.

_____. 1959b. Principles of Modern Physics (New York: McGraw-Hill Co.).

Leighton, R.B., Noyes, R.W., and Simon, G.W. 1962, Ap. J., 135, 474.

Léna, P.J. 1968, Solar Phys., 3, 28.

_____. 1969 (private communication).

Linsky, J. 1968, Smithsonian Astrophysical Observatory Special Report, No. 274.

MacQueen, R.M. 1968, Ap. J., 154, 1059.

Madden, R.P. 1956, Dissertation, Johns Hopkins University, Baltimore.

Mehltretter, J. P. 1967, Bundesministerium für wissenshaftliche Forschung Forschungsbericht W67-38.

Menzel, D. H. and Pekeris, C. L. 1935, M.N.R.A.S., 96, 77.

Minnaert, M. 1953, in The Sun, ed. G. P. Kuiper (Chicago: University of Chicago Press).

Mitsuishi, A., Yamada, Y., and Yoshinaga, H. 1962, J. Op. Soc. Am., 52, 14.

Mott, N. F., and Massey, H. S. W. 1950, The Theory of Atomic Collisions (Oxford: Oxford University Press).

Newkirk, G. A. 1957, Ap. J., 125, 571.

Nidey, R. A. 1968, Kitt Peak National Observatory Contribution No. 144.

Noyes, R. W. 1966, Ap. J., 145, 344.

Noyes, R. W., Beckers, J. M., and Low, F. J. 1968, Solar Phys., 3, 36.

Ohmura, T., and Ohmura, H. 1960, Ap. J., 131, 8.

Pagel, B. E. J. 1957, Ap. J., 125, 298.

Pannekoek, A. 1931, M.N.R.A.S., 91, 162.

Rathmann, C. L., Mann, G. H., and Nordberg, M. E. 1968, Appl. Optics, 7, 819.

Rayleigh, Third Baron (J. W. Strutt). 1885, Phil. Mag., 20, 354.

Rich, J. 1966, Dissertation, Harvard University, Cambridge, Mass.

Rubens, H., and Wood, R. W. 1911, Phil. Mag., 21, 249.

Saiedy, F. 1960, M.N.R.A.S., 121, 483.

Schwarzschild, M. 1959, Ap. J., 130, 345.

Strong, J. 1967a, Appl. Optics, 6, 179.

Strong, J. 1967b (private communication).

Thomas, R.N., and Athay, R.G. 1961. Physics of the Solar Chromosphere (New York: Interscience Publishers).

Tousey, R. 1963, Space Sci. Rev., 2, 3.

Twomey, S. 1965, J. Atm. Sci., 22, 95.

Ulrich, B.T. 1968, paper presented at 128th meeting of American Astronomical Society, Austin.

Wheeler, J.A., and Wildt, R. 1942, Ap. J., 95, 281.

White, O.R. 1968, Ap. J., 152, 217.

Wildt, R. 1939, Ap. J., 89, 295.

Wooley, R.v.d.R., and Stibbs, D.W.N. 1953, The Outer Layers of a Star (Oxford: Oxford University Press).

Young, C.A. 1897, The Sun (New York: Appleton).

Zander, R. 1966, J. Geophys. Res., 71, 3775.